

The *Spitzer* Local Volume Legacy: Survey Description and Infrared Photometry

D.A. Dale¹, S.A. Cohen¹, L.C. Johnson^{1,7}, M.D. Schuster¹, D. Calzetti², C.W. Engelbracht³,
A. Gil de Paz⁴, R.C. Kennicutt^{5,3}, J.C. Lee⁶, A. Begum⁵, M. Block³, J.J. Dalcanton⁷,
J.G. Funes⁸, K.D. Gordon⁹, B.D. Johnson¹⁰, A.R. Marble³, S. Sakai¹¹, E.D. Skillman¹²,
L. van Zee¹³, F. Walter¹⁴, D.R. Weisz¹², B. Williams⁷, S.-Y. Wu², Y. Wu¹⁵

ABSTRACT

The survey description and the near-, mid-, and far-infrared flux properties are presented for the 258 galaxies in the Local Volume Legacy (LVL). LVL is a *Spitzer Space Telescope* legacy program that surveys the local universe out to 11 Mpc, built upon a foundation of ultraviolet, H α , and HST imaging from 11HUGS (11 Mpc H α and Ultraviolet Galaxy Survey) and ANGST (ACS Nearby Galaxy Survey Treasury). LVL covers an unbiased, representative, and statistically robust sample of nearby star-forming galaxies, exploiting the highest extragalactic spatial resolution achievable with *Spitzer*. As a result of its approximately volume-limited nature, LVL augments previous *Spitzer* observations of present-day galaxies with improved sampling of the low-luminosity galaxy population. The collection of LVL galaxies shows a large spread in mid-infrared colors, likely due to the conspicuous deficiency of 8 μ m PAH emission from low-metallicity, low-luminosity galaxies. Conversely, the far-infrared emission tightly tracks the total infrared emission, with a dispersion in their flux ratio of only 0.1 dex. In terms of

¹Department of Physics and Astronomy, University of Wyoming, Laramie, WY 82071; ddale@uwyo.edu

²Astronomy Department, University of Massachusetts, Amherst, MA 01003

³Steward Observatory, University of Arizona, Tucson, AZ 85721

⁴Departamento de Astrofísica, Universidad Complutense, Madrid, E-28040, Spain

⁵Institute of Astronomy, University of Cambridge, Cambridge CB3 0HA, United Kingdom

⁶Carnegie Observatories, 813 Santa Barbara Street, Pasadena, CA 91101

⁷Department of Astronomy, University of Washington, Seattle, WA 98195

⁸Vatican Observatory Research Group, Steward Observatory, University of Arizona, Tucson, AZ 85721

⁹Space Telescope Science Institute, 3700 San Martin Drive, Baltimore, MD 21218

¹⁰Department of Astronomy, Columbia University, New York, NY 10027

¹¹Division of Astronomy and Astrophysics, University of California, Los Angeles, CA 90095

¹²Astronomy Department, University of Minnesota, Minneapolis, MN 55455

¹³Department of Astronomy, Indiana University, Bloomington, IN 47405

¹⁴Max Planck Institut für Astronomie, Königstuhl 17, 69117 Heidelberg, Germany

¹⁵Infrared Processing and Analysis Center, California Institute of Technology, MC 314-6, Pasadena, CA, 91125

the relation between infrared-to-ultraviolet ratio and ultraviolet spectral slope, the LVL sample shows redder colors and/or lower infrared-to-ultraviolet ratios than starburst galaxies, suggesting that reprocessing by dust is less important in the lower mass systems that dominate the LVL sample. Comparisons with theoretical models suggest that the amplitude of deviations from the relation found for starburst galaxies correlates with the age of the stellar populations that dominate the ultraviolet/optical luminosities.

Subject headings: surveys — galaxies: photometry — infrared: galaxies

1. Introduction

Although star formation rates based on optical spectroscopy and *GALEX* ultraviolet and *Spitzer* infrared imaging have been measured for thousands of galaxies (and hundreds of thousands via the Sloan Digital Sky Survey), most currently available datasets are derived from flux-limited samples, and thus suffer from well-known biases against low-mass, low surface brightness systems. Multi-wavelength datasets that do include such systems generally only provide representative samples of this low-mass galaxy population (e.g., SINGS; Kennicutt et al. 2003), and are thus not suitable for studies that seek to probe the low metallicity dwarf galaxy regime and that require datasets which are true to the statistics rendered by volume-limited sampling. The goal of the *Spitzer* Local Volume Legacy (LVL) survey¹ is to fill a vital niche in existing multi-wavelength surveys of present-day galaxies with a statistically robust, approximately volume-complete study of our nearest neighbors.

With LVL, we have directly addressed this issue by performing the most complete census to date of dust and star formation within the Local Volume. LVL consolidates and builds upon recent Local Volume galaxy surveys that have acquired ground-based narrowband H α (Kennicutt et al. 2008), *GALEX* ultraviolet (Lee et al. 2009a) and *HST* resolved stellar population imaging (Dalcanton et al. 2009), by collecting *Spitzer* IRAC and MIPS infrared imaging for a complete sample of 258 galaxies derived from these programs. The resultant LVL multi-wavelength dataset provides information on each galaxy’s (*i*) current star formation rate, as traced by H α emission, which is produced by the recombination of gas ionized by massive, short-lived OB stars (<20 Myr; Meynet & Maeder 2000), (*ii*) star formation rate averaged over a longer \sim 100 Myr timescale, as traced by the non-ionizing ultraviolet continuum which originates in the photospheres of OB stars, (*iii*) overall stellar mass, from 3.6 and 4.5 μ m luminosities which are generally dominated by the light from old stellar populations, and (*iv*) dust content, from both the strength and the shape of the infrared emission, which represents the stellar light that has been absorbed and re-radiated by dust. Temporally resolved star formation histories derived from the modeling of stellar population color-magnitude diagrams from *HST* resolved stellar photometry are also available for 69 of the

¹<http://www.ast.cam.ac.uk/IoA/research/lvls>

closer galaxies in the sample (e.g., Williams et al. 2009). The collection of these observations enable a wealth of spatially-resolved and spatially-integrated studies probing present-day star formation, chemical abundance, stellar structure, and dust properties as well as galaxy evolution, particularly for metal-poor, low-mass galaxies which dominate the LVL sample by number. As part of the LVL program, we are providing homogeneously processed $H\alpha$, *GALEX* ultraviolet and *Spitzer* IRAC and MIPS infrared images to the community. Public data releases have begun through the NASA/IPAC Infrared Science Archive² (IRSA).

Principal science issues to be addressed by LVL include: constraining the physical mechanisms underlying dust heating and understanding correlations between infrared emission, dust content, and global galaxy properties; establishing the primary factors which influence polycyclic aromatic hydrocarbon (PAH) emission and evaluating the robustness of PAH emission as a star formation rate indicator, particularly at low metallicities and high specific star formation rates; and probing the temporal variation of star formation as a function of global properties, with special focus on the dwarf galaxy population (e.g., Lee et al. 2009b). Specific forthcoming papers concentrate on the development of an accurate photometric technique for gauging PAH emission (Marble et al. 2009), the impact of relatively young, luminous AGB stars on stellar masses derived from the near-infrared (Johnson et al. 2009), utilizing ultraviolet-infrared colors to investigate the “inside-out” growth of galaxies (Gil de Paz et al. 2009), a characterization of the population of heavily-obscured star-forming regions (Staudaher et al. 2009), using integrated fluxes to model the spectral energy distributions with the aim of quantifying parameters such as dust mass and temperature, radiation field strength, dust-to-gas ratio, and PAH mass fraction (Gordon et al. 2009; Draine et al. 2009), and combining $H\alpha$ and infrared data to formulate optimal star formation rate indicators. Efforts are also being made to collect new and existing optical *UBVRI* imaging and spectroscopy for the sample, which enable, for example, work updating the local mass/luminosity-metallicity relationship from the *B* to 4.5 μm bands (Lee et al. 2009c), and stellar energy distribution fitting using stellar population synthesis model grids to provide constraints on star formation histories and present-day stellar masses.

In this paper, we provide a requisite component for much of this work by presenting the *Spitzer* observations, data reduction and IRAC and MIPS infrared flux densities for the LVL sample. Near-infrared photometry measured from 2MASS data within the same apertures that are used on the *Spitzer* imaging are also provided. Section 2 describes the sample, § 3 reviews the observational and data processing programs, § 4 covers details of the integrated aperture photometry, § 5 presents initial results based on the photometry, and § 6 summarizes our work.

²<http://ssc.spitzer.caltech.edu/legacy/lvlhistory.html>

2. The Sample

The Local Volume Legacy public dataset consists of *GALEX* ultraviolet, $H\alpha$ and *Spitzer* IRAC and MIPS imaging for a tiered sample of 258 galaxies that have been drawn from two existing volume-limited surveys. The inner tier of LVL mainly consists of galaxies targeted by ANGST, the ACS Nearby Galaxy Survey Treasury (Dalcanton et al. 2009). This includes all known galaxies within 3.5 Mpc which lie outside the Local Group and the Galactic plane ($|b| > 20^\circ$), as well as galaxies in the M81 group and Sculptor filament. ANGST provides *GALEX* ultraviolet imaging and has augmented existing deep *HST* imaging with new observations to provide uniform stellar photometry with homogeneous depth for these galaxies. The outer tier of LVL is derived from the larger 11 Mpc narrowband $H\alpha$ imaging survey of Kennicutt et al. (2008), and *GALEX* ultraviolet follow-up observations of a sub-sample which avoids the Galactic plane ($|b| > 30^\circ$) (Lee et al. 2009a). The $H\alpha$ survey and the *GALEX* ultraviolet component taken together has been referred to as 11HUGS, the 11 Mpc $H\alpha$ and Ultraviolet Galaxy Survey. The sample used by 11HUGS is given in Kennicutt et al. (2008) and was compiled as follows. A primary subset of the sample aims to be as complete as possible in its inclusion of galaxies that meet a combined criteria of $D \leq 11$ Mpc, $|b| > 20^\circ$, $m_B < 15$ mag and RC3 type $T \geq 0$ (i.e., galaxies with spiral and irregular morphologies later than S0a). A secondary subset is comprised of galaxies within 11 Mpc for which $H\alpha$ data are available, but fall outside one of the limits in magnitude, Galactic latitude and morphological type, and have available $H\alpha$ data (i.e., galaxies that were either observed as available telescope time allowed, or had existing $H\alpha$ measurements in the literature).

The sum of the primary and secondary subsets compiled in Kennicutt et al. (2008) encompasses the majority of the ANGST galaxies, as well as Local Group galaxies not targeted by ANGST. To build the outer tier of LVL, we have targeted those galaxies in the primary subset, but with more stringent limits on Galactic latitude ($|b| > 30^\circ$, consistent with that applied for *GALEX* follow-up³) and a slightly relaxed brightness limit ($m_B < 15.5$ mag). Beyond these bounds the original surveys that have provided the bulk of our knowledge about the Local Volume galaxy population are known to become severely incomplete (e.g., Tully 1988). Within the bounds, statistical tests and comparison with blind all-sky H I surveys confirm that the sample completeness is excellent ($>95\%$; Lee et al. 2009b). More details on the sample selection and properties of the precursor surveys are given in Dalcanton et al. (2009; ANGST sample definition, *HST* observations and reduction), Kennicutt et al. (2008; 11 Mpc sample compilation, $H\alpha$ observations, and integrated flux and equivalent width catalog), Lee et al. (2007; Local Volume star formation demographics as traced by the $H\alpha$ equivalent width), Lee et al. (2009b; 11 Mpc sample completeness properties) and Lee et al. (2009a; *GALEX* observations and integrated ultraviolet photometry catalog). A schematic illustration of LVL’s tiered volume coverage is shown in Figure 1, and the final LVL sample of 258 galaxies is given in Table 1.

³A Galactic latitude limit of $|b| > 30^\circ$ for the ultraviolet observations avoids objects with excess Galactic extinction and high foreground star density which would violate *GALEX*’s bright object safety limits.

The two tiers of LVL are highly complementary. Figure 2 presents distributions in the primary selection criteria (morphology, apparent B magnitude, Galactic latitude, and distance) for LVL, where the ANGST sub-sample has been marked separately. Data on these basic properties are taken from the compilations given in Kennicutt et al. (2008) and Dalcanton et al. (2009). ANGST provides complete coverage within an inner volume, and includes both early (dwarf spheroidals, ellipticals, lenticulars) and late (spiral and irregular) morphological types, and many of the lowest mass galaxies. 11HUGS covers a 30 times larger volume, and therefore offers better statistical sampling of the star-forming galaxy population as a whole. As would be expected for an approximately volume-limited sample, the sample population is dominated by low-luminosity, dwarf galaxies. Approximately 61% are irregulars, 31% have spiral morphology, 5% are dwarf spheroidals, and 2% are early-type galaxies. For comparison, the SINGS sample is dominated more by luminous spiral galaxies (63%), with 17% irregular, 12% S0, and 8% elliptical morphologies. While the 11HUGS-based portion of the sample goes as faint as $m_B = 15.5$ mag, as explained above, Figure 2 shows that the faintest systems in the ANGST inner-tier approach $m_B = 19$ mag (e.g., M81 Dwarf A and BK3N). In terms of their absolute B magnitudes, 81% of the galaxies in LVL are intrinsically fainter than the LMC ($M_B = -17.9$ mag).

The distances in the LVL sample range from 50-60 kpc for the Magellanic Clouds out to 11 Mpc at the outer edge of the survey. Kennicutt et al. (2008) describe in detail the origins of the adopted distances displayed in Figure 2. Many of the galaxies within ~ 5 Mpc have distance determinations based on standard candles, whereas estimates based on secondary indicators or flow-corrected velocities (assuming $H_0 = 75$ km s $^{-1}$ Mpc $^{-1}$) are adopted for the more distant systems. About half of the sample galaxies have reliable distances from measurements of the tip of the red giant branch ($\sim 40\%$ of the sample) and Cepheid variables (6% of the sample). It is important to note that an inherent difficulty with efforts to construct a volume-limited sample is that its membership will necessarily be fluid until accurate distance and photometric measurements are available for all of the galaxies that are within the volume and around its periphery. Since the inception of the LVL *Spitzer* program, four galaxies included in the sample (and in Table 1) have updated distances which place them outside of 11 Mpc. In addition, the flow model initially applied was updated in Kennicutt et al. (2008) to provide consistency with one used by NED.⁴ As a result 30 galaxies with $|b| > 30^\circ$ and $m_B < 15.5$ mag in the parent sample (Kennicutt et al. 2008) are not included in LVL. The galaxies are generally between 10 and 11 Mpc, where flow distance uncertainties ($\pm 15\%$) would most likely scatter objects in and out of the volume. Such uncertainties however, should not have a significant impact on studies which use the sample to statistically characterize the physical properties of local galaxies. Further discussion of such issues is provided in § 2 of Kennicutt et al. (2008).

Overall, the LVL sample covers a diverse cross-section of morphologies and star formation

⁴The NASA/IPAC Extragalactic Database (NED) is operated by the Jet Propulsion Laboratory, California Institution of Technology, under contract with NASA.

properties, and spans a factor of 10^4 in optical luminosity, a factor of 10^5 in star formation rate, and the full range of metallicities found locally (~ 1.5 dex). The nature of the sample allows LVL to more robustly sample infrared properties associated with metal-poor, dwarf galaxies than previous surveys. For example, the plots in Figure 3 show LVL’s coverage of parameter spaces defined by integrated infrared and infrared-to-optical galaxy properties. Also shown are the distributions for SINGS, which was designed to broadly, but not statistically, sample the range of properties in nearby galaxies. While the SINGS and LVL surveys are fairly similar in their distributions of far-infrared colors and infrared-to-optical ratios, the two surveys differ dramatically in their distributions of total infrared luminosity. As would be expected, LVL is far more effective at filling in the distribution at faint infrared luminosities, whereas SINGS includes more infrared-bright and dusty systems. Preliminary comparisons with the *IRAS* 1.2 Jy survey (Fisher et al. 1995) suggest that LVL and SINGS respectively sample preferentially the faint and bright envelopes of a broader distribution at lower infrared-to-optical ratios.

3. Observational Strategy and Data Processing

LVL *Spitzer* observations build upon IRAC and MIPS archival data which were already available for about a quarter of the sample when the program began. In this section we describe the observational strategy employed for the new IRAC and MIPS infrared data obtained to complete *Spitzer* coverage of the LVL sample, and the archival data that have been reprocessed for inclusion in our dataset.

3.1. New *Spitzer* IRAC 3.6, 4.5, 5.8, and 8.0 μm Data

New *Spitzer* IRAC (Fazio et al. 2004) observations were obtained for 180 LVL galaxies. The IRAC observing strategy follows that of SINGS, which shows that stellar and small grain dust emission is typically detected out to the optical radius at a surface brightness level of ~ 0.01 – 0.1 MJy sr $^{-1}$ (Regan et al. 2006; Dale et al. 2000). For galaxies smaller than the IRAC field of view ($D_{25} \leq 300''$) the Astronomical Observing Requests (AORs) were constructed using four dithered 30 s integrations. For larger galaxies a mosaicking strategy with \sim half-array spatial offsets was used, with the sizes of the mosaic ‘cores’ tailored to the optical size of each galaxy. Two sets of IRAC maps were obtained for each source to enable asteroid removal and to enhance map sensitivity and redundancy. Combining all eight 30 s frames thus results in a net integration per pixel of 240 s (and 120 s around the $\sim 2'.5$ -wide mosaic peripheries). Since each source was observed in all IRAC channels, ample sky coverage is automatically provided by the non-overlapping nature of the two IRAC fields-of-view.

The basic calibrated data (BCD) used for post-pipeline processing are from the S18.0 and S18.5 versions of the IRAC pipeline. These versions differ from their predecessors by including improved

corrections for muxbleed and the first-frame effect, among other corrections. The multi-epoch, multiple-pointing IRAC observations for each galaxy are combined into one single mosaic for each band using the MOPEX mosaicking software. Additional post-BCD processing includes: distortion corrections, rotation of the individual frames (for multi-epoch observations), bias structure and bias drift corrections, image offset determinations via pointing refinements from the SSC pipeline (MOPEX’s default), detector artifact removal, constant-level background subtraction, and image resampling to $0''.75$ pixels using drizzling techniques. The drizzling slightly improves the final PSF over the native one; the full-width half maxima are $\sim 1''.6$ in the shorter wavelength channels and $\sim 1''.9$ at $8\ \mu\text{m}$. The final images are in units of MJy sr^{-1} and have the average sky level removed; sky values are estimated via several “blank” regions located near but beyond the target galaxy emission. Though the LVL IRAC data processing is built upon MOPEX while the SINGS project developed its own IRAC data processing package, the nature of the final data products in the two surveys is essentially the same.

In cases where exceptionally bright target sources saturated or entered the non-linear regime of the detector during the 30 s exposure, additional 1.2 s images are used to allow for recovery of this information. Pixels affected by these issues, typically in the 5.8 and $8.0\ \mu\text{m}$ frames, are flagged during processing. The correction begins by creating a mosaic of the 1.2 s exposures interpolated onto the same pixel grid as the original mosaic. A difference image is then created from the two mosaics and any residual, systematic difference in the background sky levels is removed. Pixels in the difference image valued at $1\ \text{MJy sr}^{-1}$ or higher are flagged (routinely regions of ~ 400 contiguous pixels) and these pixels in the long integration mosaic are replaced by their short integration counterparts. Immediately outside of these saturated areas, the photometry of the 1.2 s-based mosaics is consistent with that from the far-deeper mosaics described above, and further away in the fainter surface brightness regions the deeper mosaics obviously more effectively detect emission. The nuclear regions for the following galaxies were corrected for saturation: NGC 0253, NGC 2903, NGC 3031, NGC 3034 (at all IRAC wavelengths), NGC 3351, NGC 3593, NGC 3627, NGC 4258, NGC 5195, and NGC 5253.

3.2. New *Spitzer* MIPS 24, 70, and $160\ \mu\text{m}$ Data

New *Spitzer* MIPS (Rieke et al. 2004) observations were obtained for 201 LVL galaxies. Galaxies were imaged in all three MIPS bands centered at 24, 70, and $160\ \mu\text{m}$, using the highly successful scan mapping strategy employed in the SINGS project. The scan mode was used even on galaxies small enough to fit within the array field of view, because achieving adequate background measurements for extended targets in the photometry mode is less efficient than in the scan mode. Each map was executed at the medium scan rate, and includes multiple scan legs tailored to the size of the galaxy and half-array offsets between scan legs. Each galaxy was mapped twice, with the maps separated by 10-40 days to allow time for the field-of-view to rotate and for asteroids to move out of the field. This second map was performed in the reverse direction (the “backward mapping”

mode), with offsets in the cross-scan and in-scan directions. Taken together, these mapping strategies ensure that each point on the galaxy is scanned over in two different directions, which aids reduction of array artifacts on both Si:As and Ge:Ga arrays. The in-scan offset ensures that Ge:Ga stimflashes do not occur at the same point in both maps and thereby improves the calibration. The integration time per point is 160, 80, and 16 s at 24, 70, and 160 μm , respectively.

The MIPS images are processed with the MIPS Data Analysis Tool (DAT; Gordon et al. 2005), supplemented by custom scripts for the specific data reduction and mosaicking of extended sources. The latter include at 24 μm : readout offset correction, array-averaged background subtraction, and exclusion of the first five images in each scan leg due to boost frame transients. At 70 and 160 μm , the custom scripts include a pixel-dependent background subtraction for each map to remove residual detector drifts and background cirrus and zodiacal emission. This method of reduction was used for all the SINGS galaxies as well as very large galaxies (M31, M33, M101, SMC, LMC, etc.). The resulting PSFs have full-width half maxima of ~ 6 , 18, and $40''$ at 24, 70, 160 μm , respectively. The pixel scales of the MIPS mosaics are $1''.5$, $4''.5$, and $9''.0$ at 24, 70, and 160 μm , respectively.

Finally, a correction for 70 μm non-linearity effects is included in the data processing. A correction of the form

$$f_{\text{true}}^{70\mu\text{m}} = 0.502(f_{\text{measured}}^{70\mu\text{m}})^{1.182}, \quad (1)$$

derived from data presented by Gordon et al. (2009) and slightly different than the form first presented in Dale et al. (2007) for SINGS galaxies, is applied to pixel values above a threshold of $\sim 44 \text{ MJy sr}^{-1}$. The uncertainties on the parameters in Equation 1 are $\sim 10\%$. The correction to the global 70 μm flux density is ≤ 1.01 for 83% of the sample, ≤ 1.05 for 90% of the sample, and ≤ 1.29 for all but two sources. The correction for NGC 0253, a galaxy with a well-known super star cluster, is 1.59. The correction for the starburst galaxy NGC 3034 (M82) is 1.83.

3.3. Archival *Spitzer* Data

Archival IRAC and MIPS data, with spatial coverage and sensitivity similar to or greater than that described in § 3.1 and § 3.2, are utilized for 78 (IRAC) and 57 (MIPS) galaxies. No new IRAC or MIPS observations were obtained for these subsets of the LVL sample. The data processing procedures for the archival data are the same as those followed for the new observations described above (including the use of the S18 IRAC data processing pipeline), except for the asteroid rejection in the few cases where only one epoch was measured. Table 2 indicates for which galaxies we use archival *Spitzer* data.

4. Aperture Photometry

This section describes the infrared flux densities measured for the LVL program. For a given galaxy, in most cases the same aperture was used for extracting all infrared flux densities. Elliptical apertures were based on capturing all the galaxy emission visible for all infrared images. Typically this means that the $3.6\ \mu\text{m}$ image was used to create the aperture, since $3.6\ \mu\text{m}$ is the bandpass within which *Spitzer* is most sensitive and stars are brightest. Occasionally the emission at $160\ \mu\text{m}$ shows the greatest spatial extent, resulting in part from the smearing involved with the $\sim 40''$ of the PSF at this wavelength. In addition, for a subset of ~ 40 LVL galaxies, the infrared-based apertures were slightly enlarged to capture extended ultraviolet emission. The aperture centers, semi-major and semi-minor axes a and b , and the position angles are provided in Table 1. The median semi-major axis is 1.13 times R_{25} , and 7% of the semi-major axes are smaller than R_{25} .

Table 2 presents the global flux densities for the entire LVL sample, for wavelengths spanning the near- to far-infrared. The compact table entry format T.UV \pm W.XYZ implies (T.UV \pm W.XY) $\times 10^Z$. The data are corrected for Galactic extinction (Schlegel, Finkbeiner, & Davis 1998) assuming $A_V/E(B - V) \approx 3.1$ and the reddening curve of Li & Draine (2001). The effect of airmass has been removed from the ground-based near-infrared fluxes. No color corrections have been applied to the flux densities. Additional issues such as sky removal, aperture corrections, and upper limits are covered in detail below.

The uncertainties provided in Table 2 include both calibration and statistical uncertainties. Including the uncertainties in aperture corrections described below, the IRAC calibration uncertainties are, conservatively, 5-10% for 3.6 and $4.5\ \mu\text{m}$ data, and 10-15% for 5.8 and $8.0\ \mu\text{m}$ data (Reach et al. 2005; Farihi et al. 2008; T. Jarrett, private communication); 10% IRAC calibration uncertainties are used in Table 2. MIPS calibration uncertainties are 4%, 5%, and 12% respectively at 24 , 70 , and $160\ \mu\text{m}$ (Engelbracht et al. 2007, Gordon et al. 2007, and Stansberry et al. 2007). A floor to the 2MASS uncertainties is fixed by setting the calibration errors to 5%.

4.1. 2MASS Near-Infrared JHK_s Photometry

The Two Micron All Sky Survey (2MASS) obtained data for the entire sky at 1.25 , 1.65 , and $2.17\ \mu\text{m}$ using two automated, ground-based 1.3 m telescopes (Skrutskie et al. 2006). Galaxy photometry is available from the 2MASS Extended Source Catalog for over a million galaxies and from the 2MASS Large Galaxy Atlas for several hundred galaxies larger than $1'$ (Jarrett et al. 2003). Integrated fluxes for several LVL galaxies were adopted from the Large Galaxy Atlas, and these are generally consistent with expectations based on IRAC 3.6 and $4.5\ \mu\text{m}$ fluxes and simple stellar model extrapolations to 2MASS wavelengths. However, most LVL galaxies do not appear in the Large Galaxy Atlas, and for these relatively faint systems many of the fluxes from the Extended Source Catalog are 0.5–2 mag low based on similar extrapolations from IRAC 3.6 and $4.5\ \mu\text{m}$ data. We find that when Extended Source Catalog fluxes appear unexpectedly faint, it is

typically due to the comparatively small apertures used in the automated 2MASS extraction (see, for example, the fairly extreme case of UGC 08245 in Figure 4). Hence we have independently extracted 2MASS fluxes for the vast majority of the LVL sample using the same apertures and foreground star removals used to determine IRAC and MIPS fluxes, as discussed in the following section. Figure 5 displays the ratios of our near-infrared extractions with those provided in the 2MASS Extended Source Catalog. Included in the figure are results from Kirby et al. (2008) based on deep H band imaging of nearby galaxies with the 3.9 m Anglo-Australian Telescope; Kirby et al. (2008) likewise find that the fainter sources in the Extended Source Catalog have their global fluxes underestimated. The correction factors in Figure 5 rise steeply with decreasing flux densities below 0.1 Jy (~ 10 mag). The secureness of the detections below this level also drops quickly, down to the $2\text{--}3\sigma$ level for $f_\nu \lesssim 0.01$ Jy.

4.2. *Spitzer* 3.6, 4.5, 5.8, 8.0, 24, 70, and 160 μm Photometry

4.2.1. *Foreground Star and Background Galaxy Removal*

The presence of foreground stars and background galaxies can significantly affect the global infrared fluxes for some galaxies, particularly the fainter dwarfs and galaxies at low Galactic latitudes. Once identified, the foreground stars and background galaxies are removed through a simple interpolation of the local sky from the images using the IRAF task `IMEDIT`. Our procedure for distinguishing between target galaxy and foreground/background sources relies on a multi-wavelength analysis (3.6, 8.0, 24 μm , and $H\alpha$), looking for objects that are $H\alpha$ -rich (target galaxy) or especially blue (foreground stars; $f_\nu(3.6)/f_\nu(8.0) > 8$), or extended red systems with smooth morphologies (background galaxies). Archival *Hubble Space Telescope* imaging was also inspected for obvious background galaxy or foreground stellar identifications, when available. When uncertain about the identification of a particular source, we opted to err on the conservative side and allow such sources to remain in the global flux extraction. However, these sources of uncertain origin are typically very faint and have negligible impact on global flux extractions. The median ratios of corrected-to-stellar contaminated fluxes is [0.854, 0.846, 0.939, 0.971, 0.980, 1.00, 1.00] at [3.6, 4.5, 5.8, 8.0, 24, 70, 160] μm ; very few significant corrections are made at 24, 70, and 160 μm .

4.2.2. *Aperture Corrections*

Since the IRAC flux calibration is based on point source photometry for a $12''$ radius aperture, the fluxes for all extended sources and aperture radii $\neq 12''$ need to have an additional correction applied. These corrections account for the “extended” emission due to the wings of the PSF and also for the scattering of the diffuse emission across the IRAC focal plane. This photometric correction is different than merely subtracting off the sky value (§ 3.1). As described in Dale et al. (2007), the IRAC extended source correction has been derived for a variety of source morphologies and

extents. For an effective aperture radius $r = \sqrt{ab}$ in arcseconds derived from the semi-major a and semi-minor b ellipse axes provided in Table 1, the IRAC extended source aperture correction is

$$f_{\text{true}}^{\text{IRAC}} / f_{\text{measured}}^{\text{IRAC}} = Ae^{-r^B} + C, \quad (2)$$

where A , B , and C are listed in Table 3⁵. The median IRAC extended source aperture corrections are [0.914, 0.941, 0.826, 0.756] at [3.6, 4.5, 5.8, 8.0] μm .

In contrast to the IRAC aperture corrections, the main reason MIPS aperture corrections are needed is the smearing of light according to the PSF profile; the measured MIPS fluxes need to be slightly boosted to account for light diffracted beyond the extent of the chosen apertures. MIPS aperture corrections are empirically determined from a comparison of fluxes from smoothed and unsmoothed 3.6 μm imaging, an approximate proxy for tracing the MIPS galaxy morphologies. The aperture correction for a given MIPS flux is the ratio of the fluxes from the unsmoothed 3.6 μm image to the flux from the 3.6 μm image smoothed to the same PSF as the MIPS image in question. The median MIPS aperture corrections are [1.01, 1.01, 1.03] at [24, 70, 160] μm , and the most significant corrections are [1.07, 1.20, 1.68] for UGC 05923.

4.3. Upper Limits

Many of the optically-faint galaxies in the sample are frequently undetected in the infrared, particularly at wavelengths of 5.8 μm and longer. Upper limits are included in Table 2 for sources undetected by infrared imaging. In all cases “undetected” implies that the measured flux density is below the 5σ upper limit. The 5σ upper limits for *Spitzer* imaging are derived assuming a galaxy spans all N_{pix} pixels in the aperture,

$$f_{\nu}(5\sigma \text{ upper limit})_{\text{Spitzer}} = 5 \sigma_{\text{sky}} \Omega_{\text{pix}} \sqrt{N_{\text{pix}} + N_{\text{pix}}^2 / N_{\text{sky}}} \approx 5 \sigma_{\text{sky}} \Omega_{\text{pix}} \sqrt{2N_{\text{pix}}} \quad (3)$$

where σ_{sky} is the sky surface brightness fluctuation per pixel (MJy sr⁻¹), Ω_{pix} the solid angle subtended per pixel, and N_{sky} ($\approx N_{\text{pix}}$) the total number of pixels in the sky apertures. The parameter σ_{sky} is approximately 0.02, 0.03, 0.11, 0.12, 0.2, 0.9, and 1.7 MJy sr⁻¹ at 3.6, 4.5, 5.8, 8.0, 24, 70, and 160 μm , respectively, though somewhat larger values are employed for situations where the sky fluctuations are notably larger due to flatfielding errors, scattered light, cirrus, etc. A similar computation for 2MASS near-infrared upper limits is carried out after converting that survey’s mean 10σ point source sensitivities (~ 16.4 , 15.5 , and 14.8 mag for J , H , and K_s , respectively; Skrutskie et al. 2006) to 5σ values and accounting for the difference in the sizes of the 2MASS point source aperture ($\pi r_{2\text{MASS}}^2$; $r_{2\text{MASS}} = 4''$) and the LVL apertures (πab). In other words,

$$f_{\nu}(5\sigma \text{ upper limit})_{2\text{MASS}} = \frac{5}{10} f_{\nu}(2\text{MASS } 10\sigma \text{ point source limit}) \sqrt{\frac{\pi ab}{\pi r_{2\text{MASS}}^2}}. \quad (4)$$

⁵See <http://ssc.spitzer.caltech.edu/irac/calib/extcal/>

5. Results

5.1. Detection Rate

The lower panels of Figure 6 display the detection rates for the different *Spitzer* imaging channels as a function of *B* band apparent and absolute magnitudes. Nearly all galaxies are detected at all *Spitzer* wavelengths down to $m_B \approx 14$ mag and $M_B \approx -13$ mag. Consistent with our pre-survey expectations, the $m_B \sim 15.5$ mag cut-off for the outer tier of the sample that extends to 11 Mpc (see § 2) proved to be a useful sample selection criterion, because very few galaxies fainter than $m_B \sim 15.5$ mag were detected in MIPS. The inner tier/ANGST portion of the sample extends the sample to much fainter levels, as faint as $m_B \approx 19$ mag in the cases of BK03N and M81 Dwarf A. As expected for the optically-faint galaxies, the highest detection rates are found for the stellar-dominated 3.6 and 4.5 μm channels, while the 70 and 160 μm imaging proved to be far more challenging to convincingly detect cold dust emission. A stacking analysis (e.g., Dole et al. 2006) will be employed to obtain a better statistical understanding of the fainter galaxy population at long wavelengths, in particular with respect to the H I emission.

5.2. Comparison with Data from *IRAS*

Secure flux measurements are available at all *IRAS* and MIPS wavelengths for a subset of 70 LVL galaxies. The *IRAS* data are compiled from Rice et al. (1988), Moshir et al. (1990), Sanders et al. (2003), Lisenfeld et al. (2007), and our own archival extractions. Figure 7 provides a comparison of MIPS 24 μm and *IRAS* 25 μm data. The agreement between 24 and 25 μm fluxes is excellent: $\nu f_\nu(24\mu\text{m})/\nu f_\nu(25\mu\text{m}) = 1.02$ with a dispersion of 25%.

The aggregate emission from all dust grains is a fundamental metric of any galaxy. Figure 7 provides a comparison of the 3–1100 μm total infrared (*TIR*) for the LVL sample as measured by MIPS and *IRAS*. The MIPS-based total infrared is estimated from a linear combination of 24, 70, and 160 μm fluxes,

$$f(TIR)_{\text{MIPS}} = 1.559\nu f_\nu(24\mu\text{m}) + 0.7686\nu f_\nu(70\mu\text{m}) + 1.347\nu f_\nu(160\mu\text{m}), \quad (5)$$

and the *IRAS*-based total infrared is similarly computed from a linear combination of the 25, 60, and 100 μm fluxes,

$$f(TIR)_{\text{IRAS}} = 2.403\nu f_\nu(25\mu\text{m}) - 0.2454\nu f_\nu(60\mu\text{m}) + 1.6381\nu f_\nu(100\mu\text{m}), \quad (6)$$

which are Equations 4 and 5, respectively, in Dale & Helou (2002; see Equation 22 in Draine & Li 2007 for a variation of Equation 5 above that includes the IRAC 8.0 μm flux). The coefficients in the above two equations stem from fits to a suite of spectral templates applicable to a wide range of normal star-forming galaxies at redshift zero, where “normal” implies the exclusion of AGN and ultraluminous infrared galaxies (see § 5.3 and Figure 5 in Dale & Helou 2002 for a representative

sampling of the suite of templates). The uncertainty in using these prescriptions to compute the total infrared for normal star-forming galaxies is estimated to be of order 25% (Draine & Li 2007).

The MIPS-based version should be more accurate since the infrared wavelength baseline spanned by MIPS is longer than the baseline covered by *IRAS*, and more importantly, the *IRAS* detectors do not sample the bulk of the dust in the coldest, most quiescent galaxies. To determine if these differences in wavelength coverage between *IRAS* and MIPS result in different estimates of the total infrared, the two righthand panels in Figure 7 compare $f(TIR)_{\text{MIPS}}$ and $f(TIR)_{\text{IRAS}}$. The ratio of MIPS- and *IRAS*-based total infrared measures has a scatter (21%) similar to that in the 24-to-25 μm comparison, but the average ratio is 1.17. These findings are similar to those by Kennicutt et al. (2009) for a sample of 205 nearby galaxies with both *IRAS* and MIPS data. The righthand panel in Figure 7 includes semi-empirical predictions from models of infrared spectral energy distributions. As alluded to above, part of the systematic offset in $TIR_{\text{MIPS}}/TIR_{\text{IRAS}}$ can be attributed to the relative inability of *IRAS* to accurately measure the total infrared for cold galaxies. The infrared emission for the coldest galaxies, galaxies with the lowest $f_{\nu}(60\mu\text{m})/f_{\nu}(100\mu\text{m})$ ratios, peaks beyond *IRAS*’s 100 μm detector, and thus the total infrared as measured by *IRAS* is systematically low for the coldest galaxies.

5.3. Multi-Wavelength Spectral Energy Distributions

Figures 8 and 9 show ultraviolet- $\text{H}\alpha$ -infrared mosaics of NGC 5236 and UGC 05829, spanning wavelengths where the emission is dominated by young stars (0.15 μm), H II regions ($\text{H}\alpha$), old stars (3.6 μm), PAHs (8.0 μm), very small grains (24 μm) and large grains (70 μm). The galaxies and wavelengths displayed in these two figures highlight the broad range of environments and galaxies sampled by the LVL survey (see § 2). Figure 10 provides the panchromatic ultraviolet-infrared broadband spectral energy distributions for all 258 galaxies.⁶ The solid curve is the sum of a dust (dashed) and a stellar (dotted) model. The dust curve is a Dale & Helou (2002) model (least squares) fitted to ratios of the observed 24, 70, and 160 μm fluxes, and then scaled to match the overall infrared brightness. The α_{SED} listed within each panel parameterizes the distribution of dust mass as a function of heating intensity U in units of the local ultraviolet interstellar radiation field, as described in Dale & Helou (2002):

$$dM_{\text{dust}}(U) \propto U^{-\alpha_{\text{SED}}} dU, \quad 0.3 \leq U \leq 10^5. \quad (7)$$

To quantify the uncertainty on α_{SED} displayed within each panel of Figure 10, 1,000 Monte Carlo simulations of the fit to each galaxy’s far-infrared fluxes were performed, utilizing the tabulated flux uncertainties to add a random (Gaussian deviate) flux offset at each MIPS wavelength. The

⁶The far- and near-ultraviolet data are from images acquired as part of the *GALEX* Nearby Galaxy Survey, Medium Imaging Survey, and All-Sky Imaging Survey along with several Guest Investigator programs including the 11HUGS Cycle 1 and Cycle 4 and ANGST Cycle 3 proposals.

α_{SED} uncertainties reflect the standard deviations in the simulations. The stellar curve is a 1 Gyr continuous star formation, solar metallicity curve from Vazquez & Leitherer (2005) fitted to the 2MASS data. The initial mass function for this curve utilizes a double power law form, with $\alpha_{1,\text{IMF}} = 1.3$ for $0.1 < m/M_{\odot} < 0.5$ and $\alpha_{2,\text{IMF}} = 2.3$ for $0.5 < m/M_{\odot} < 100$ (e.g., Kroupa 2002). Though this stellar curve is not adjusted for internal extinction and may not be applicable to many galaxies in the sample, it is included as a fiducial reference against which deviations in the ultraviolet can be compared from galaxy to galaxy.

The spectral energy distributions for the LVL sample range widely. There are stellar-dominated (NGC 0404, UGC 05373, UGCA 0193) and comparatively dusty (IC 5256, NGC 6503) systems; for sources detected by MIPS, the infrared-to-far-ultraviolet ratio in the sample spans more than three orders of magnitude, from $\lesssim 0.1$ to over 100 (§ 5.5). There are galaxies with far-infrared spectral energy distributions indicative of warm (UGCA 0281) and cold dust grains (NGC 5055). Compared to what would be expected based on their stellar and far-infrared emission, many galaxies show a dearth of emission from PAHs in the $8.0 \mu\text{m}$ band (e.g., ESO 245-G005, UGC 01249, UGC 05272). The variations in global spectral energy distributions are discussed in more detail below.

5.4. Infrared Colors

The IRAC–MIPS infrared colors for the LVL sample are displayed in Panel a of Figure 11. The $f_{\nu}(70\mu\text{m})/f_{\nu}(160\mu\text{m})$ ratio typically traces the temperature of large interstellar grains, while the $f_{\nu}(8.0\mu\text{m})/f_{\nu}(24\mu\text{m})$ ratio has several influences. The flux at $24 \mu\text{m}$ mostly represents emission from very small grains (grains with effective radii of $15\text{--}40\text{\AA}$; Draine & Li 2007), and the flux at $8.0 \mu\text{m}$ can have contributions from stars, hot dust, PAHs, and AGN. Perhaps due to the diversity of emission mechanisms responsible for 8.0 and $24 \mu\text{m}$ flux levels, the $f_{\nu}(8.0\mu\text{m})/f_{\nu}(24\mu\text{m})$ ratio spans nearly two orders of magnitude compared to the single factor of ~ 10 stretch in the $f_{\nu}(70\mu\text{m})/f_{\nu}(160\mu\text{m})$ ratio. Since the local volume lacks “strong” AGN, loosely defined here as AGN that dominate a galaxy’s emission over substantial portions of the electromagnetic spectrum, it is unlikely that AGN contribute much to the scatter in Figure 11.

The $(42\text{--}122 \mu\text{m})$ far-infrared (*FIR*) and total infrared are frequently used as indications of the star formation rate in galaxies (Kennicutt 1998; Bell 2003). However, in many instances the far-infrared continuum is unavailable or not detected, so monochromatic infrared proxies for *FIR* or *TIR* are occasionally employed (e.g., Papovich & Bell 2002; Bavouzet et al. 2008). Hence, the tightness (dispersion) in monochromatic-to-bolometric ratios are of general interest. Five flavors of these ratios are displayed in the remaining panels of Figure 11, and a tabulation of median LVL infrared colors and monochromatic-to-bolometric infrared ratios can be found in Table 4 along with their dispersions. Panel b of Figure 11 shows the distribution of the $8.0 \mu\text{m}$ emission with respect to the $3\text{--}1100 \mu\text{m}$ total infrared, a distribution which exhibits a dispersion of 0.23 dex, similar to that for $f_{\nu}(70\mu\text{m})/f_{\nu}(160\mu\text{m})$ and $f_{\nu}(8.0\mu\text{m})/f_{\nu}(24\mu\text{m})$. While it is evident that the LVL sample is distributed fairly evenly by morphology across $f_{\nu}(70\mu\text{m})/f_{\nu}(160\mu\text{m})$ ratios, the bulk of the systems

exhibiting relatively low $f_{\nu}(8.0\mu\text{m})/f_{\nu}(24\mu\text{m})$ and $\nu f_{\nu}(8.0\mu\text{m})/TIR$ ratios are from late-type spirals and irregulars. Walter et al. (2007) also find somewhat unusual infrared colors for dwarf irregulars compared to normal spiral galaxies, and they attribute the difference to the lower dust content and higher dust temperatures in dwarf galaxies (see also Hirashita & Ichikawa 2009 and Muñoz-Mateos et al. 2009).

The preponderance of late-type spirals and irregulars showing relatively low $8.0\mu\text{m}$ emission is amplified when “dust-only” $8.0\mu\text{m}$ emission is considered. Panel e of Figure 11 shows a plot similar to that in Panel b but with the stellar emission removed using the expression presented in Helou et al. (2004):

$$\nu f_{\nu}(8.0\mu\text{m})_{\text{dust}} = \nu f_{\nu}(8.0\mu\text{m}) - \eta^{8*} \nu f_{\nu}(3.6\mu\text{m}) \quad (8)$$

where $\eta^{8*} = 0.232 \times 3.6/8.0$ (see also Engelbracht et al. 2008 for a similar scale factor). The dispersion (0.40 dex) and overall range are significantly larger when the dust-only $8.0\mu\text{m}$ emission is normalized to the total infrared. It is possible that a portion of these increases in dispersion and range is due to the inapplicability of Equation 8 to late-type spirals, but it should be noted that Equation 8 is based on a detailed analysis of NGC 300, a local system with an Sd morphological classification. Another possibility is that the late-type spirals and irregulars within LVL are on average less abundant in heavy metals, and thus either the formation of PAH molecules is starved or the relatively fragile PAHs are photo-dissociated in the hard radiation fields typically associated with low-metallicity environments (Engelbracht et al. 2005; Madden et al. 2006; Wu et al. 2006; Jackson et al. 2006; Draine et al. 2007; Sloan et al. 2008; Gordon et al. 2008; Dale et al. 2009). PAH emission from galaxies with normal metallicities, on the other hand, has been shown to correlate strongly with far-infrared and submillimeter emission (e.g., Haas, Klaas, & Bianchi 2002; Bendo et al. 2008). Figure 12 is similar to Figure 11 but the flux ratios are displayed as a function of absolute B magnitude. Although additional data and detailed follow-up utilizing LVL metallicities would be required to address this issue, clearly the lowest luminosity galaxies in the LVL sample are driving most of the scatter in $8\mu\text{m}$ -to- TIR measures.

In contrast to the $8.0\mu\text{m}$ -to- TIR measures, the $\nu f_{\nu}(24\mu\text{m})/TIR$ ratio (Panel d of Figure 11) shows a range less than an order of magnitude and a dispersion of 0.16 dex; the $70\mu\text{m}$ -to- TIR and $160\mu\text{m}$ -to- TIR ratios have even smaller dispersions (Panels c & f and Table 4). The implication is that, compared to the $8.0\mu\text{m}$ PAH emission from galaxies, the infrared emission from large grains at 70 and $160\mu\text{m}$ is far more tightly coupled to the bolometric infrared emission. The very small grain emission at $24\mu\text{m}$ shows an intermediate coupling to the total infrared, though these results may hinge on the relatively high percentage of low metallicity systems in the LVL sample.

The $70\mu\text{m}$ -to- TIR and $160\mu\text{m}$ -to- TIR ratios cling remarkably closely to the model predictions, with dispersions from the model of 0.039 and 0.032 dex, respectively. These tight dispersions reflect the importance of the 70 and $160\mu\text{m}$ fluxes in determining the total infrared using just MIPS data. However, there is evidence for a slightly increasing mismatch between model and data at the warmest far-infrared colors. This inconsistency may reflect the differences between the LVL sample and the sample used to construct the models (Dale et al. 2000). Galaxies in the LVL sample

typically have lower star formation rates (per area) and thus more of the infrared emission stems from cold dust grains emitting at longer wavelengths (e.g., 70 and 160 μm), leading to comparatively lower 24 μm /TIR and higher 70 μm /TIR and 160 μm /TIR ratios.

5.5. The Infrared-to-Ultraviolet Ratio and Ultraviolet Spectral Slope

The infrared-to-ultraviolet ratio is a measure of dust extinction in the ultraviolet for star-forming galaxies (e.g., Gordon et al. 2000), and thus should be related to the amount of reddening in their ultraviolet spectra. Indeed, starbursting galaxies follow a tight correlation between the ratio of infrared-to-ultraviolet emission and the ultraviolet spectral slope (e.g., Calzetti 1997; Meurer et al. 1999). Compared to the relation defined by starbursts, normal star-forming galaxies are offset to redder ultraviolet spectral slopes, exhibit lower infrared-to-ultraviolet ratios, and show significantly larger scatter (Buat et al. 2002, 2005; Bell 2002; Kong et al. 2004; Gordon et al. 2004; Burgarella et al. 2005; Calzetti et al. 2005; Seibert et al. 2005; Cortese et al. 2006; Boissier et al. 2007; Gil de Paz et al. 2007; Dale et al. 2007). Conversely, extremely dusty galaxies with infrared luminosities above $\sim 10^{11} L_{\odot}$ are known to be offset *above* the canonical starbursting relation, to higher dust extinction levels (Goldader et al. 2002). Offsets from the locus formed by starbursting galaxies can be particularly pronounced for systems lacking significant current star formation, such as elliptical galaxies, systems for which the luminosity is more dominated by a passively evolving older, redder stellar population. The LVL survey provides a unique sample for exploring the relationship between the infrared-to-ultraviolet ratio and the ultraviolet slope, as it consists of a statistically complete set of star-forming galaxies, nearly two-thirds of which are dwarf/irregular systems.

Figure 13 displays the LVL infrared-to-ultraviolet ratios as a function of the ultraviolet spectral slope. As expected, the well-known starbursts in the LVL sample lie close to the starburst curve: NGC 0253, NGC 4631, NGC 4449, NGC 1705, and NGC 4736, with the latter formally known as a post-starburst galaxy (Walker, Lebofsky, & Rieke 1988). Overall, the LVL population is broadly segregated in the infrared-to-ultraviolet ratio according to optical morphology, with Sb and earlier-type galaxies showing relatively high values, Sc/Sd/Sm systems exhibiting intermediate values, and the bulk of the relatively optically thin irregulars appearing near the bottom of the diagram and significantly below the more dust-obscured starburst galaxies. Interestingly, compared to the Cortese et al. (2006) normal galaxy curve shown in Figure 13, most LVL targets either have lower infrared-to-ultraviolet ratios for a given ultraviolet color, or are redder for a given infrared-to-ultraviolet ratio. Lower infrared-to-ultraviolet ratios could arise from the typically less dusty nature of dwarf/irregulars, or the patchy distribution of dust allowing a higher fraction of ultraviolet photons to escape (e.g., Dale et al. 2007; Muñoz-Mateos et al. 2009). Inspection of the imaging also shows that the (dust) infrared and H α emission is frequently more centrally concentrated than the ultraviolet emission, and thus comparing the *global* infrared and ultraviolet fluxes in galaxies with spatially-extended ultraviolet emission will result in artificially lowered infrared-to-ultraviolet ratios. Redder colors in LVL galaxies could be related to less efficient star formation capabilities in

less massive galaxies (e.g., Kauffmann, Wheeler, & Bullock 2007), as well as temporally-extended star formation histories suggested by the lack of widespread $H\alpha$ emission in many cases.

Differences in the infrared-to-ultraviolet ratio can be quantified according to the amount of dust extinction (e.g., Meurer et al. 1999; Gordon et al. 2000; Buat et al. 2005). The distribution of far-ultraviolet extinctions estimated by the infrared-to-ultraviolet-based prescription presented in Buat et al. (2005) is provided in Figure 14. Buat et al. derive their prescription by averaging over the results from many PEGASE-based model star formation histories (constant, burst, exponential decay) and dust attenuation configurations (foreground screen, clumpy mixture, etc.). The median far-ultraviolet extinction in the LVL sample using this method is 0.54 mag with ninety percent of the sources having far-ultraviolet extinctions less than 1.7 mag, or equivalently with the aid of the Li & Draine (2001) extinction curve, the median optical extinction is $A_V \sim 0.2$ mag and ninety percent have $A_V \lesssim 0.64$ mag.

To further explore possible correlations with the dominant stellar population and recent star formation history, Figure 15 provides two observable tracers of the “birthrate parameter” as a function of the (perpendicular or closest) distance to the starburst curve in Figure 15. The birthrate parameter is defined as the ratio of the current star formation rate to its overall lifetime average (Kennicutt et al. 1994), roughly the star formation rate per stellar mass, and thus provides a normalized measure of the star formation activity. Both the ratio of far-ultraviolet-to-near-infrared luminosity and the $H\alpha$ equivalent width have been previously used as tracers of the birthrate (e.g., Kennicutt et al. 1994; Boselli et al. 2001; Cortese et al. 2006; Lee et al. 2009b; Muñoz-Mateos et al. 2009). In the top panel of Figure 15 the far-ultraviolet, which tracks star formation averaged over the most recent ~ 100 Myr, is normalized by the near-infrared luminosity, which probes the total stellar mass built up over much longer timescales. The bottom panel of Figure 15 incorporates an observable indicator of the birthrate parameter that is much less affected by extinction: the $H\alpha$ equivalent width (taken from Kennicutt et al. 2008). This parameter is also a measure of the birthrate, since the $H\alpha$ flux is a measure of the line emission in H II regions primarily produced by massive ($> 10 M_\odot$) stars on ~ 3 – 20 Myr timescales (e.g., Kennicutt 1998; Meynet & Maeder 2000) while the red continuum emission near 6563 \AA that provides the normalization for the equivalent width traces the total mass of stars built up over much longer timescales. The $H\alpha$ equivalent widths shown here are measured over the entire extent of galaxies via narrowband and R band imaging (as opposed to spectroscopic measurements), and thus are representative of global, galaxy-averaged values.

Both panels of Figure 15 show a clear trend, with lower birthrate systems exhibiting larger distances from the starburst trend, consistent with the study of Kong et al. (2004). The deviations from the starburst curve are presumably driven by the differential effects that young and old stellar populations and their local dust opacities have on the age-reddened and dust-reddened luminosities, suggesting that a galaxy’s star formation history plays an important role in determining its location within Figure 13. To more directly interpret these deviations from the starburst curve as a function of the age of the stellar population, the righthand axis of the upper panel of Figure 15 is quantified

according to the age of a continuously star-forming system inferred from theoretical spectra. This comparison is accomplished by convolving *GALEX* far-ultraviolet and *Spitzer* 3.6 μm filter transmission profiles with stellar spectra similar to those described in § 5.3 but for a wide range of ages (1 Myr to 10 Gyr). The ages for the respective simulated spectra are shown along the righthand axis at levels corresponding to the computed theoretical far-ultraviolet-to-near-infrared ratios along the lefthand axis. Assuming these theoretical spectra and a continuous star formation are broadly applicable to the LVL sample, the ages range from several million years up to a few billion years, with the longest-lasting star formation episodes corresponding to the largest deviations from the starburst curve. It should be stressed that this comparison with theoretical stellar population ages is indicative—if the actual star formation rates have been declining with time instead of remaining constant, then the age axis in Figure 15 overestimates the true ages.

6. Summary

In this contribution we describe the Local Volume Legacy, a *Spitzer Space Telescope* infrared imaging program built upon a foundation of *GALEX* ultraviolet and ground-based $\text{H}\alpha$ imaging of 258 galaxies within 11 Mpc, approximately two-thirds of which are irregulars or dwarf spheroidals. The proximity and nearly volume-limited nature of the survey are key aspects to this program, enabling multi-wavelength analyses of star formation with high spatial resolution in a manner that is statistically representative of the nearby galaxy population. First results based primarily on the near-, mid-, and far-infrared data are reported here. Whereas monochromatic tracers of the far-infrared at 70 and 160 μm closely track the 3–1100 μm total-infrared emission, the mid-infrared-to-total-infrared ratios show large dispersions. The large scatter in comparing dust emission at 8.0 μm to the total dust emission is likely due to the notable deficiency of PAH emission from the low-metallicity, low-luminosity galaxies prevalent in the LVL survey. The LVL sample shows a correlation between infrared-to-ultraviolet ratio and ultraviolet spectral slope, but it is shifted to redder colors and/or lower infrared-to-ultraviolet ratios than what is seen for starbursting galaxies and most star-forming galaxies. In many instances the ~ 100 Myr ultraviolet emission is more spatially extended than the ~ 10 Myr (dust) infrared and $\text{H}\alpha$ emission, suggesting that the outer parts of many LVL galaxies are older than their inner regions. Thus, *global* flux ratios will naturally yield older (redder) and small infrared-to-ultraviolet ratios than is typically found in starbursts and normal star-forming galaxies. Theoretical models are utilized to buttress the idea that deviations from the starburst relation correspond to the age of the stellar population that drives the bulk of the ultraviolet luminosity.

Support for this work, part of the *Spitzer Space Telescope* Legacy Science Program, was provided by NASA and issued by the Jet Propulsion Laboratory, California Institute of Technology under NASA contract 1407. This research has made use of the NASA/IPAC Extragalactic Database which is operated by JPL/Caltech, under contract with NASA. This publication makes use of data

products from the Two Micron All Sky Survey, which is a joint project of the University of Massachusetts and the Infrared Processing and Analysis Center/California Institute of Technology, funded by the National Aeronautics and Space Administration and the National Science Foundation. IRAF, the Image Reduction and Analysis Facility, has been developed by the National Optical Astronomy Observatories and the Space Telescope Science Institute. We gratefully acknowledge NASA’s support for construction, operation, and science analysis for the GALEX mission, developed in cooperation with the Centre National d’Etudes Spatiales of France and the Korean Ministry of Science and Technology.

REFERENCES

- Bavouzet, N., Dole, H., Le Floch, E., Caputi, K.I., Lagache, G., & Kochanek, C.S. 2008, *A&A*, 479, 83
- Bell, E.F. 2002, *ApJ*, 577, 150
- Bell, E.F. 2003, *ApJ*, 586, 794
- Bernard, J.-P. et al. 2008, *AJ*, 136, 919
- Boissier, S. et al. 2007, *ApJS*, 173, 524
- Boselli, A., Gavazzi, G., Donas, J., & Scodeggio, M. 2001, 121, 753
- Buat, V. et al. 2001, *ApJ*, 619, L51
- Buat, V., Boselli, A., Gavazzi, G., & Bonfanti, C. 2002, *A&A*, 383, 801
- Buat, V. et al. 2005, *ApJ*, 619, L51
- Burgarella, D., Buat, V., & Iglesias-Páramo, J. 2005, *MNRAS*, 360, 1413
- Calzetti, D. 1995, Bohlin, R.C., Kinney, A.L., Storchi-Bergmann, T., & Heckman, T.M. 1995, *ApJ*, 443, 136
- Calzetti, D. 1997, *AJ*, 113, 162
- Calzetti, D. et al. 2005, *ApJ*, 633, 871
- Calzetti, D. et al. 2007, *ApJ*, 666, 870
- Cortese, L., Boselli, A., Buat, V., Gavazzi, G., Boissier, S., Gil de Paz, A., Seibert, M., Madore, B.F., & Martin, C. 2006, *ApJ*, 637, 242
- Dalcanton, J. et al. 2009, *ApJ*, in press
- Dale, D.A. et al. 2000, *AJ*, 120, 583

- Dale, D.A., Helou, G., Contursi, A., Silbermann, N.A., & Kolhatkar, S. 2001, *ApJ*, 549, 215
- Dale, D.A. & Helou, G. 2002, *ApJ*, 576, 159
- Dale, D.A. et al. 2007, *ApJ*, 655, 863
- Dale, D.A. et al. 2009, *ApJ*, 693, 1821
- Dole, H. et al. 2006, *A&A*, 451, 417
- Draine, B.T., & Li, A. 2007, *ApJ*, 657, 810
- Draine, B.T. et al. 2007, *ApJ*, 663, 866
- Draine, B.T. et al. 2009, in preparation
- Engelbracht, C.W., Gordon, K.D., Rieke, G.H., Werner, M.W., Dale, D.A., & Latter, W.B. 2005, *ApJ*, 628, L29
- Engelbracht, C.W. et al. 2007, *PASP*, 119, 914
- Engelbracht, C.W., Rieke, G.H., Gordon, K.D., Smith, J.-D.T., Werner, M.W., Moustakas, J., Willmer, C.N.A., & Vanzi, L. 2008, *ApJ*, 678, 804
- Farihi, J., Zuckerman, B., & Becklin, E.E. 2008, *ApJ*, 674, 431
- Fazio, G.G. et al. 2004, *ApJS*, 154, 10
- Fisher, K.B., Huchra, J.P., Strauss, M.A., Davis, M., Yahil, A., & Schlegel, D. *ApJS*, 100, 69
- Gil de Paz, A. et al. 2007, *ApJS*, 173, 185
- Gil de Paz, A. et al. 2009, in preparation
- Goldader, J.D., Meurer, G., Heckman, T.M., Seibert, M., Sanders, D.B., Calzetti, D., & Steidel, C.C. 2002, *ApJ*, 568,
- Gordon, K.D., Clayton, G.C. Witt, A.N., & Misselt, K.A. 2000, *ApJ*, 533, 236
- Gordon, K.D. et al. 2004, *ApJS*, 154, 215
- Gordon, K.D. et al. 2005, *PASP*, 117, 503
- Gordon, K.D. et al. 2007, *PASP*, 119, 1019
- Gordon, K.D., Engelbracht, C.W., Rieke, G.H., Misselt, K.A., Smith, J.D.T., & Kennicutt, R.C. 2008, *ApJ*, 682, 336
- Gordon, K.D. et al. 2009, in preparation

- Helou, G. et al. 2004, *ApJS*, 154, 253
- Hirashita, H. & Ichikawa, T.T. 2009, *MNRAS*, in press
- Jackson, D.C., Cannon, J.M., Skillman, E.D., Lee, H., Gehrz, R.D., Woodward, C.E., & Polomski, E. 2006, *ApJ*, 646, 192
- Jarrett, T.H., Chester, T., Cutri, R., Schneider, S.E., & Huchra, J.P. 2003, *AJ*, 125, 525
- Johnson, B. et al. 2009, in preparation
- Kaufmann, T., Wheeler, C. & Bullock, J.S. 2007, *MNRAS*, 382, 1187
- Kennicutt, R.C., Tamblyn, P., & Congdon, C.E. 1994, *ApJ*, 435, 22
- Kennicutt, R.C. 1998, *ARA&A*, 36, 189
- Kennicutt, R.C. et al. 2003, *PASP*, 115, 928
- Kennicutt, R.C. et al. 2007, *ApJ*, 671, 333
- Kennicutt, R.C., Lee, J.C., Funes, J.G., Sakai, S., & Akiyama, S. 2008, *ApJS*, 178, 247
- Kennicutt, R.C. et al. 2009, *ApJ*, submitted
- Kirby, E.M., Jerjen, H., Ryder, S.D., & Driver, S.P. 2008, *AJ*, 136, 1866
- Kong, X., Charlot, S., Brinchmann, J., & Fall, S.M. 2004, *MNRAS*, 349, 769
- Kroupa, P. 2002, *Science*, 295, 82
- Lee, J.C. 2006, Ph.D. thesis, University of Arizona
- Lee, J.C., Kennicutt, R.C., Funes, J.G., Sakai, S., & Akiyama, S. 2007, *ApJ*, 671, 113
- Lee, J.C. et al. 2009a, in preparation
- Lee, J.C., Kennicutt, R.C., Funes, J.G., Sakai, S., & Akiyama, S. 2009b, *ApJ*, 692, 1305
- Lee, H. et al. 2009c, in press
- Li, A. & Draine, B.T. 2001, *ApJ*, 554, 778
- Lisenfeld, U. 2007, *A&A*, 462, 507
- Madden, S.C., Galliano, F., Jones, A.P., & Sauvage, M. 2006, *A&A*, 446, 877
- Marble, A.R. et al. 2009, in preparation
- Meurer, G.R., Heckman, T.M., & Calzetti, D. 1999, *ApJ*, 521, 64

- Meynet, G. & Maeder, A. 2000, *A&A*, 361, 101
- Moshir, M. et al. 1990, *IRAS Faint Source Catalog*, version 2.0
- Muñoz-Mateos, J.C. et al. 2009, in preparation
- Papovich, C. & Bell, E.F. 2002, *ApJ*, 579, L1
- Reach, W.T. et al. 2005, *PASP*, 117, 978
- Regan, M. et al. 2006, *ApJ*, 652, 1112
- Rice, W., Lonsdale, C.J., Soifer, B.T., Neugebauer, G., Kopan, E.L., Lloyd, L.A., de Jong, T., & Habing, H.J. 1988, *ApJS*, 68, 91
- Rieke, G.H. et al. 2004, *ApJS*, 154, 25
- Ryan-Weber, E. et al. 2002, *AJ*, 124, 1954
- Sanders, D.B., Mazzarella, J.M., Kim, D.-C., Surace, J.A., & Soifer, B.T. 2003, *AJ*, 126, 1607
- Schlegel, D.J., Finkbeiner, D.P., & Davis, M. 1998, *ApJ*, 500, 525
- Seibert, M. et al. 2005, *ApJ*, 619, L55
- Sloan, G.C., Kraemer, K.E., Wood, P.R., Zijlstra, A.A., Bernard-Salas, J., Devost, D., & Houck, J.R. 2008, *ApJ*, 686, 1056
- Skrutskie, M.F. et al. 2006, *AJ*, 131, 1163
- Stansberry, J.A. et al. 2007, *PASP*, 119, 1038
- Staudaher, S. et al. 2009, in preparation
- Tully, R.B. 1988, *AJ*, 96, 73
- Walker, C.E., Lebofsky, M.J., & Rieke, G.H. 1988, *ApJ*, 325, 687
- Williams, B.F. et al. 2009, *AJ*, in press
- Wu, Y., Charmandaris, V., Hao, H., Brandl, B.R., Bernard-Salas, J., Spoon, H.W.W., & Houck, J.R. 2006, *ApJ*, 639, 157
- Vazquez, G.A. & Leitherer, C. 2005, *ApJ*, 621, 695
- Yan, L. et al. 2004, *ApJS*, 154, 60

Table 1. Galaxy Sample and Infrared Photometry Apertures

Galaxy	m_B (mag)	cz (km s ⁻¹)	D (Mpc)	T	$E(B-V)$ (mag)	α_0 & δ_0 (J2000)	$2a$ ($''$)	$2b$ ($''$)	PA ($^\circ$)	log(TIR) (L_\odot)
WLM	11.03	-116	0.92	10	0.04	000158.9–152655	672	340	0	6.7
NGC0024	12.19	554	8.13	5	0.02	000955.9–245755	301	216	225	8.8
NGC0045	11.32	471	7.07	8	0.02	001404.6–231101	577	456	336	8.9
NGC0055	8.42	129	2.17	9	0.01	001508.2–391256	2251	714	106	9.2
NGC0059	13.12	382	5.30	-3	0.02	001525.8–212646	256	180	302	7.5
ESO410-G005	14.95	...	1.90	-1	0.01	001530.3–321041	159	120	308	< 6.1
Sculptor-dE1	17.78	...	4.20	10	0.02	002351.6–244204	160	103	0	< 6.8
ESO294-G010	15.52	117	1.90	-3	0.01	002633.7–415120	165	102	0	< 6.1
IC1574	14.50	361	4.92	10	0.02	004303.9–221444	202	123	0	< 7.0
NGC0247	9.67	160	3.65	7	0.02	004708.9–204456	1476	581	352	9.0
NGC0253	8.04	241	3.94	5	0.02	004733.2–251734	2050	808	50	10.8
ESO540-G030	16.46	...	3.40	-1	0.02	004920.8–180406	168	148	0	< 6.7
UGCA015	15.38	301	3.34	10	0.02	004949.1–210049	150	78	28	< 6.5
ESO540-G032	16.55	...	3.40	-3	0.02	005024.6–195427	100	91	0	< 6.5
UGC00521	15.31	659	11.32	10	0.07	005112.2+120129	107	107	90	< 7.5
SMC ^a	2.70	158	0.06	9	0.42	8.0
NGC0300	8.72	144	2.00	7	0.01	005458.1–374054	1507	1128	114	8.9
UGC00668	9.88	-234	0.65	10	0.02	010450.5+020720	682	547	60	6.5
UGC00685	14.20	157	4.70	9	0.06	010723.2+164101	179	147	122	7.1
UGC00695	15.28	664	10.20	6	0.03	010746.5+010347	129	109	0	7.5
NGC404	11.51	-48	3.10	-1	0.06	010927.7+354307	210	210	90	7.8
UGC00891	14.72	643	10.84	9	0.03	012118.9+122438	194	118	42	7.4
UGC01056	14.87	595	10.32	10	0.07	012847.6+164117	125	117	0	7.4
UGC01104	14.41	686	7.50	9	0.06	013242.5+181906	166	103	0	7.2
NGC0598	6.27	-179	0.84	6	0.04	013350.8+303920	4453	2762	12	9.3
NGC0625	11.71	405	4.07	9	0.02	013504.4–412624	499	256	90	8.5
NGC0628	9.95	657	7.30	5	0.07	013642.4+154711	879	809	90	9.9
UGC01176	14.40	633	9.00	10	0.06	014010.0+155426	202	168	25	7.5
ESO245-G005	12.70	395	4.43	10	0.02	014503.6–433528	358	253	318	7.5
UGC01249	12.07	338	7.20	9	0.08	014729.5+271950	468	205	331	8.5
NGC0672	11.47	421	7.20	6	0.08	014752.7+272550	556	361	67	9.0
ESO245-G007	13.33	56	0.44	10	0.02	015106.1–442647	288	240	0	< 5.1
NGC0784	12.23	198	5.19	8	0.06	020116.7+285005	480	191	3	7.9
NGC855	13.30	595	9.73	-5	0.07	021403.9+275239	190	171	68	8.6
ESO115-G021	13.34	513	4.99	8	0.03	023746.8–612018	401	113	221	7.4
ESO154-G023	12.69	578	5.76	8	0.02	025652.4–543359	486	248	39	8.0
NGC1291	9.39	839	9.37	0	0.01	031719.1–410632	840	804	0	9.4
NGC1313	9.20	475	4.15	7	0.11	031810.0–662908	896	694	338	9.4
NGC1311	13.18	571	5.45	9	0.02	032006.9–521114	300	141	36	7.7
UGC02716	14.64	379	6.23	8	0.14	032407.9+174512	174	123	90	7.2
IC1959	13.26	640	6.06	9	0.01	033312.4–502445	253	114	330	7.9
NGC1487	12.34	848	9.08	7	0.01	035543.4–422157	430	261	70	9.0
NGC1510	13.47	913	9.84	-2	0.01	040332.7–432359	126	122	0	8.3
NGC1512	11.13	896	9.64	1	0.01	040355.6–432149	1002	928	83	9.4
NGC1522	13.93	905	9.32	11	0.01	040607.6–524011	151	99	37	8.3

Table 1—Continued

Galaxy	m_B (mag)	cz (km s ⁻¹)	D (Mpc)	T	$E(B-V)$ (mag)	α_0 & δ_0 (J2000)	$2a$ ($''$)	$2b$ ($''$)	PA ($^\circ$)	log(TIR) (L_\odot)
IC2049	15.19	869	16.73	7	0.02	041204.2–583327	119	106	0	7.7
ESO483-G013	14.18	823	10.43	–3	0.05	041240.9–230928	205	147	322	8.1
ESO158-G003	14.01	975	9.96	9	0.01	044615.6–572044	199	172	0	8.2
ESO119-G016	14.79	969	9.84	10	0.02	045128.6–613905	221	116	26	7.4
NGC1705	12.77	628	5.10	11	0.01	045413.5–532137	167	120	220	7.8
NGC1744	11.60	748	7.65	7	0.04	045957.8–260116	661	317	349	8.6
NGC1796	12.86	987	10.32	5	0.02	050242.8–610822	256	205	99	9.0
ESO486-G021	14.47	865	8.89	2	0.03	050319.9–252524	115	99	90	7.8
MCG-05-13-004 ^b	13.22	686	6.63	9	0.01	0.0
NGC1800	13.07	803	8.24	9	0.01	050625.7–315715	229	163	107	8.3
UGCA106	13.05	933	9.77	9	0.02	051159.2–325817	323	245	14	8.5
LMC ^a	0.91	278	0.05	9	0.92	8.9
KKH037	16.40	–148	3.39	10	0.07	064744.2+800723	105	81	90	< 6.4
NGC2366	11.43	100	3.19	10	0.04	072845.9+691202	617	315	31	8.1
UGCA133	15.80	...	3.20	–3	0.04	073412.2+665313	215	153	0	< 6.7
NGC2403	8.93	131	3.22	6	0.04	073655.1+653534	1512	930	304	9.5
NGC2500	12.20	514	7.63	7	0.04	080152.4+504405	274	234	75	8.9
NGC2537	12.82	447	6.90	9	0.05	081314.7+455936	211	199	0	8.7
UGC04278	13.07	565	7.59	7	0.05	081358.7+454445	319	79	351	8.1
UGC04305	11.10	157	3.39	10	0.03	081910.8+704320	555	465	60	7.9
NGC2552	12.56	524	7.65	9	0.05	081920.0+500038	312	205	54	8.3
M81dwA	18.69	113	3.55	10	0.02	082356.0+710145	78	78	90	6.4
UGC04426	15.00	397	10.28	10	0.04	082828.4+415124	206	145	10	< 7.7
UGC04459	14.78	19	3.56	10	0.04	083406.8+661036	134	111	120	7.0
UGC04483	15.27	178	3.21	10	0.03	083703.5+694632	94	58	0	< 6.5
NGC2683	10.64	411	7.70	3	0.03	085241.0+332516	822	420	41	9.6
UGC04704	15.33	596	7.75	8	0.03	085902.5+391223	303	108	296	7.4
UGC04787	15.41	552	6.53	8	0.02	090735.1+331638	211	107	5	7.4
UGC04998	14.72	623	10.50	10	0.06	092512.9+682258	187	162	71	< 7.7
NGC2903	9.68	556	8.90	4	0.03	093210.9+213005	824	461	17	10.3
UGC05076	15.21	571	8.31	10	0.02	093236.5+515216	165	139	90	< 7.4
CGCG035-007	15.46	574	5.17	5	0.04	093444.9+062532	126	96	63	6.8
UGC05139	14.17	143	3.84	10	0.05	094033.6+711120	264	219	63	7.0
IC0559	14.82	513	4.93	5	0.03	094443.9+093655	135	124	63	6.8
F8D1	16.14	...	3.80	–3	0.11	094447.1+672619	254	254	90	< 7.0
[FM2000]1	17.80	...	3.40	–3	0.08	094510.0+684547	89	89	90	< 6.4
NGC2976	11.24	3	3.56	5	0.07	094715.9+675507	457	312	322	8.9
LEDA166101	16.94	...	3.50	–3	0.14	095013.0+673037	219	152	33	< 6.8
UGC05272	15.41	520	7.10	10	0.02	095023.1+312917	196	96	112	7.5
UGC05288	14.32	557	6.80	8	0.03	095116.9+074939	164	141	331	7.4
BK03N	18.78	–40	4.02	10	0.08	095348.5+685808	41	41	90	< 6.2
NGC3031	7.89	–34	3.63	2	0.08	095531.8+690403	1629	1123	154	9.7
NGC3034	9.30	203	3.53	7	0.16	095552.1+694057	698	581	65	10.7
UGC05340	14.76	503	5.90	10	0.02	095645.3+284910	174	99	10	< 7.1
KDG061	15.17	–135	3.60	8	0.07	095704.5+683536	214	119	49	< 6.7

Table 1—Continued

Galaxy	m_B (mag)	cz (km s ⁻¹)	D (Mpc)	T	$E(B-V)$ (mag)	α_0 & δ_0 (J2000)	$2a$ ($''$)	$2b$ ($''$)	PA ($^\circ$)	log(TIR) (L_\odot)
UGC05336	14.30	46	3.70	10	0.08	095729.2+690250	248	181	220	6.5
Arp's Loop	16.76	99	3.90	10	0.08	095732.7+691700	137	137	90	< 6.7
UGC05364	12.92	20	0.69	10	0.02	095926.5+304458	311	192	67	< 5.5
UGC05373	11.85	301	1.44	10	0.03	095959.5+051957	333	268	90	5.9
KKH057	17.95	...	3.90	-3	0.02	100014.6+631058	73	53	45	< 6.4
UGCA193	14.84	662	9.70	7	0.04	100236.4-060031	284	69	14	7.0
NGC3109	10.39	403	1.34	9	0.07	100307.6-260946	1595	348	91	7.5
NGC3077	10.61	14	3.82	6	0.07	100319.2+684401	576	483	64	8.9
AM1001-270	16.51	362	1.30	10	0.08	100403.0-271948	169	96	319	< 5.8
BK05N	17.77	...	3.80	-3	0.06	100441.6+681526	207	102	330	< 6.7
UGC05428	15.95	-129	3.50	10	0.10	100507.5+663339	196	168	90	< 6.8
UGC05423	15.20	350	5.30	10	0.08	100531.3+702152	107	70	140	6.9
UGC05442	15.78	-18	3.70	-3	0.05	100701.2+674938	197	124	34	< 6.7
UGC05456	13.72	544	3.80	5	0.04	100719.4+102151	161	121	322	7.3
IKN	17.31	...	3.70	-3	0.06	100805.9+682357	180	156	180	< 6.8
Sextans A	11.86	324	1.32	10	0.04	101100.6-044141	408	315	35	6.5
[HS98]117	17.01	-37	4.00	10	0.12	102125.5+710652	213	129	0	< 6.8
NGC3239	11.73	753	8.29	9	0.03	102504.7+170856	315	272	63	9.0
DDO078	15.84	55	3.70	-3	0.02	102627.4+673916	141	141	90	< 6.7
UGC05672	15.14	531	6.30	5	0.02	102820.9+223409	289	104	340	7.3
UGC05666	10.80	57	4.02	9	0.04	102823.9+682505	864	486	59	8.4
UGC05692	13.71	180	4.00	9	0.04	103036.4+703713	306	211	0	7.1
NGC3274	13.21	537	6.50	7	0.02	103216.1+274008	347	142	110	8.1
BK06N	16.85	...	3.80	-3	0.01	103432.4+660036	231	108	304	< 6.8
NGC3299	14.11	641	10.40	8	0.02	103623.8+124231	264	207	0	8.1
UGC05764	15.21	586	7.08	10	0.02	103643.1+313245	150	85	44	6.9
UGC05797	15.00	713	6.84	10	0.03	103925.4+014302	141	138	0	7.2
UGC05829	13.73	629	7.88	10	0.02	104242.3+342730	285	252	20	8.0
NGC3344	10.45	586	6.64	4	0.03	104331.4+245531	514	448	330	9.4
NGC3351	10.53	778	10.00	3	0.03	104357.5+114219	586	457	10	9.9
NGC3368	10.11	897	10.52	2	0.03	104645.5+114905	511	349	346	9.8
UGC05889	14.22	572	9.30	9	0.03	104722.2+140416	202	190	0	< 7.7
UGC05923	14.03	712	7.16	0	0.03	104907.5+065504	97	60	353	7.4
UGC05918	15.22	340	7.40	10	0.01	104936.5+653149	140	113	65	< 7.3
NGC3432	11.67	616	7.89	9	0.01	105232.7+363747	476	187	38	9.2
KDG73	17.28	-132	3.70	10	0.02	105256.5+693317	126	100	345	< 6.6
NGC3486	11.05	681	8.24	5	0.02	110023.2+285834	495	389	83	9.4
NGC3510	14.30	705	8.57	8	0.03	110343.6+285301	310	136	345	8.3
NGC3521	9.83	805	8.03	4	0.06	110548.7-000222	767	494	343	10.2
NGC3593	11.86	628	6.52	0	0.02	111436.7+124903	373	211	86	9.4
NGC3623	10.25	807	8.95	1	0.02	111856.0+130525	663	331	352	9.5
NGC3627	9.65	727	10.05	3	0.03	112013.4+125927	746	487	347	10.5
NGC3628	10.28	843	9.45	3	0.03	112014.8+133518	1039	619	102	10.4
UGC06457	15.00	963	10.24	10	0.03	112712.4-005944	150	111	19	7.4
UGC06541	14.40	249	3.89	11	0.02	113328.1+491428	124	87	316	6.6

Table 1—Continued

Galaxy	m_B (mag)	cz (km s ⁻¹)	D (Mpc)	T	$E(B-V)$ (mag)	α_0 & δ_0 (J2000)	$2a$ ($''$)	$2b$ ($''$)	PA ($^\circ$)	log(TIR) (L_\odot)
NGC3738	11.97	229	4.90	10	0.01	113548.6+543129	220	175	343	8.2
NGC3741	14.49	229	3.19	10	0.02	113605.9+451706	201	108	10	6.5
UGC06782	15.07	525	14.00	9	0.03	114857.4+235016	135	114	115	< 7.8
UGC06817	13.56	242	2.64	10	0.03	115050.0+385245	270	144	65	6.4
UGC06900	14.80	590	7.47	10	0.02	115539.9+313106	204	145	107	< 7.4
NGC4020	13.82	760	9.68	7	0.02	115856.5+302442	222	136	18	8.6
NGC4068	13.02	210	4.31	10	0.02	120402.8+523523	255	178	22	7.5
NGC4080	14.28	567	6.92	10	0.03	120451.8+265932	153	131	312	7.9
NGC4096	11.48	566	8.28	5	0.02	120600.3+472847	556	243	18	9.5
NGC4144	12.05	265	9.80	6	0.01	120958.9+462730	437	189	103	8.8
NGC4163	13.75	165	2.96	10	0.02	121208.9+361008	213	164	4	6.6
NGC4190	13.90	228	3.50	10	0.03	121344.6+363808	210	164	45	7.2
ESO321-G014	15.63	610	3.20	10	0.09	121349.3+381347	171	105	22	< 6.5
UGC07242	14.65	68	5.42	6	0.02	121408.4+660541	157	85	0	< 7.0
UGCA276	15.70	284	3.18	10	0.02	121459.9+361301	161	143	301	< 6.6
UGC07267	15.29	472	7.33	8	0.02	121523.9+512104	189	98	45	7.1
NGC4214	10.24	291	2.92	10	0.02	121538.1+361935	624	567	0	8.8
CGCG269-049	15.30	159	3.23	10	0.02	121547.3+522315	94	67	319	< 6.3
NGC4236	10.05	0	4.45	8	0.01	121643.2+692719	1241	369	342	8.7
NGC4244	10.88	244	4.49	6	0.02	121729.8+374825	1182	242	47	8.8
NGC4242	11.37	517	7.43	8	0.01	121730.4+453710	410	312	28	8.7
UGC07321	14.15	408	20.00	7	0.03	121734.3+223225	370	78	81	9.0
NGC4248	13.21	484	7.24	3	0.02	121750.7+472432	251	170	107	8.0
NGC4258	9.10	448	7.98	4	0.02	121854.9+471824	1242	531	332	10.0
ISZ399	14.72	900	8.97	11	0.06	121959.5+172331	132	102	314	8.8
NGC4288	13.26	535	7.67	7	0.01	122038.3+461737	190	163	139	8.4
UGC07408	13.35	462	6.87	9	0.01	122115.5+454900	220	192	90	< 7.4
UGC07490	13.05	465	8.40	9	0.02	122424.6+701958	226	220	0	8.1
NGC4395	10.64	319	4.61	9	0.02	122552.2+333315	1008	790	328	8.9
UGCA281	15.36	281	5.70	11	0.01	122616.7+482939	87	73	81	7.5
UGC07559	14.20	218	4.87	10	0.01	122706.8+370822	240	132	307	6.9
UGC07577	12.84	196	2.74	10	0.02	122743.4+432926	270	180	301	6.6
NGC4449	9.99	207	4.21	10	0.02	122810.4+440525	473	354	57	9.4
UGC07599	14.88	278	6.90	8	0.02	122828.0+371404	120	72	306	< 7.1
UGC07605	14.79	309	4.43	10	0.01	122838.4+354301	141	86	17	< 6.7
NGC4455	13.80	637	7.75	7	0.02	122844.0+224918	200	90	198	8.2
UGC07608	13.67	538	7.76	10	0.02	122843.0+431328	210	207	0	7.7
NGC4460	12.78	490	9.59	-1	0.02	122845.9+445157	338	147	37	9.0
UGC07639	13.99	382	8.00	10	0.01	122953.3+473154	231	140	334	7.2
NGC4485	12.32	493	7.07	10	0.02	123031.8+414202	180	134	343	8.8
NGC4490	10.22	565	8.03	7	0.02	123034.4+413841	418	232	121	10.1
UGC07690	13.10	537	7.73	10	0.03	123226.8+424225	195	151	36	8.1
UGC07699	13.60	496	6.85	6	0.01	123248.0+373718	270	105	32	8.0
UGC07698	13.00	331	6.10	10	0.02	123255.3+313215	279	189	9	7.4
UGC07719	15.33	678	9.39	8	0.02	123400.6+390116	158	86	347	7.6

Table 1—Continued

Galaxy	m_B (mag)	cz (km s ⁻¹)	D (Mpc)	T	$E(B-V)$ (mag)	α_0 & δ_0 (J2000)	$2a$ ($''$)	$2b$ ($''$)	PA ($^\circ$)	log(TIR) (L_\odot)
UGC07774	15.02	526	7.44	7	0.02	123622.8+400019	201	57	100	7.4
UGCA292	16.10	307	3.10	10	0.02	123840.7+324605	115	75	0	< 6.3
NGC4594	8.98	1024	9.33	1	0.05	123959.4–113714	555	233	90	9.6
NGC4605	10.89	143	5.47	5	0.01	123958.9+613628	498	330	303	9.2
NGC4618	11.22	544	7.79	8	0.02	124133.3+410841	335	267	22	9.2
NGC4625	12.92	609	8.65	9	0.02	124154.8+411623	299	214	280	8.7
NGC4631	9.75	606	8.05	7	0.02	124203.7+323205	953	540	80	10.4
UGC07866	13.71	354	4.57	10	0.02	124215.0+383014	196	173	357	7.0
NGC4656	10.96	646	8.59	9	0.01	124356.2+320930	719	255	220	9.2
UGC07916	15.00	607	8.21	10	0.02	124425.8+342314	153	99	170	7.3
UGC07950	15.10	502	7.91	10	0.02	124656.2+513649	144	124	0	7.7
UGC07949	15.12	333	9.90	10	0.02	124659.5+362843	165	99	24	< 7.5
NGC4707	13.40	468	7.44	9	0.01	124823.3+510952	207	177	20	7.6
NGC4736	8.99	308	4.66	2	0.02	125056.7+410706	1033	825	100	9.8
UGC08024	13.94	374	4.30	10	0.01	125405.2+270854	199	126	213	< 6.7
NGC4826	9.36	408	7.50	2	0.04	125642.8+214050	723	449	113	9.9
UGC08091	14.68	214	2.13	10	0.03	125839.7+141306	125	92	32	6.0
UGCA319	14.96	747	7.40	9	0.08	130214.4–171417	130	90	24	< 7.2
UGCA320	13.52	744	7.24	9	0.08	130317.0–172529	491	163	114	7.7
UGC08188	12.40	321	4.49	9	0.01	130550.8+373615	379	326	90	7.9
UGC08201	12.80	37	4.57	10	0.02	130625.0+674226	268	150	90	6.8
MCG-03-34-002	14.79	922	10.16	4	0.08	130756.6–164120	130	80	320	7.4
UGC08245	15.22	70	3.64	10	0.03	130835.3+785612	191	100	70	6.6
NGC5023	12.85	407	5.40	6	0.02	131211.7+440221	410	127	26	8.0
CGCG217-018	15.10	570	8.21	10	0.01	131251.6+403232	114	87	35	7.4
UGC08313	14.78	625	8.72	5	0.01	131354.3+421231	191	114	30	7.7
UGC08320	13.11	192	4.33	10	0.02	131426.5+455527	292	198	341	7.4
UGC08331	14.31	260	8.20	10	0.01	131529.6+473004	236	115	323	7.5
NGC5055	9.31	504	7.55	4	0.02	131549.2+420147	1098	712	80	10.3
NGC5068	10.70	673	6.24	6	0.10	131855.4–210212	613	593	90	9.5
IC4247	14.57	274	4.97	2	0.06	132644.2–302143	129	78	333	6.7
NGC5204	11.73	201	4.65	9	0.01	132936.0+582510	338	211	351	8.4
NGC5194	8.96	463	8.00	4	0.04	132950.6+471307	1699	1130	15	10.6
NGC5195	10.45	465	8.00	2	0.04	132959.4+471556	203	192	0	9.3
UGC08508	13.94	62	2.69	10	0.02	133043.1+545436	160	120	305	6.4
NGC5229	14.18	364	5.10	7	0.02	133402.9+475452	279	102	347	7.4
NGC5238	13.60	235	5.20	8	0.01	133442.8+513650	216	166	0	7.5
[KK98]208	14.30	381	4.68	10	0.04	133635.5–293417	360	150	57	< 7.1
NGC5236	8.20	516	4.47	5	0.07	133700.8–295224	1100	1055	0	10.4
ESO444-G084	15.48	587	4.61	10	0.07	133720.7–280248	126	88	310	6.5
UGC08638	15.10	274	4.27	10	0.01	133919.4+244634	179	132	73	6.8
UGC08651	14.45	201	3.02	10	0.01	133953.5+404423	194	140	59	6.3
NGC5253	10.87	404	3.15	11	0.06	133956.1–313832	351	193	44	0.0
NGC5264	12.60	478	4.53	9	0.05	134136.0–295448	268	226	66	7.7
UGC08760	14.45	193	3.24	10	0.02	135051.3+380113	216	113	29	< 6.6

Table 1—Continued

Galaxy	m_B (mag)	cz (km s ⁻¹)	D (Mpc)	T	$E(B-V)$ (mag)	α_0 & δ_0 (J2000)	$2a$ ($''$)	$2b$ ($''$)	PA ($^\circ$)	log(TIR) (L_\odot)
KKH086	16.99	287	2.60	10	0.03	135433.8+041443	131	83	0	< 6.3
UGC08837	13.71	144	8.30	10	0.01	135444.0+535347	364	148	17	7.8
UGC08833	15.15	228	3.20	10	0.01	135448.4+355018	121	115	0	< 6.5
NGC5457	8.31	241	6.70	6	0.01	140325.0+542429	1800	1446	37	10.4
NGC5474	11.82	273	7.20	6	0.01	140500.8+533920	413	373	90	8.8
NGC5477	14.24	304	7.70	9	0.01	140533.0+542732	169	124	64	7.7
[KK98]230	17.84	62	2.14	10	0.01	140710.4+350335	67	49	0	< 5.8
UGC09128	14.46	154	2.24	10	0.02	141556.8+230321	127	88	36	< 6.1
NGC5585	11.20	305	5.70	7	0.02	141948.4+564349	392	266	38	8.5
UGC09240	13.31	150	2.80	10	0.01	142443.4+443134	222	182	90	6.8
UGC09405	14.57	222	8.00	10	0.01	143524.0+571516	199	136	333	7.1
MRK475	15.46	583	9.02	11	0.01	143905.5+364819	72	71	196	7.2
NGC5832	14.09	447	8.74	3	0.03	145747.6+714056	293	180	49	8.4
NGC5949	13.37	435	8.53	4	0.02	152800.3+644548	219	135	324	8.8
UGC09992	14.86	427	8.56	10	0.04	154147.9+671515	156	109	340	7.3
KKR25	16.53	-139	1.90	10	0.01	161347.6+542216	94	87	0	< 5.9
NGC6503	10.91	60	5.27	6	0.03	174923.7+700840	639	231	119	9.1
IC4951	13.91	794	9.34	8	0.04	200931.8-615104	225	92	355	7.7
DDO210	14.14	-137	0.94	10	0.05	204651.5-125047	160	77	103	< 5.4
IC5052	11.79	598	5.86	7	0.05	205206.0-691201	450	168	323	8.7
NGC7064	13.10	797	9.86	5	0.01	212903.4-524605	250	81	90	8.3
NGC7090	11.33	857	10.41	5	0.02	213628.8-543320	539	161	308	9.6
IC5152	10.68	124	1.97	10	0.03	220242.0-511741	312	274	90	7.8
IC5256	14.58	950	10.76	8	0.03	224945.4-684127	124	76	22	8.0
UGCA438	14.67	62	2.22	10	0.01	232627.4-322317	189	163	0	< 6.4
ESO347-G017	14.41	690	9.37	9	0.02	232655.9-372050	212	129	90	7.7
UGC12613	12.50	-183	0.76	10	0.07	232833.7+144437	461	269	113	5.9
IC5332	11.21	706	9.53	7	0.02	233427.6-360601	645	573	0	9.3
NGC7713	11.51	689	9.28	7	0.02	233615.4-375616	370	227	345	9.1
UGCA442	13.60	267	4.27	9	0.02	234346.7-315724	245	117	43	6.9
KKH098	17.22	-137	2.50	10	0.12	234534.1+384301	126	79	5	< 6.2
ESO149-G003	15.04	594	6.40	10	0.01	235202.4-523428	249	100	332	< 7.2
NGC7793	9.63	230	3.91	7	0.02	235750.4-323530	755	499	90	9.3

Note. — Magnitudes, heliocentric redshifts, distances, and optical morphologies are from Kennicutt et al. (2008), and the Milky Way foreground extinctions are from Schlegel, Finkbeiner, & Davis(1998). The remaining columns define the elliptical apertures used for the photometry presented in Table 2; the position angles are measured east of north.

^aInfrared photometry for the Large and Small Magellanic Clouds are from Bernard et al. (2008) and Gordon et al. (2009), respectively.

^bNGC 1800 and MCG-05-13-004 spatially overlap so separate photometry for MCG-05-13-004 is not provided.

Table 2. Infrared Flux Densities

Galaxy	2MASS J 1.25 μm (Jy)	2MASS H 1.65 μm (Jy)	2MASS K _s 2.17 μm (Jy)	IRAC 3.6 μm (Jy)	IRAC 4.5 μm (Jy)	IRAC 5.8 μm (Jy)	IRAC 8.0 μm (Jy)	MIPS 24 μm (Jy)	MIPS 70 μm (Jy)	
WLM ^{e f}	2.45±0.15E-1	3.13±0.20E-1	1.17±0.16E-1	9.09±1.23E-2	6.28±0.86E-2	4.87±0.62E-2	5.07±0.63E-2	7.57±0.82E-2	2.01±0.25E+0	3.
NGC0024 ^{e f}	2.32±0.12E-1	2.49±0.14E-1	1.90±0.12E-1	1.04±0.14E-1	7.06±1.01E-2	8.81±1.16E-2	1.28±0.16E-1	1.20±0.13E-1	2.23±0.27E+0	7.
NGC0045	2.08±0.13E-1	2.29±0.17E-1	1.67±0.18E-1	2.00±0.27E-1	1.27±0.17E-1	6.56±0.83E-2	1.69±0.21E-1	1.88±0.20E-1	3.86±0.47E+0	1.
NGC0055 ^{e f}	3.31±0.17E+0	3.08±0.16E+0	2.63±0.14E+0	2.03±0.27E+0	1.40±0.19E+0	1.50±0.19E+0	2.28±0.28E+0	6.29±0.68E+0	1.26±0.15E+2	2.
NGC0059	8.48±0.55E-2	1.13±0.08E-1	6.36±0.72E-2	3.29±0.45E-2	2.23±0.31E-2	1.57±0.20E-2	1.18±0.15E-2	4.40±0.47E-2	5.17±0.64E-1	4.
ESO410-G005	<1.08E-2	<1.61E-2	<1.97E-2	1.39±0.19E-2	5.71±0.79E-3	8.41±1.11E-3	5.25±0.67E-3	<6.11E-3	<8.24E-2	
Sculptor-dE1	<5.04E-3	<7.50E-3	<9.14E-3	<2.80E-4	<4.30E-4	<1.56E-3	<1.70E-3	<5.68E-3	<7.66E-2	
ESO294-G010	1.73±0.23E-2	2.12±0.34E-2	1.35±0.39E-2	4.79±0.65E-3	3.12±0.43E-3	<1.56E-3	<1.71E-3	<5.69E-3	<7.68E-2	
IC1574	1.96±0.28E-2	2.18±0.41E-2	1.55±0.48E-2	5.92±0.80E-3	3.93±0.54E-3	2.61±0.35E-3	1.74±0.24E-3	<6.97E-3	<9.40E-2	
NGC0247	1.47±0.07E+0	1.30±0.07E+0	1.02±0.06E+0	8.54±1.15E-1	5.89±0.81E-1	6.11±0.76E-1	8.48±1.06E-1	9.88±1.06E-1	1.57±0.19E+1	6.
NGC0253 ^{e e}	2.11±0.11E+1	2.53±0.13E+1	2.23±0.11E+1	1.23±0.17E+1	8.25±1.13E+0	1.94±0.24E+1	3.86±0.48E+1	1.46±0.16E+2	1.41±0.17E+3	1.
ESO540-G030	<6.22E-3	<9.23E-3	<1.12E-2	2.17±0.29E-3	1.58±0.22E-3	<1.91E-3	<2.09E-3	<6.96E-3	<9.38E-2	
UGCA015	6.42±1.80E-3	9.01±2.72E-3	4.27±2.43E-3	2.11±0.29E-3	1.67±0.23E-3	6.10±1.10E-4	3.60±0.80E-4	<4.78E-3	<6.45E-2	
ESO540-G032	4.75±1.58E-3	1.15±0.24E-2	<6.81E-3	1.46±0.20E-3	7.60±1.10E-4	<1.16E-3	<1.27E-3	<4.22E-3	<5.69E-2	
UGC00521	8.60±1.86E-3	9.60±2.75E-3	5.42±2.88E-3	3.01±0.41E-3	2.24±0.31E-3	1.04±0.14E-3	1.16±0.15E-3	3.47±0.40E-3	5.28±0.78E-2	
SMC ^{a e f}	2.74±0.46E+2	2.07±0.35E+2	...	1.48±0.24E+2	3.51±0.33E+2	1.12±0.13E+4	2.
NGC0300	3.26±0.16E+0	3.27±0.17E+0	2.52±0.13E+0	1.63±0.22E+0	1.20±0.16E+0	1.25±0.16E+0	2.02±0.25E+0	2.50±0.27E+0	4.62±0.56E+1	1.
UGC00668 ^{e f}	3.05±0.18E-1	4.74±0.28E-1	2.32±0.22E-1	1.24±0.17E-1	9.08±1.25E-2	3.34±0.42E-2	7.13±0.89E-2	8.64±0.93E-2	2.46±0.30E+0	5.
UGC00685	4.20±0.34E-2	2.28±0.43E-2	<1.16E-2	1.14±0.16E-2	7.48±1.03E-3	4.26±0.56E-3	5.29±0.67E-3	9.98±1.10E-3	1.61±0.21E-1	3.
UGC00695	9.45±2.01E-3	9.99±2.99E-3	<8.45E-3	4.45±0.60E-3	3.02±0.41E-3	1.83±0.25E-3	1.47±0.20E-3	2.52±0.32E-3	1.53±0.19E-1	1.
NGC0404 ^e	8.10±0.41E-1	8.41±0.42E-1	6.76±0.34E-1	4.38±0.59E-1	2.39±0.33E-1	2.16±0.28E-1	1.51±0.19E-1	1.45±0.16E-1	2.93±0.36E+0	3.
UGC00891	2.43±0.28E-2	1.34±0.38E-2	1.55±0.46E-2	5.89±0.80E-3	4.03±0.55E-3	1.82±0.26E-3	3.59±0.46E-3	4.45±0.52E-3	6.75±1.03E-2	1.
UGC01056	1.77±0.22E-2	2.60±0.34E-2	2.91±0.40E-2	5.58±0.76E-3	4.14±0.57E-3	2.62±0.35E-3	4.20±0.53E-3	6.29±0.70E-3	1.08±0.14E-1	4.
UGC01104	2.02±0.24E-2	2.11±0.35E-2	1.58±0.41E-2	8.28±1.12E-3	5.53±0.76E-3	3.45±0.46E-3	4.84±0.61E-3	4.46±0.51E-3	1.38±0.18E-1	1.
NGC0598 ^{e f}	2.12±0.11E+1	2.12±0.11E+1	1.67±0.08E+1	1.97±0.27E+1	1.39±0.19E+1	1.29±0.16E+1	2.78±0.35E+1	4.81±0.52E+1	7.90±0.96E+2	2.
NGC0625	2.83±0.15E-1	2.97±0.17E-1	2.42±0.16E-1	1.23±0.17E-1	8.83±1.21E-2	9.21±1.17E-2	1.38±0.17E-1	8.79±0.95E-1	6.79±0.83E+0	8.
NGC0628 ^{e f}	1.66±0.08E+0	1.67±0.09E+0	1.32±0.07E+0	8.72±1.18E-1	5.45±0.75E-1	1.14±0.15E+0	2.70±0.34E+0	3.25±0.35E+0	3.39±0.41E+1	1.
UGC01176	<1.50E-2	<2.21E-2	<2.66E-2	8.29±1.12E-3	6.22±0.85E-3	4.45±0.59E-3	4.40±0.56E-3	8.76±0.98E-3	9.11±1.35E-2	2.
ESO245-G005	5.02±0.55E-2	5.90±0.80E-2	4.14±0.93E-2	2.18±0.30E-2	1.53±0.21E-2	1.79±0.23E-2	7.75±0.98E-3	2.47±0.27E-2	5.95±0.74E-1	1.
UGC01249	1.05±0.07E-1	1.73±0.12E-1	8.91±1.05E-2	5.39±0.73E-2	3.41±0.47E-2	3.36±0.43E-2	2.45±0.31E-2	8.70±0.94E-2	1.87±0.23E+0	4.
NGC0672	3.59±0.20E-1	3.66±0.22E-1	2.96±0.20E-1	1.52±0.21E-1	1.18±0.16E-1	1.16±0.15E-1	1.16±0.14E-1	3.38±0.36E-1	5.90±0.72E+0	1.
ESO245-G007 ^f	4.34±0.48E-2	3.61±0.68E-2	<1.87E-2	1.72±0.23E-2	1.25±0.17E-2	<3.20E-3	<3.49E-3	<1.16E-2	<1.57E-1	
NGC0784	1.03±0.07E-1	1.02±0.09E-1	7.22±0.99E-2	4.98±0.67E-2	3.50±0.48E-2	2.69±0.34E-2	1.52±0.19E-2	4.94±0.53E-2	1.14±0.14E+0	1.

Table 2—Continued

Galaxy	2MASS J 1.25 μm (Jy)	2MASS H 1.65 μm (Jy)	2MASS K _s 2.17 μm (Jy)	IRAC 3.6 μm (Jy)	IRAC 4.5 μm (Jy)	IRAC 5.8 μm (Jy)	IRAC 8.0 μm (Jy)	MIPS 24 μm (Jy)	MIPS 70 μm (Jy)
NGC0855 ^{e f}	9.07±0.55E-2	9.78±0.67E-2	7.97±0.68E-2	4.24±0.60E-2	2.75±0.39E-2	1.83±0.30E-2	4.57±0.57E-2	8.55±0.92E-2	1.69±0.21E+0
ESO115-G021	5.85±0.46E-2	6.67±0.62E-2	4.17±0.67E-2	1.83±0.25E-2	1.23±0.17E-2	9.03±1.17E-3	7.85±0.99E-3	1.66±0.18E-2	3.55±0.44E-1
ESO154-G023	1.32±0.09E-1	1.41±0.11E-1	1.05±0.12E-1	3.76±0.51E-2	3.08±0.42E-2	1.59±0.20E-2	1.86±0.23E-2	5.00±0.54E-2	1.03±0.13E+0
NGC1291 ^{e f}	4.37±0.22E+0	4.56±0.23E+0	3.98±0.20E+0	2.11±0.28E+0	1.27±0.18E+0	9.47±1.22E-1	6.35±0.80E-1	4.81±0.52E-1	5.28±0.65E+0
NGC1313	9.81±0.51E-1	1.04±0.06E+0	7.41±0.44E-1	6.43±0.87E-1	4.87±0.67E-1	6.18±0.77E-1	1.22±0.15E+0	2.85±0.31E+0	5.23±0.64E+1
NGC1311	5.13±0.42E-2	5.25±0.57E-2	4.08±0.65E-2	2.37±0.32E-2	1.68±0.23E-2	1.27±0.17E-2	1.23±0.16E-2	2.90±0.31E-2	7.20±0.88E-1
UGC02716	2.53±0.29E-2	2.56±0.41E-2	2.22±0.47E-2	1.20±0.16E-2	7.58±1.04E-3	7.20±0.95E-3	8.67±1.09E-3	9.18±1.01E-3	1.64±0.21E-1
IC1959	3.45±0.32E-2	3.54±0.45E-2	2.77±0.52E-2	1.91±0.26E-2	1.31±0.18E-2	9.78±1.28E-3	1.00±0.13E-2	3.24±0.35E-2	8.99±1.10E-1
NGC1487	1.32±0.09E-1	1.78±0.12E-1	1.20±0.12E-1	7.07±0.96E-2	4.62±0.63E-2	6.97±0.89E-2	1.37±0.17E-1	2.96±0.32E-1	4.79±0.59E+0
NGC1510	3.77±0.28E-2	3.71±0.36E-2	3.09±0.40E-2	1.71±0.23E-2	1.19±0.16E-2	1.40±0.19E-2	2.20±0.28E-2	1.35±0.15E-1	9.22±1.13E-1
NGC1512 ^{e f}	8.12±0.44E-1	8.57±0.49E-1	7.30±0.47E-1	3.87±0.53E-1	2.43±0.34E-1	2.52±0.34E-1	4.34±0.55E-1	4.87±0.52E-1	6.83±0.83E+0
NGC1522	2.61±0.24E-2	2.28±0.32E-2	1.99±0.38E-2	1.10±0.15E-2	7.89±1.08E-3	9.79±1.29E-3	1.50±0.19E-2	9.66±1.04E-2	9.42±1.15E-1
IC2049	1.08±0.19E-2	1.26±0.29E-2	8.79±3.41E-3	4.38±0.60E-3	2.83±0.39E-3	1.09±0.16E-3	3.03±0.39E-3	4.69±0.53E-3	6.16±0.88E-2
ESO483-G013	3.93±0.35E-2	3.85±0.48E-2	3.37±0.55E-2	1.68±0.23E-2	1.14±0.16E-2	1.22±0.16E-2	1.12±0.14E-2	3.46±0.37E-2	5.40±0.66E-1
ESO158-G003	3.84±0.36E-2	3.54±0.49E-2	2.74±0.57E-2	1.64±0.22E-2	1.14±0.16E-2	1.11±0.14E-2	2.04±0.26E-2	2.91±0.31E-2	5.36±0.66E-1
ESO119-G016	1.89±0.28E-2	2.21±0.41E-2	1.51±0.49E-2	7.41±1.00E-3	5.38±0.74E-3	2.83±0.38E-3	2.90±0.38E-3	6.13±0.70E-3	7.33±1.11E-2
NGC1705 ^{e f}	5.75±0.37E-2	5.40±0.44E-2	4.44±0.48E-2	2.57±0.36E-2	1.79±0.25E-2	1.01±0.19E-2	1.68±0.20E-2	5.38±0.58E-2	1.25±0.15E+0
NGC1744	1.12±0.09E-1	1.13±0.13E-1	8.94±1.45E-2	9.86±1.33E-2	8.11±1.11E-2	4.51±0.57E-2	1.00±0.12E-1	1.11±0.12E-1	1.94±0.24E+0
NGC1796	1.02±0.06E-1	1.12±0.08E-1	9.55±0.84E-2	5.51±0.75E-2	3.76±0.52E-2	8.47±1.09E-2	1.91±0.24E-1	2.22±0.24E-1	3.40±0.41E+0
ESO486-G021	1.87±0.20E-2	2.07±0.28E-2	1.32±0.33E-2	6.57±0.89E-3	4.25±0.58E-3	4.94±0.66E-3	6.13±0.78E-3	1.30±0.14E-2	3.37±0.41E-1
MCG-05-13-004 ^b
NGC1800	8.96±0.55E-2	1.03±0.07E-1	8.34±0.71E-2	3.14±0.43E-2	2.08±0.29E-2	2.58±0.33E-2	3.57±0.45E-2	6.02±0.65E-2	1.21±0.15E+0
UGCA106	1.19±0.08E-1	6.95±0.78E-2	4.99±0.88E-2	2.69±0.37E-2	1.93±0.26E-2	1.75±0.22E-2	2.51±0.31E-2	5.05±0.55E-2	8.89±1.09E-1
LMC ^{a e f}	2.05±0.29E+3	1.41±0.20E+3	1.77±0.25E+3	4.81±0.75E+3	5.96±0.60E+3	1.11±0.13E+5
kkh037	5.43±1.59E-3	6.24±2.36E-3	6.43±2.81E-3	2.50±0.34E-3	1.58±0.22E-3	<1.11E-3	<1.22E-3	<4.05E-3	<5.44E-2
NGC2366 ^e	1.45±0.10E-1	1.47±0.13E-1	1.10±0.14E-1	6.47±0.88E-2	4.96±0.68E-2	4.83±0.61E-2	5.62±0.70E-2	6.84±0.74E-1	5.52±0.67E+0
UGCA133	1.79±0.31E-2	1.65±0.46E-2	9.06±4.67E-3	4.10±0.56E-3	3.11±0.43E-3	<2.20E-3	<2.40E-3	<7.99E-3	<1.08E-1
NGC2403 ^{e f}	2.94±0.15E+0	2.91±0.15E+0	2.39±0.12E+0	1.88±0.25E+0	1.31±0.18E+0	2.08±0.27E+0	4.11±0.51E+0	5.89±0.63E+0	8.57±1.05E+1
NGC2500 ^e	1.71±0.10E-1	1.80±0.11E-1	1.39±0.10E-1	8.77±1.19E-2	5.64±0.77E-2	1.13±0.15E-1	1.69±0.21E-1	2.09±0.23E-1	3.93±0.48E+0
NGC2537 ^e	1.93±0.10E-1	1.95±0.11E-1	1.60±0.10E-1	7.71±1.04E-2	5.11±0.70E-2	7.67±0.99E-2	1.41±0.18E-1	2.92±0.31E-1	4.07±0.50E+0
UGC04278 ^{e f}	4.79±0.36E-2	4.52±0.46E-2	3.58±0.51E-2	2.18±0.30E-2	1.57±0.22E-2	1.65±0.22E-2	1.56±0.20E-2	3.79±0.41E-2	8.96±1.10E-1
UGC04305 ^{e f}	1.66±0.12E-1	2.91±0.19E-1	2.16±0.19E-1	7.13±0.98E-2	5.66±0.78E-2	3.03±0.47E-2	2.38±0.48E-2	1.78±0.19E-1	3.19±0.39E+0
NGC2552	6.62±0.54E-2	8.70±0.77E-2	5.49±0.81E-2	3.35±0.45E-2	2.27±0.31E-2	2.16±0.28E-2	1.78±0.22E-2	5.77±0.62E-2	9.78±1.20E-1

Table 2—Continued

Galaxy	2MASS J 1.25 μm (Jy)	2MASS H 1.65 μm (Jy)	2MASS K _s 2.17 μm (Jy)	IRAC 3.6 μm (Jy)	IRAC 4.5 μm (Jy)	IRAC 5.8 μm (Jy)	IRAC 8.0 μm (Jy)	MIPS 24 μm (Jy)	MIPS 70 μm (Jy)
M81dwA ^{e f}	3.77±1.29E-3	3.88±1.95E-3	2.92±1.55E-3	1.86±0.90E-3	9.50±9.00E-4	<1.68E-3	<1.64E-3	3.45±0.41E-3	4.66±0.78E-2
UGC04426	1.15±0.29E-2	1.61±0.44E-2	8.91±3.97E-3	4.27±0.58E-3	3.10±0.43E-3	<2.10E-3	<2.30E-3	<7.65E-3	<1.03E-1
UGC04459 ^{e f}	7.54±2.07E-3	1.38±0.31E-2	7.93±3.71E-3	4.71±1.00E-3	3.88±1.00E-3	2.65±0.90E-3	7.32±1.00E-3	2.40±0.26E-2	3.16±0.39E-1
UGC04483 ^e	5.95±1.26E-3	7.63±1.89E-3	4.19±2.01E-3	1.84±0.25E-3	9.60±1.30E-4	6.40±1.00E-4	1.13±0.15E-3	7.05±0.77E-3	1.05±0.13E-1
NGC2683	2.16±0.11E+0	2.46±0.12E+0	2.10±0.11E+0	1.08±0.15E+0	6.92±0.95E-1	7.49±0.94E-1	1.18±0.15E+0	9.14±0.98E-1	1.65±0.20E+1
UGC04704	2.81±0.33E-2	1.84±0.46E-2	<1.29E-2	8.64±1.17E-3	5.63±0.77E-3	6.01±0.79E-3	1.13±0.18E-3	1.05±0.12E-2	1.35±0.18E-1
UGC04787	2.59±0.28E-2	2.40±0.39E-2	1.93±0.46E-2	8.55±1.16E-3	5.85±0.80E-3	2.94±0.40E-3	5.27±0.67E-3	8.67±0.96E-3	1.44±0.19E-1
UGC04998	2.55±0.32E-2	3.08±0.47E-2	1.77±0.54E-2	1.08±0.15E-2	7.51±1.03E-3	5.70±0.75E-3	6.58±0.83E-3	<7.72E-3	<1.04E-1
NGC2903	3.00±0.15E+0	3.14±0.16E+0	2.74±0.14E+0	1.61±0.22E+0	1.09±0.15E+0	2.20±0.28E+0	5.11±0.64E+0	7.00±0.75E+0	7.85±0.96E+1
UGC05076	1.62±0.26E-2	1.26±0.38E-2	9.06±4.55E-3	5.01±0.68E-3	3.28±0.45E-3	1.49±0.22E-3	4.57±0.58E-3	<6.68E-3	<9.01E-2
CGCG035-007	1.23±0.19E-2	1.41±0.28E-2	1.35±0.34E-2	4.28±0.58E-3	2.89±0.40E-3	1.85±0.25E-3	2.03±0.26E-3	4.43±0.50E-3	1.18±0.15E-1
UGC05139 ^{e f}	3.09±0.43E-2	3.97±0.64E-2	1.60±0.73E-2	1.19±0.14E-2	7.56±1.20E-3	7.32±1.80E-3	7.54±1.60E-3	6.56±0.78E-3	2.93±0.37E-1
IC0559	1.92±0.23E-2	1.72±0.33E-2	2.37±0.41E-2	8.10±1.10E-3	5.55±0.76E-3	5.23±0.69E-3	2.35±0.30E-3	5.08±0.58E-3	9.31±1.26E-2
F8D1	2.96±0.47E-2	7.01±0.75E-2	1.88±0.79E-2	1.08±0.15E-2	8.75±1.20E-3	<3.11E-3	<3.40E-3	<1.13E-2	<1.52E-1
[FM2000]1	<3.65E-3	<5.32E-3	<6.40E-3	<2.00E-4	<2.90E-4	<1.07E-3	<1.17E-3	<3.91E-3	<5.25E-2
NGC2976 ^{e f}	8.60±0.43E-1	8.93±0.46E-1	7.07±0.37E-1	4.34±0.59E-1	2.84±0.39E-1	5.04±0.65E-1	1.02±0.13E+0	1.40±0.15E+0	2.00±0.24E+1
LEDA166101	<7.92E-3	<1.14E-2	<1.35E-2	6.13±0.83E-3	4.10±0.56E-3	<2.22E-3	<2.43E-3	<8.08E-3	<1.08E-1
UGC05272	1.99±0.25E-2	2.57±0.36E-2	1.58±0.42E-2	7.35±1.00E-3	5.12±0.70E-3	3.76±0.50E-3	1.84±0.24E-3	1.31±0.14E-2	3.09±0.38E-1
UGC05288	2.91±0.29E-2	2.34±0.40E-2	2.44±0.47E-2	8.50±1.15E-3	5.69±0.78E-3	4.94±0.65E-3	3.14±0.40E-3	1.12±0.12E-2	1.78±0.23E-1
BK03N	<1.70E-3	<2.48E-3	<2.98E-3	<9.00E-5	<1.40E-4	<5.00E-4	<5.50E-4	<1.82E-3	<2.45E-2
NGC3031 ^{e f}	2.35±0.12E+1	2.55±0.13E+1	2.13±0.11E+1	1.09±0.15E+1	6.53±0.90E+0	5.88±0.75E+0	8.04±1.00E+0	5.24±0.56E+0	8.53±1.04E+1
NGC3034 ^{c e f}	9.29±0.46E+0	1.08±0.05E+1	1.01±0.05E+1	7.28±2.28E+0	5.75±1.81E+0	2.37±0.73E+1	6.22±1.92E+1	3.25±1.03E+2	1.63±0.51E+3
UGC05340 ^e	8.67±2.19E-3	7.35±3.28E-3	<9.36E-3	3.05±0.41E-3	1.97±0.27E-3	<1.60E-3	<1.74E-3	<5.81E-3	<7.83E-2
KDG061	9.81±2.78E-3	7.28±4.03E-3	1.18±0.49E-2	4.66±0.63E-3	2.89±0.40E-3	<1.95E-3	<2.13E-3	<7.08E-3	<9.53E-2
UGC05336	2.47±0.38E-2	2.05±0.55E-2	1.47±0.65E-2	7.38±1.10E-3	3.79±1.00E-3	<3.62E-3	<4.00E-3	4.02±0.48E-3	5.40±0.91E-2
ArpsLoop	<5.71E-3	<8.32E-3	<9.98E-3	<3.10E-4	<4.60E-4	<1.67E-3	<1.83E-3	<6.08E-3	<8.18E-2
UGC05364 ^f	<1.93E-2	<2.86E-2	<3.48E-2	1.95±0.26E-2	1.36±0.19E-2	<2.97E-3	<3.24E-3	<1.08E-2	<1.46E-1
UGC05373 ^f	1.22±0.08E-1	1.32±0.10E-1	1.36±0.11E-1	4.97±0.67E-2	3.61±0.50E-2	1.51±0.19E-2	1.55±0.19E-2	2.10±0.23E-2	1.21±0.19E-1
kkh057	<2.46E-3	<3.65E-3	<4.44E-3	5.90±0.80E-4	2.30±0.30E-4	<7.60E-4	<8.30E-4	<2.75E-3	<3.71E-2
UGCA193	1.58±0.25E-2	1.21±0.35E-2	1.91±0.43E-2	5.72±0.78E-3	3.82±0.53E-3	2.76±0.37E-3	2.36±0.31E-3	3.66±0.44E-3	4.04±0.76E-2
NGC3109	5.77±0.32E-1	3.56±0.26E-1	3.44±0.28E-1	3.02±0.41E-1	2.30±0.32E-1	1.44±0.18E-1	1.59±0.20E-1	3.01±0.32E-1	6.88±0.84E+0
NGC3077 ^f	1.05±0.05E+0	1.04±0.05E+0	8.70±0.46E-1	5.54±0.75E-1	3.75±0.51E-1	4.34±0.55E-1	8.11±1.01E-1	1.31±0.14E+0	1.96±0.24E+1
AM1001-270 ^f	<5.28E-3	<7.71E-3	<9.27E-3	3.26±0.44E-3	2.25±0.31E-3	<1.55E-3	<1.70E-3	<5.65E-3	<7.60E-2

Table 2—Continued

Galaxy	2MASS J 1.25 μm (Jy)	2MASS H 1.65 μm (Jy)	2MASS K _s 2.17 μm (Jy)	IRAC 3.6 μm (Jy)	IRAC 4.5 μm (Jy)	IRAC 5.8 μm (Jy)	IRAC 8.0 μm (Jy)	MIPS 24 μm (Jy)	MIPS 70 μm (Jy)	
BK05N	<5.90E-3	<8.66E-3	<1.04E-2	1.69±0.23E-3	7.90±1.10E-4	<1.76E-3	<1.92E-3	<6.40E-3	<8.61E-2	
UGC05428	1.41±0.33E-2	1.28±0.47E-2	1.03±0.51E-2	4.23±0.57E-3	2.64±0.36E-3	<2.22E-3	<2.43E-3	<8.06E-3	<1.08E-1	
UGC05423 ^{e f}	1.20±0.16E-2	1.37±0.23E-2	1.36±0.27E-2	4.86±1.00E-3	3.43±1.00E-3	2.65±0.90E-3	2.52±0.80E-3	3.34±0.39E-3	1.15±0.15E-1	1.0
UGC05442	1.51±0.27E-2	1.46±0.40E-2	1.33±0.48E-2	5.09±0.69E-3	3.55±0.49E-3	1.51±0.22E-3	3.12±0.40E-3	2.60±2.20E-4	<9.33E-2	
UGC05456	3.80±0.30E-2	5.01±0.43E-2	3.10±0.45E-2	1.33±0.18E-2	9.09±1.25E-3	8.98±1.18E-3	1.04±0.13E-2	5.68±0.61E-2	6.28±0.77E-1	6.3
IKN	<6.83E-3	<1.00E-2	<1.21E-2	<3.70E-4	<5.60E-4	<2.04E-3	<2.23E-3	<7.43E-3	<1.00E-1	
SextansA ^{e f}	1.42±0.09E-1	1.31±0.11E-1	6.22±1.13E-2	3.97±0.54E-2	2.71±0.37E-2	2.97±0.38E-2	2.51±0.31E-2	3.78±0.41E-2	7.32±0.91E-1	1.0
[HS98]117	5.42±2.72E-3	6.82±3.44E-3	9.03±4.20E-3	2.86±0.39E-3	1.57±0.22E-3	<2.02E-3	<2.21E-3	<7.33E-3	<9.84E-2	
NGC3239	1.60±0.09E-1	1.72±0.11E-1	1.25±0.11E-1	7.42±1.00E-2	4.97±0.68E-2	7.47±0.96E-2	8.72±1.09E-2	3.58±0.39E-1	5.00±0.61E+0	7.4
DDO078	<5.57E-3	<8.27E-3	<1.01E-2	<3.10E-4	<4.70E-4	<1.72E-3	<1.87E-3	<6.24E-3	<8.41E-2	
UGC05672	4.06±0.35E-2	3.45±0.46E-2	2.53±0.53E-2	1.19±0.16E-2	7.71±1.06E-3	7.17±0.94E-3	6.98±0.88E-3	8.51±0.95E-3	7.60±1.17E-2	4.0
UGC05666 ^{e f}	3.36±0.20E-1	2.31±0.20E-1	1.65±0.21E-1	1.51±0.21E-1	9.05±1.27E-2	6.44±0.87E-2	6.62±0.89E-2	2.82±0.30E-1	4.84±0.59E+0	1.0
UGC05692	9.28±0.63E-2	8.24±0.76E-2	6.64±0.84E-2	2.69±0.36E-2	1.77±0.24E-2	1.66±0.21E-2	1.13±0.14E-2	1.10±0.12E-2	2.95±0.38E-1	6.3
NGC3274	4.24±0.42E-2	4.15±0.59E-2	3.59±0.69E-2	2.17±0.29E-2	1.46±0.20E-2	1.86±0.24E-2	2.49±0.31E-2	6.53±0.70E-2	1.27±0.16E+0	1.5
BK06N	8.54±2.60E-3	<9.21E-3	<1.12E-2	2.07±0.28E-3	1.50±0.21E-3	<1.92E-3	<2.10E-3	<6.98E-3	<9.42E-2	
NGC3299	8.22±0.56E-2	7.11±0.68E-2	6.80±0.78E-2	2.99±0.40E-2	2.04±0.28E-2	1.83±0.24E-2	2.83±0.35E-2	2.47±0.27E-2	3.01±0.38E-1	1.0
UGC05764	6.61±1.88E-3	6.87±2.83E-3	7.29±3.41E-3	2.66±0.36E-3	1.90±0.26E-3	1.25±0.18E-3	1.02±0.14E-3	3.41±0.40E-3	6.03±0.87E-2	8.3
UGC05797	1.91±0.25E-2	1.48±0.35E-2	1.17±0.42E-2	6.48±0.88E-3	4.09±0.56E-3	3.74±0.50E-3	3.03±0.39E-3	4.31±0.50E-3	1.11±0.15E-1	2.3
UGC05829	5.48±0.52E-2	3.74±0.69E-2	2.22±0.81E-2	1.41±0.19E-2	9.56±1.31E-3	4.88±0.65E-3	4.42±0.57E-3	3.22±0.35E-2	7.35±0.90E-1	9.3
NGC3344 ^e	9.42±0.48E-1	8.91±0.46E-1	6.94±0.38E-1	4.01±0.54E-1	2.47±0.34E-1	4.59±0.58E-1	9.74±1.21E-1	1.19±0.13E+0	1.52±0.19E+1	4.9
NGC3351 ^{e f}	1.68±0.08E+0	1.77±0.09E+0	1.54±0.08E+0	8.13±1.10E-1	5.14±0.71E-1	7.20±0.93E-1	1.34±0.16E+0	2.53±0.27E+0	2.19±0.27E+1	5.6
NGC3368 ^e	2.29±0.11E+0	2.52±0.13E+0	2.11±0.11E+0	1.09±0.15E+0	6.65±0.91E-1	6.85±0.87E-1	8.86±1.10E-1	7.82±0.84E-1	1.45±0.18E+1	4.7
UGC05889	3.39±0.37E-2	3.91±0.53E-2	3.03±0.61E-2	1.34±0.18E-2	8.65±1.19E-3	6.38±0.84E-3	4.39±0.56E-3	7.99±0.90E-3	<1.17E-1	
UGC05923 ^e	2.63±0.18E-2	2.92±0.24E-2	2.18±0.25E-2	9.52±1.30E-3	6.40±0.88E-3	6.11±0.82E-3	9.45±1.20E-3	1.11±0.12E-2	2.62±0.32E-1	2.3
UGC05918	<4.88E-3	<7.27E-3	<8.87E-3	3.01±0.41E-3	2.00±0.28E-3	<1.52E-3	<1.66E-3	<5.52E-3	<7.44E-2	
NGC3432	2.03±0.11E-1	2.10±0.13E-1	1.71±0.12E-1	1.02±0.14E-1	7.38±1.01E-2	1.36±0.17E-1	2.29±0.29E-1	5.99±0.65E-1	9.83±1.20E+0	1.8
KDG073	<4.42E-3	<6.57E-3	<8.00E-3	1.94±0.26E-3	6.00±0.80E-4	<1.37E-3	<1.49E-3	<4.97E-3	<6.70E-2	
NGC3486 ^e	4.80±0.25E-1	5.82±0.31E-1	4.47±0.26E-1	2.36±0.32E-1	1.58±0.22E-1	2.60±0.33E-1	5.88±0.73E-1	6.41±0.69E-1	9.66±1.18E+0	2.7
NGC3510	5.82±0.45E-2	3.81±0.55E-2	2.32±0.63E-2	2.07±0.28E-2	1.45±0.20E-2	1.52±0.20E-2	2.31±0.29E-2	5.34±0.57E-2	1.18±0.14E+0	1.8
NGC3521 ^{e f}	3.74±0.19E+0	4.22±0.21E+0	3.50±0.18E+0	2.05±0.28E+0	1.36±0.19E+0	2.53±0.32E+0	6.27±0.76E+0	5.50±0.59E+0	6.45±0.79E+1	1.9
NGC3593 ^e	7.76±0.39E-1	9.45±0.48E-1	7.66±0.39E-1	3.76±0.51E-1	2.51±0.34E-1	5.26±0.67E-1	1.21±0.15E+0	1.69±0.18E+0	2.46±0.30E+1	3.3
NGC3623	2.89±0.14E+0	3.20±0.16E+0	2.65±0.13E+0	1.27±0.17E+0	7.95±1.09E-1	7.43±0.94E-1	7.67±0.96E-1	5.55±0.60E-1	7.02±0.86E+0	3.5
NGC3627 ^{e f}	3.34±0.17E+0	3.73±0.19E+0	3.17±0.16E+0	1.87±0.25E+0	1.25±0.17E+0	2.35±0.30E+0	5.58±0.69E+0	7.43±0.30E+0	9.22±0.70E+1	2.2

Table 2—Continued

Galaxy	2MASS J 1.25 μm (Jy)	2MASS H 1.65 μm (Jy)	2MASS K _s 2.17 μm (Jy)	IRAC 3.6 μm (Jy)	IRAC 4.5 μm (Jy)	IRAC 5.8 μm (Jy)	IRAC 8.0 μm (Jy)	MIPS 24 μm (Jy)	MIPS 70 μm (Jy)
NGC3628	2.43±0.12E+0	2.98±0.15E+0	2.66±0.14E+0	1.52±0.21E+0	1.04±0.14E+0	1.86±0.23E+0	4.08±0.51E+0	5.10±0.55E+0	6.86±0.84E+1
UGC06457	1.52±0.22E-2	1.65±0.33E-2	1.18±0.39E-2	5.52±0.75E-3	3.13±0.43E-3	2.94±0.39E-3	2.31±0.30E-3	2.07±0.29E-3	9.42±1.27E-2
UGC06541 ^e	1.13±0.18E-2	1.26±0.27E-2	1.26±0.32E-2	5.12±0.70E-3	3.76±0.52E-3	1.86±0.25E-3	2.17±0.28E-3	6.66±0.73E-3	1.83±0.23E-1
NGC3738 ^e	1.32±0.07E-1	1.40±0.09E-1	1.04±0.08E-1	6.03±0.82E-2	4.02±0.55E-2	4.23±0.55E-2	5.09±0.64E-2	1.24±0.13E-1	2.73±0.33E+0
NGC3741	1.13±0.25E-2	1.83±0.38E-2	1.12±0.45E-2	4.77±0.65E-3	3.24±0.45E-3	1.70±0.24E-3	1.02±0.15E-3	5.57±0.63E-3	1.73±0.22E-1
UGC06782	<4.93E-3	<7.31E-3	<8.88E-3	3.32±0.45E-3	2.30±0.32E-3	<1.51E-3	<1.65E-3	<5.49E-3	<7.40E-2
UGC06817	2.33±0.34E-2	2.62±0.51E-2	2.15±0.60E-2	8.27±1.12E-3	4.99±0.69E-3	4.12±0.55E-3	3.40±0.44E-3	7.04±0.81E-3	1.23±0.17E-1
UGC06900	2.38±0.31E-2	1.82±0.44E-2	1.81±0.52E-2	7.68±1.04E-3	5.41±0.74E-3	5.44±0.72E-3	4.26±0.54E-3	4.13±0.51E-3	<1.02E-1
NGC4020	6.58±0.43E-2	5.44±0.51E-2	5.91±0.60E-2	3.12±0.42E-2	2.03±0.28E-2	3.40±0.44E-2	6.82±0.86E-2	9.39±1.01E-2	1.25±0.15E+0
NGC4068	5.05±0.43E-2	4.16±0.57E-2	3.72±0.67E-2	2.42±0.33E-2	1.69±0.23E-2	1.20±0.16E-2	9.09±1.14E-3	3.22±0.35E-2	7.02±0.86E-1
NGC4080	5.25±0.35E-2	5.12±0.44E-2	3.45±0.46E-2	1.85±0.25E-2	1.21±0.17E-2	1.77±0.23E-2	3.94±0.50E-2	3.47±0.38E-2	4.34±0.53E-1
NGC4096	5.58±0.29E-1	6.22±0.32E-1	5.35±0.29E-1	2.91±0.39E-1	2.00±0.27E-1	3.91±0.50E-1	8.77±1.09E-1	8.74±0.94E-1	1.11±0.14E+1
NGC4144 ^e	1.60±0.09E-1	1.55±0.11E-1	1.24±0.11E-1	7.01±0.95E-2	4.81±0.66E-2	4.45±0.57E-2	6.14±0.77E-2	1.13±0.12E-1	2.37±0.29E+0
NGC4163	5.98±0.43E-2	4.39±0.51E-2	3.26±0.58E-2	1.73±0.23E-2	1.15±0.16E-2	7.26±0.95E-3	5.64±0.71E-3	1.24±0.14E-2	1.77±0.23E-1
NGC4190	5.96±0.43E-2	4.99±0.52E-2	3.69±0.59E-2	1.83±0.25E-2	1.20±0.16E-2	9.90±1.29E-3	5.85±0.74E-3	1.78±0.19E-2	5.65±0.99E-1
ESO321-G014	1.18±0.24E-2	9.34±3.48E-3	<9.72E-3	5.08±0.69E-3	3.52±0.48E-3	9.20±1.50E-4	1.17±0.17E-3	4.30±1.90E-4	<7.94E-2
UGC07242	<4.55E-3	<6.76E-3	<8.24E-3	<2.60E-4	<3.80E-4	<1.41E-3	<1.53E-3	<5.11E-3	<6.89E-2
UGCA276	1.24±0.26E-2	7.66±3.78E-3	4.49±2.06E-3	2.69±0.36E-3	1.53±0.21E-3	<1.84E-3	<2.01E-3	<6.69E-3	<9.02E-2
UGC07267	2.50±0.26E-2	1.98±0.35E-2	1.75±0.42E-2	7.27±0.99E-3	4.82±0.66E-3	2.65±0.36E-3	1.73±0.23E-3	3.53±0.43E-3	7.02±1.02E-2
NGC4214 ^e	5.86±0.31E-1	6.39±0.35E-1	4.88±0.30E-1	3.15±0.43E-1	2.18±0.30E-1	3.22±0.41E-1	5.46±0.68E-1	2.00±0.22E+0	2.28±0.28E+1
CGCG269-049 ^{e f}	4.91±1.33E-3	6.62±2.01E-3	3.31±1.99E-3	1.49±0.20E-3	1.16±0.16E-3	6.30±1.00E-4	6.20±0.90E-4	2.88±0.33E-3	4.63±0.65E-2
NGC4236 ^{e f}	6.35±0.34E-1	8.31±0.45E-1	5.70±0.35E-1	2.50±0.34E-1	2.10±0.29E-1	1.07±0.14E-1	2.16±0.27E-1	5.14±0.55E-1	8.02±0.98E+0
NGC4244 ^{e f}	6.73±0.35E-1	6.86±0.37E-1	5.78±0.33E-1	3.05±0.41E-1	2.10±0.29E-1	2.08±0.26E-1	2.87±0.36E-1	4.59±0.49E-1	7.44±0.91E+0
NGC4242 ^e	1.94±0.11E-1	2.40±0.15E-1	1.60±0.13E-1	1.03±0.14E-1	6.15±0.84E-2	6.34±0.81E-2	9.90±1.23E-2	1.07±0.12E-1	1.98±0.24E+0
UGC07321 ^{e f}	4.37±0.36E-2	4.75±0.49E-2	3.86±0.55E-2	2.28±0.31E-2	1.46±0.20E-2	1.71±0.22E-2	2.37±0.30E-2	2.98±0.32E-2	5.85±0.72E-1
NGC4248	8.41±0.54E-2	7.31±0.63E-2	6.94±0.71E-2	4.13±0.56E-2	2.50±0.34E-2	2.43±0.31E-2	3.09±0.39E-2	3.42±0.37E-2	4.95±0.61E-1
NGC4258 ^e	5.03±0.25E+0	5.50±0.28E+0	4.63±0.23E+0	2.28±0.31E+0	1.51±0.21E+0	1.17±0.15E+0	2.52±0.31E+0	2.78±0.30E+0	4.07±0.50E+1
ISZ399	3.54±0.26E-2	3.99±0.36E-2	3.45±0.39E-2	2.26±0.31E-2	1.60±0.22E-2	4.90±0.65E-2	1.22±0.15E-1	4.36±0.47E-1	3.05±0.37E+0
NGC4288	5.35±0.39E-2	6.46±0.54E-2	3.25±0.55E-2	2.40±0.33E-2	1.55±0.21E-2	2.29±0.30E-2	4.18±0.52E-2	6.79±0.73E-2	1.37±0.17E+0
UGC07408	4.48±0.40E-2	3.67±0.54E-2	3.29±0.64E-2	1.31±0.18E-2	7.75±1.06E-3	6.21±0.81E-3	4.98±0.63E-3	<9.06E-3	<1.22E-1
UGC07490	7.21±0.51E-2	8.07±0.69E-2	6.83±0.75E-2	2.48±0.34E-2	1.68±0.23E-2	1.57±0.20E-2	1.88±0.23E-2	2.25±0.24E-2	3.88±0.48E-1
NGC4395	4.68±0.28E-1	4.45±0.31E-1	3.20±0.31E-1	3.20±0.43E-1	2.54±0.35E-1	2.49±0.31E-1	2.59±0.32E-1	5.09±0.55E-1	1.06±0.13E+1
UGCA281 ^f	7.42±1.34E-3	8.22±2.00E-3	7.28±2.40E-3	3.64±0.50E-3	2.65±0.36E-3	1.79±0.24E-3	1.77±0.23E-3	5.89±0.63E-2	4.47±0.55E-1

Table 2—Continued

Galaxy	2MASS J 1.25 μm (Jy)	2MASS H 1.65 μm (Jy)	2MASS K _s 2.17 μm (Jy)	IRAC 3.6 μm (Jy)	IRAC 4.5 μm (Jy)	IRAC 5.8 μm (Jy)	IRAC 8.0 μm (Jy)	MIPS 24 μm (Jy)	MIPS 70 μm (Jy)	
UGC07559	1.50±0.30E-2	1.50±0.45E-2	1.12±0.54E-2	7.29±0.99E-3	4.40±0.61E-3	2.07±0.29E-3	2.01±0.27E-3	7.92±0.89E-3	1.82±0.23E-1	1.0
UGC07577	7.76±0.53E-2	7.78±0.67E-2	4.19±0.69E-2	2.41±0.33E-2	1.42±0.19E-2	7.38±0.96E-3	4.21±0.54E-3	6.05±0.72E-3	1.28±0.18E-1	4.0
NGC4449 ^e	1.03±0.05E+0	1.11±0.06E+0	8.93±0.46E-1	4.81±0.65E-1	3.14±0.43E-1	6.32±0.80E-1	1.35±0.17E+0	3.21±0.35E+0	4.72±0.58E+1	8.4
UGC07599	6.60±1.56E-3	9.16±2.35E-3	4.01±2.06E-3	2.74±0.37E-3	1.43±0.20E-3	<1.13E-3	<1.23E-3	<4.11E-3	<5.55E-2	
UGC07605	1.39±0.19E-2	1.11±0.28E-2	6.09±2.45E-3	4.31±0.59E-3	2.41±0.33E-3	<1.34E-3	<1.46E-3	1.63±0.23E-3	5.79±0.84E-2	
NGC4455	5.22±0.34E-2	5.47±0.43E-2	4.28±0.45E-2	2.17±0.30E-2	1.46±0.20E-2	1.36±0.18E-2	1.62±0.20E-2	3.41±0.37E-2	9.52±1.16E-1	1.9
UGC07608	2.12±0.36E-2	1.55±0.52E-2	1.49±0.63E-2	6.86±0.93E-3	4.07±0.56E-3	3.27±0.44E-3	7.54±0.95E-3	2.41±0.26E-2	3.05±0.38E-1	3.0
NGC4460 ^e	1.92±0.10E-1	2.03±0.12E-1	1.95±0.12E-1	8.35±1.13E-2	5.62±0.77E-2	7.77±1.00E-2	1.24±0.16E-1	3.05±0.33E-1	3.83±0.47E+0	5.4
UGC07639	2.54±0.32E-2	2.67±0.46E-2	2.64±0.55E-2	1.14±0.15E-2	7.68±1.05E-3	4.56±0.60E-3	3.27±0.42E-3	5.63±0.66E-3	1.15±0.16E-1	1.0
NGC4485 ^e	9.47±0.54E-2	9.93±0.63E-2	6.95±0.58E-2	4.25±0.58E-2	2.97±0.41E-2	5.72±0.75E-2	9.46±1.19E-2	1.87±0.20E-1	3.11±0.38E+0	9.6
NGC4490 ^e	9.34±0.47E-1	9.35±0.47E-1	8.14±0.42E-1	4.71±0.64E-1	3.23±0.44E-1	7.92±1.01E-1	1.69±0.21E+0	4.29±0.46E+0	6.80±0.83E+1	1.0
UGC07690	4.76±0.37E-2	5.26±0.50E-2	2.77±0.53E-2	1.86±0.25E-2	1.26±0.17E-2	1.09±0.14E-2	1.18±0.15E-2	3.01±0.33E-2	7.88±0.96E-1	1.1
UGC07699	5.39±0.39E-2	7.75±0.57E-2	5.35±0.57E-2	2.24±0.30E-2	1.43±0.20E-2	1.50±0.19E-2	2.00±0.25E-2	3.75±0.41E-2	7.20±0.88E-1	1.5
UGC07698	3.14±0.41E-2	3.11±0.59E-2	2.54±0.70E-2	1.22±0.17E-2	1.06±0.15E-2	1.60±0.21E-2	1.87±0.23E-2	1.47±0.16E-2	2.63±0.33E-1	4.0
UGC07719	1.02±0.20E-2	1.76±0.30E-2	8.71±3.52E-3	4.66±0.63E-3	3.10±0.43E-3	1.71±0.24E-3	1.22±0.17E-3	1.34±0.14E-2	2.20±0.27E-1	1.0
UGC07774	2.03±0.20E-2	2.81±0.30E-2	1.48±0.33E-2	9.08±1.23E-3	5.52±0.76E-3	3.97±0.53E-3	5.24±0.67E-3	9.34±1.02E-3	1.44±0.18E-1	3.0
UGCA292 ^{e f}	<3.62E-3	<5.39E-3	<6.57E-3	1.40±0.19E-3	5.30±0.70E-4	<1.12E-3	2.76±0.35E-3	2.19±0.26E-3	4.64±0.67E-2	
NGC4594 ^{e f}	8.07±0.40E+0	9.20±0.46E+0	7.56±0.38E+0	3.94±0.53E+0	2.31±0.32E+0	1.73±0.22E+0	1.30±0.16E+0	7.74±0.83E-1	7.31±0.89E+0	4.0
NGC4605	6.49±0.33E-1	6.92±0.36E-1	5.61±0.31E-1	3.25±0.44E-1	2.27±0.31E-1	3.88±0.49E-1	7.36±0.92E-1	1.05±0.11E+0	2.16±0.26E+1	3.7
NGC4618 ^e	2.81±0.15E-1	3.26±0.18E-1	2.44±0.15E-1	1.58±0.21E-1	1.04±0.14E-1	1.72±0.22E-1	3.27±0.41E-1	4.01±0.43E-1	7.89±0.96E+0	1.7
NGC4625 ^{e f}	9.82±0.64E-2	1.13±0.08E-1	8.98±0.88E-2	4.85±0.64E-2	3.01±0.40E-2	5.74±0.76E-2	1.28±0.16E-1	1.29±0.14E-1	1.85±0.23E+0	5.0
NGC4631 ^{e f}	1.75±0.09E+0	1.98±0.10E+0	1.84±0.09E+0	1.26±0.17E+0	8.36±1.15E-1	2.45±0.31E+0	5.86±0.73E+0	8.14±0.88E+0	1.38±0.17E+2	2.6
UGC07866	2.26±0.32E-2	2.87±0.48E-2	3.16±0.57E-2	1.01±0.14E-2	5.86±0.80E-3	2.48±0.34E-3	3.61±0.46E-3	6.61±0.76E-3	2.54±0.32E-1	2.0
NGC4656	2.01±0.12E-1	1.90±0.14E-1	1.35±0.14E-1	9.54±1.29E-2	7.05±0.97E-2	7.65±0.97E-2	1.02±0.13E-1	5.41±0.58E-1	9.28±1.13E+0	1.2
UGC07916	<9.70E-3	<1.44E-2	<1.76E-2	4.10±0.56E-3	3.24±0.44E-3	2.24±0.31E-3	1.90±0.25E-3	9.11±1.00E-3	1.22±0.16E-1	1.0
UGC07950	3.63±0.28E-2	4.17±0.39E-2	3.19±0.43E-2	1.07±0.14E-2	7.41±1.02E-3	7.17±0.94E-3	4.33±0.55E-3	1.15±0.13E-2	3.03±0.37E-1	4.0
UGC07949	9.22±2.14E-3	1.05±0.32E-2	6.88±3.42E-3	3.51±0.48E-3	<8.50E-4	<1.55E-3	<1.70E-3	2.20±0.30E-3	<7.63E-2	
NGC4707	2.39±0.33E-2	2.30±0.49E-2	1.62±0.58E-2	1.09±0.15E-2	6.26±0.86E-3	5.10±0.67E-3	4.30±0.55E-3	1.12±0.12E-2	2.28±0.29E-1	4.0
NGC4736 ^{e f}	6.95±0.35E+0	7.68±0.38E+0	6.44±0.32E+0	3.60±0.49E+0	2.32±0.32E+0	2.72±0.35E+0	5.17±0.64E+0	5.53±0.60E+0	1.01±0.12E+2	1.6
UGC08024 ^{e f}	9.92±2.62E-3	1.24±0.40E-2	1.20±0.48E-2	4.07±1.00E-3	2.99±1.00E-3	<4.03E-3	<3.99E-3	<4.38E-3	<5.91E-2	
NGC4826 ^{e f}	5.68±0.28E+0	6.31±0.32E+0	5.28±0.26E+0	2.52±0.34E+0	1.57±0.22E+0	1.64±0.21E+0	2.35±0.29E+0	2.55±0.28E+0	5.29±0.65E+1	8.5
UGC08091 ^f	8.86±1.81E-3	1.21±0.27E-2	8.40±3.24E-3	3.05±0.42E-3	2.29±0.31E-3	1.55±0.22E-3	1.47±0.20E-3	4.32±0.49E-3	8.17±1.09E-2	1.0
UGCA319	1.22±0.20E-2	1.39±0.28E-2	1.28±0.34E-2	5.50±0.75E-3	3.51±0.48E-3	2.50±0.34E-3	5.16±0.66E-3	<4.77E-3	<6.42E-2	

Table 2—Continued

Galaxy	2MASS J 1.25 μm (Jy)	2MASS H 1.65 μm (Jy)	2MASS K _s 2.17 μm (Jy)	IRAC 3.6 μm (Jy)	IRAC 4.5 μm (Jy)	IRAC 5.8 μm (Jy)	IRAC 8.0 μm (Jy)	MIPS 24 μm (Jy)	MIPS 70 μm (Jy)
UGCA320	3.51±0.52E-2	4.67±0.76E-2	<2.06E-2	1.80±0.24E-2	1.45±0.20E-2	3.23±0.42E-3	3.42±0.43E-3	2.33±0.25E-2	5.18±0.64E-1
UGC08188	1.18±0.08E-1	1.70±0.12E-1	1.22±0.12E-1	5.96±0.81E-2	4.47±0.61E-2	4.11±0.52E-2	3.56±0.44E-2	6.88±0.74E-2	1.52±0.19E+0
UGC08201 ^{e f}	3.20±0.37E-2	4.69±0.55E-2	3.73±0.63E-2	1.56±0.23E-2	1.18±0.15E-2	5.35±1.70E-3	4.08±0.80E-3	4.49±0.56E-3	1.41±0.19E-1
MCG-03-34-002	1.72±0.19E-2	1.78±0.27E-2	2.22±0.33E-2	7.23±0.98E-3	5.10±0.70E-3	4.02±0.54E-3	2.90±0.37E-3	6.75±0.74E-3	1.15±0.15E-1
UGC08245	2.57±0.26E-2	2.44±0.36E-2	2.00±0.43E-2	9.42±1.28E-3	5.98±0.82E-3	2.64±0.36E-3	2.90±0.37E-3	4.12±0.49E-3	9.63±1.32E-2
NGC5023 ^e	9.86±0.62E-2	1.04±0.08E-1	8.98±0.82E-2	4.50±0.61E-2	2.87±0.39E-2	2.48±0.32E-2	1.99±0.25E-2	5.68±0.61E-2	9.50±1.16E-1
CGCG217-018	1.60±0.18E-2	2.13±0.27E-2	1.62±0.31E-2	6.64±0.90E-3	4.24±0.58E-3	3.90±0.52E-3	4.71±0.60E-3	1.19±0.13E-2	1.70±0.21E-1
UGC08313	1.81±0.26E-2	2.88±0.39E-2	2.41±0.46E-2	9.26±1.26E-3	5.89±0.81E-3	5.70±0.75E-3	7.12±0.90E-3	2.78±0.30E-2	2.37±0.29E-1
UGC08320	5.83±0.49E-2	6.20±0.67E-2	5.02±0.76E-2	1.98±0.27E-2	1.47±0.20E-2	5.34±0.70E-3	7.09±0.90E-3	1.69±0.19E-2	5.62±0.69E-1
UGC08331	2.18±0.29E-2	2.33±0.42E-2	1.58±0.50E-2	6.45±0.87E-3	4.49±0.62E-3	2.25±0.31E-3	2.24±0.30E-3	7.04±0.79E-3	1.63±0.21E-1
NGC5055 ^{e f}	4.21±0.21E+0	4.96±0.25E+0	4.05±0.20E+0	2.38±0.32E+0	1.55±0.21E+0	2.62±0.34E+0	5.64±0.70E+0	5.54±0.60E+0	7.44±0.91E+1
NGC5068	8.64±0.44E-1	8.12±0.44E-1	7.10±0.40E-1	4.59±0.62E-1	3.26±0.45E-1	4.87±0.61E-1	1.24±0.15E+0	1.37±0.15E+0	2.08±0.25E+1
IC4247	1.85±0.19E-2	1.57±0.27E-2	1.39±0.31E-2	6.36±0.86E-3	4.33±0.60E-3	2.07±0.28E-3	1.86±0.24E-3	4.20±0.47E-3	6.94±0.94E-2
NGC5204 ^e	1.43±0.08E-1	1.48±0.10E-1	1.12±0.10E-1	6.80±0.92E-2	4.60±0.63E-2	5.05±0.65E-2	8.22±1.03E-2	1.78±0.19E-1	4.02±0.40E+0
NGC5194 ^{e f}	4.99±0.25E+0	5.89±0.30E+0	4.52±0.23E+0	2.66±0.36E+0	1.80±0.26E+0	4.23±0.54E+0	1.06±0.13E+1	1.24±0.13E+1	1.56±0.19E+2
NGC5195 ^{e f}	2.37±0.12E+0	2.80±0.14E+0	2.25±0.11E+0	8.34±1.13E-1	5.11±0.70E-1	4.62±0.61E-1	6.46±0.81E-1	1.47±0.16E+0	9.72±1.19E+0
UGC08508	2.18±0.25E-2	2.13±0.36E-2	1.39±0.42E-2	8.43±1.14E-3	5.10±0.70E-3	3.90±0.52E-3	4.28±0.54E-3	6.25±0.70E-3	1.47±0.19E-1
NGC5229	3.60±0.33E-2	4.76±0.48E-2	4.23±0.55E-2	1.31±0.18E-2	8.57±1.18E-3	7.40±0.97E-3	8.06±1.02E-3	1.66±0.18E-2	3.56±0.44E-1
NGC5238	4.44±0.38E-2	5.07±0.53E-2	3.47±0.59E-2	1.23±0.17E-2	8.72±1.20E-3	8.26±1.08E-3	5.30±0.67E-3	1.63±0.18E-2	4.02±0.50E-1
[KK98]208	<9.31E-3	<1.37E-2	<1.66E-2	<5.10E-4	<7.70E-4	<2.82E-3	<3.08E-3	<1.03E-2	<1.38E-1
NGC5236 ^f	1.13±0.06E+1	1.26±0.06E+1	1.04±0.05E+1	6.23±0.84E+0	4.11±0.56E+0	9.49±1.18E+0	2.41±0.30E+1	3.96±0.43E+1	3.82±0.47E+2
ESO444-G084	<6.46E-3	<9.45E-3	<1.14E-2	3.38±0.46E-3	2.13±0.29E-3	2.03±0.28E-3	7.40±1.10E-4	2.54±0.31E-3	6.29±0.88E-2
UGC08638	1.32±0.26E-2	2.29±0.39E-2	1.52±0.46E-2	7.48±1.01E-3	5.01±0.69E-3	2.74±0.37E-3	2.24±0.29E-3	8.99±0.99E-3	1.41±0.18E-1
UGC08651	2.09±0.29E-2	1.59±0.41E-2	1.59±0.50E-2	5.93±0.80E-3	3.90±0.54E-3	1.79±0.24E-3	1.35±0.18E-3	3.41±0.40E-3	7.49±1.14E-2
NGC5253 ^e	4.40±0.22E-1	4.44±0.23E-1	3.54±0.19E-1	2.42±0.33E-1	2.62±0.36E-1	5.38±0.69E-1	8.07±1.01E-1
NGC5264	1.50±0.09E-1	1.15±0.08E-1	1.08±0.09E-1	5.31±0.72E-2	3.68±0.50E-2	3.60±0.46E-2	4.22±0.53E-2	4.86±0.52E-2	7.78±0.95E-1
UGC08760	1.48±0.26E-2	1.29±0.39E-2	1.59±0.47E-2	6.09±0.83E-3	4.35±0.60E-3	2.08±0.28E-3	1.35±0.18E-3	1.19±0.14E-3	<9.26E-2
kkh086	<4.11E-3	<6.10E-3	<7.41E-3	1.28±0.17E-3	7.20±1.00E-4	<1.26E-3	<1.38E-3	<4.59E-3	<6.18E-2
UGC08837	3.44±0.41E-2	2.27±0.58E-2	2.65±0.71E-2	1.56±0.21E-2	1.01±0.14E-2	7.20±0.94E-3	1.07±0.13E-2	1.90±0.21E-2	2.86±0.36E-1
UGC08833	1.20±0.20E-2	6.30±2.94E-3	3.43±1.67E-3	2.45±0.33E-3	2.05±0.28E-3	<1.43E-3	<1.57E-3	<5.22E-3	<7.04E-2
NGC5457 ^{e f}	4.38±0.22E+0	5.04±0.26E+0	4.41±0.23E+0	2.70±0.37E+0	1.90±0.26E+0	4.49±0.56E+0	7.63±0.95E+0	1.06±0.11E+1	1.18±0.14E+2
NGC5474 ^{e f}	1.43±0.10E-1	1.59±0.13E-1	1.14±0.13E-1	1.04±0.14E-1	7.34±1.02E-2	7.55±1.01E-2	1.17±0.15E-1	1.57±0.17E-1	3.47±0.42E+0
NGC5477 ^f	2.39±0.26E-2	2.47±0.38E-2	2.20±0.45E-2	7.42±1.01E-3	5.17±0.71E-3	4.19±0.55E-3	2.60±0.34E-3	1.72±0.19E-2	4.24±0.52E-1

Table 2—Continued

Galaxy	2MASS J 1.25 μm (Jy)	2MASS H 1.65 μm (Jy)	2MASS K _s 2.17 μm (Jy)	IRAC 3.6 μm (Jy)	IRAC 4.5 μm (Jy)	IRAC 5.8 μm (Jy)	IRAC 8.0 μm (Jy)	MIPS 24 μm (Jy)	MIPS 70 μm (Jy)	
[KK98]230	<2.25E-3	<3.35E-3	<4.08E-3	4.60±0.60E-4	3.40±0.50E-4	<7.00E-4	<7.60E-4	<2.53E-3	<3.42E-2	
UGC09128 ^e	1.30±0.19E-2	9.19±2.66E-3	9.25±3.19E-3	3.11±0.42E-3	2.39±0.33E-3	<1.28E-3	<1.40E-3	<4.65E-3	<6.27E-2	
NGC5585 ^e	1.45±0.09E-1	1.57±0.11E-1	1.12±0.11E-1	8.69±1.18E-2	5.87±0.81E-2	6.56±0.84E-2	8.88±1.11E-2	1.38±0.15E-1	3.00±0.37E+0	7.46
UGC09240	4.80±0.41E-2	4.17±0.54E-2	3.32±0.62E-2	1.55±0.21E-2	1.07±0.15E-2	7.96±1.04E-3	7.79±0.98E-3	2.32±0.25E-2	3.60±0.45E-1	4.9
UGC09405	1.51±0.28E-2	2.01±0.42E-2	1.29±0.50E-2	6.69±0.91E-3	3.97±0.55E-3	2.75±0.37E-3	3.76±0.48E-3	4.62±0.55E-3	5.57±0.96E-2	1.6
MRK475	2.26±1.13E-3	2.00±1.21E-3	1.42±0.73E-3	9.80±1.30E-4	8.00±1.10E-4	5.40±0.90E-4	8.20±1.10E-4	9.27±1.00E-3	1.10±0.14E-1	4.1
NGC5832	1.07±0.07E-1	1.09±0.08E-1	9.68±0.84E-2	4.50±0.61E-2	2.92±0.40E-2	2.98±0.38E-2	4.59±0.57E-2	4.38±0.47E-2	8.13±1.00E-1	2.68
NGC5949	1.39±0.07E-1	1.47±0.09E-1	1.21±0.08E-1	7.01±0.95E-2	4.48±0.62E-2	7.55±0.98E-2	1.50±0.19E-1	1.44±0.16E-1	2.18±0.27E+0	6.11
UGC09992	1.14±0.22E-2	9.90±3.30E-3	9.72±3.96E-3	4.80±0.65E-3	3.24±0.45E-3	1.51±0.21E-3	3.78±0.48E-3	6.81±0.76E-3	1.16±0.15E-1	1.3
KKR25 ^{e f}	<3.51E-3	<5.24E-3	<6.39E-3	<2.00E-4	<3.00E-4	<1.09E-3	<1.19E-3	<3.97E-3	<5.36E-2	
NGC6503 ^e	9.49±0.48E-1	1.05±0.05E+0	8.60±0.45E-1	4.47±0.60E-1	2.99±0.41E-1	5.05±0.64E-1	9.27±1.16E-1	8.73±0.94E-1	1.51±0.18E+1	3.72
IC4951	3.47±0.30E-2	3.60±0.40E-2	3.44±0.47E-2	1.02±0.14E-2	7.20±0.99E-3	5.74±0.76E-3	3.58±0.46E-3	1.14±0.12E-2	2.35±0.29E-1	3.0
DDO210 ^f	<4.48E-3	<6.59E-3	<7.97E-3	2.99±0.41E-3	1.85±0.25E-3	<1.35E-3	<1.47E-3	<4.90E-3	<6.60E-2	
IC5052 ^e	2.38±0.13E-1	2.47±0.14E-1	2.01±0.13E-1	1.24±0.17E-1	8.65±1.19E-2	9.01±1.16E-2	1.39±0.17E-1	3.82±0.41E-1	4.58±0.56E+0	8.52
NGC7064	6.58±0.40E-2	4.87±0.43E-2	4.41±0.48E-2	2.37±0.32E-2	1.54±0.21E-2	1.12±0.15E-2	1.19±0.15E-2	3.24±0.35E-2	1.01±0.12E+0	1.33
NGC7090 ^e	4.34±0.22E-1	4.83±0.25E-1	3.92±0.22E-1	2.18±0.30E-1	1.44±0.20E-1	2.49±0.32E-1	4.87±0.61E-1	6.53±0.70E-1	1.06±0.13E+1	2.84
IC5152 ^{d e}	4.60±0.23E-1	3.37±0.18E-1	3.06±0.18E-1	...	1.66±0.23E-1	...	2.27±0.28E-1	2.09±0.23E-1	4.86±0.59E+0	1.13
IC5256	2.85±0.21E-2	2.58±0.27E-2	2.10±0.31E-2	8.08±1.10E-3	5.38±0.74E-3	8.85±1.17E-3	1.75±0.22E-2	1.88±0.20E-2	2.79±0.34E-1	6.0
UGCA438	2.18±0.31E-2	2.27±0.45E-2	1.68±0.53E-2	9.02±1.22E-3	6.35±0.87E-3	3.85±0.51E-3	4.23±0.53E-3	<7.74E-3	<1.04E-1	
ESO347-G017	1.86±0.28E-2	2.00±0.42E-2	1.59±0.50E-2	8.80±1.19E-3	5.67±0.78E-3	3.21±0.43E-3	2.94±0.38E-3	8.56±0.95E-3	2.77±0.35E-1	2.9
UGC12613 ^f	1.22±0.09E-1	9.81±1.02E-2	1.14±0.12E-1	5.55±0.75E-2	3.31±0.45E-2	1.84±0.24E-2	2.63±0.33E-2	2.56±0.28E-2	3.52±0.45E-1	1.21
IC5332	4.14±0.23E-1	5.73±0.32E-1	3.86±0.27E-1	2.38±0.32E-1	1.64±0.23E-1	1.85±0.23E-1	2.93±0.37E-1	3.34±0.36E-1	4.61±0.56E+0	1.98
NGC7713	1.79±0.10E-1	2.24±0.13E-1	1.51±0.12E-1	1.00±0.14E-1	6.85±0.94E-2	8.53±1.09E-2	1.40±0.17E-1	2.84±0.31E-1	5.70±0.70E+0	1.08
UGCA442	2.32±0.30E-2	2.37±0.43E-2	1.34±0.51E-2	1.12±0.15E-2	7.51±1.03E-3	3.81±0.51E-3	2.63±0.34E-3	1.01±0.11E-2	1.21±0.16E-1	2.6
kkh098	1.02±0.18E-2	1.07±0.26E-2	7.56±3.09E-3	2.42±0.33E-3	1.56±0.22E-3	<1.21E-3	<1.32E-3	<4.39E-3	<5.90E-2	
ESO149-G003	1.03±0.26E-2	1.27±0.40E-2	<1.12E-2	3.55±0.48E-3	2.58±0.36E-3	6.90±1.00E-4	8.40±1.10E-4	8.90±1.60E-4	5.74±0.84E-2	
NGC7793 ^{e f}	1.68±0.08E+0	1.70±0.09E+0	1.31±0.07E+0	7.71±1.04E-1	4.69±0.64E-1	1.02±0.13E+0	1.85±0.23E+0	2.10±0.23E+0	3.29±0.40E+1	1.07

Note. — The compact table entry format T.UV±W.XYEZ implies (T.UV±W.XY)×10^Z. See § 4 for corrections that have been applied to the data. The uncertainty includes both statistical and systematic effects ($\lesssim 10\%$ for the near-infrared data). 5 σ upper limits are provided for non-detections.

^aInfrared photometry for the Large and Small Magellanic Clouds are from Bernard et al. (2008) and Gordon et al. (2009), respectively.

^bNGC 1800 and MCG-05-13-004 spatially overlap so separate photometry for MCG-05-13-004 is not provided.

^cThe bright cores of NGC 3034 (M82) and NGC 0253 produce particularly challenging *Spitzer* data, including the effects of saturation at 24 μm . The 24 μm flux densities are approximated from *IRAS* data via $\nu f_\nu(24\mu\text{m}) = \nu f_\nu(25\mu\text{m})$, and the data at other wavelengths should be used with caution.

^dOnly 4.5 and 8.0 μm data were obtained for IC 5152.

^eIRAC imaging taken from the *Spitzer* archives.

^fMIPS imaging taken from the *Spitzer* archives.

Table 3. IRAC Aperture Correction Parameters

λ	A	B	C
3.6 μm	0.82	0.370	0.910
4.5 μm	1.16	0.443	0.940
5.8 μm	1.49	0.207	0.710
8.0 μm	1.37	0.330	0.740

Note. — See Equation 2 and
<http://ssc.spitzer.caltech.edu/irac/calib/extcal/>

Table 4. LVL Infrared Ratios and Dispersions

Ratio	Median	Dispersion (dex)
$f_{\nu}(70\mu\text{m})/f_{\nu}(160\mu\text{m})$	0.53	0.21
$f_{\nu}(8.0\mu\text{m})/f_{\nu}(24\mu\text{m})$	0.53	0.27
$\nu f_{\nu}(8.0\mu\text{m})/TIR$	0.12	0.23
$\nu f_{\nu}(8.0\mu\text{m})_{\text{dust}}/TIR$	0.083	0.40
$\nu f_{\nu}(24\mu\text{m})/TIR$	0.074	0.16
$\nu f_{\nu}(70\mu\text{m})/TIR$	0.47	0.11
$\nu f_{\nu}(160\mu\text{m})/TIR$	0.39	0.12

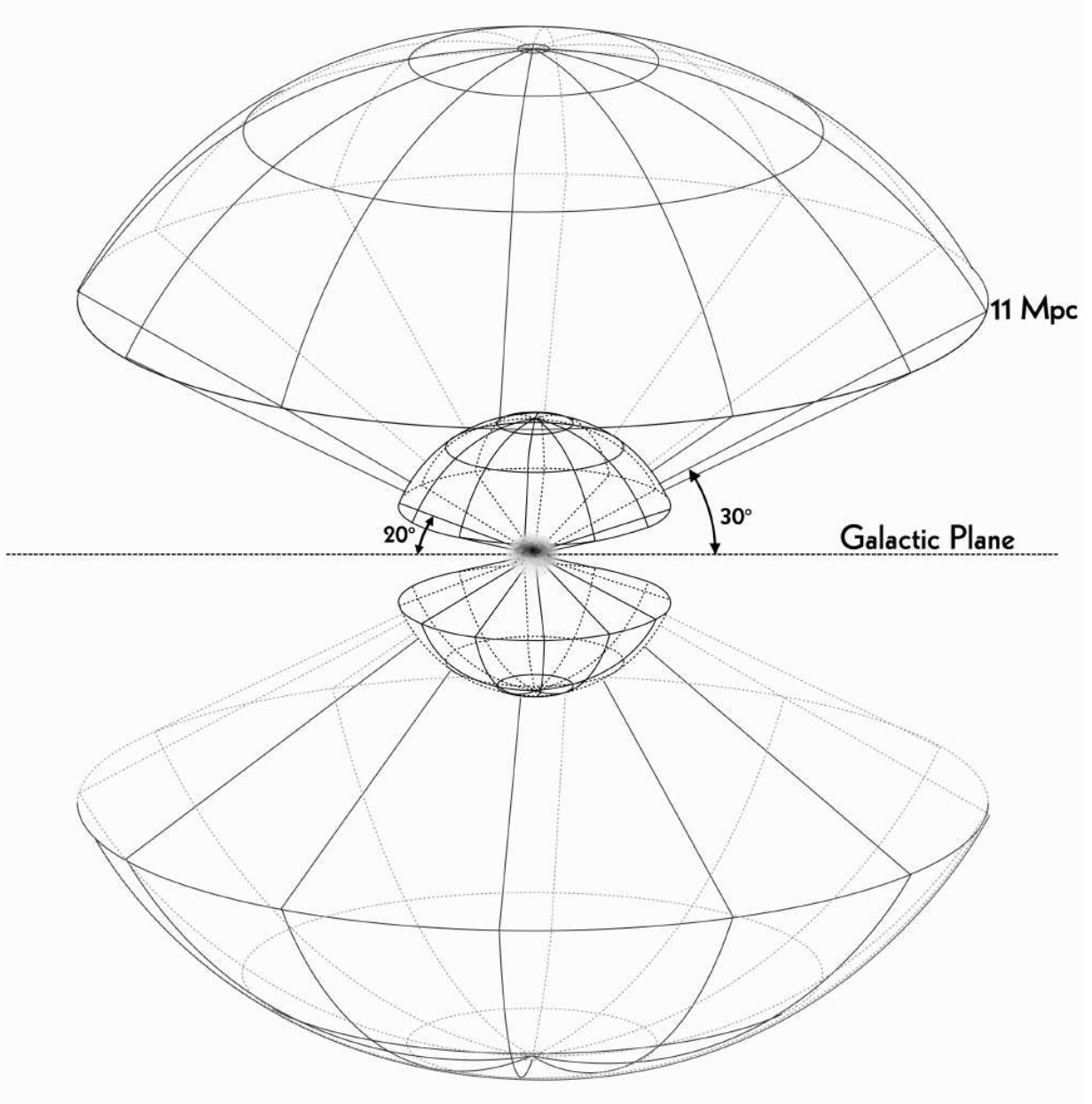


Fig. 1.— Schematic representation of the tiered volume coverage for the Local Volume Legacy survey. The 258 galaxies in the LVL sample include *i*) 69 early- and late-type galaxies primarily within the inner 3.5 Mpc for which *HST* observations exist from the ANGST program, and *ii*) a magnitude-limited sample of spiral and irregular galaxies from 11HUGS out to 11 Mpc. The *Spitzer* infrared imaging data that are being collected by LVL complement the ground-based $H\alpha$ and *GALEX* ultraviolet imaging already available for the sample. Image credit: Pete Marenfeld (NOAO/AURA/NSF).

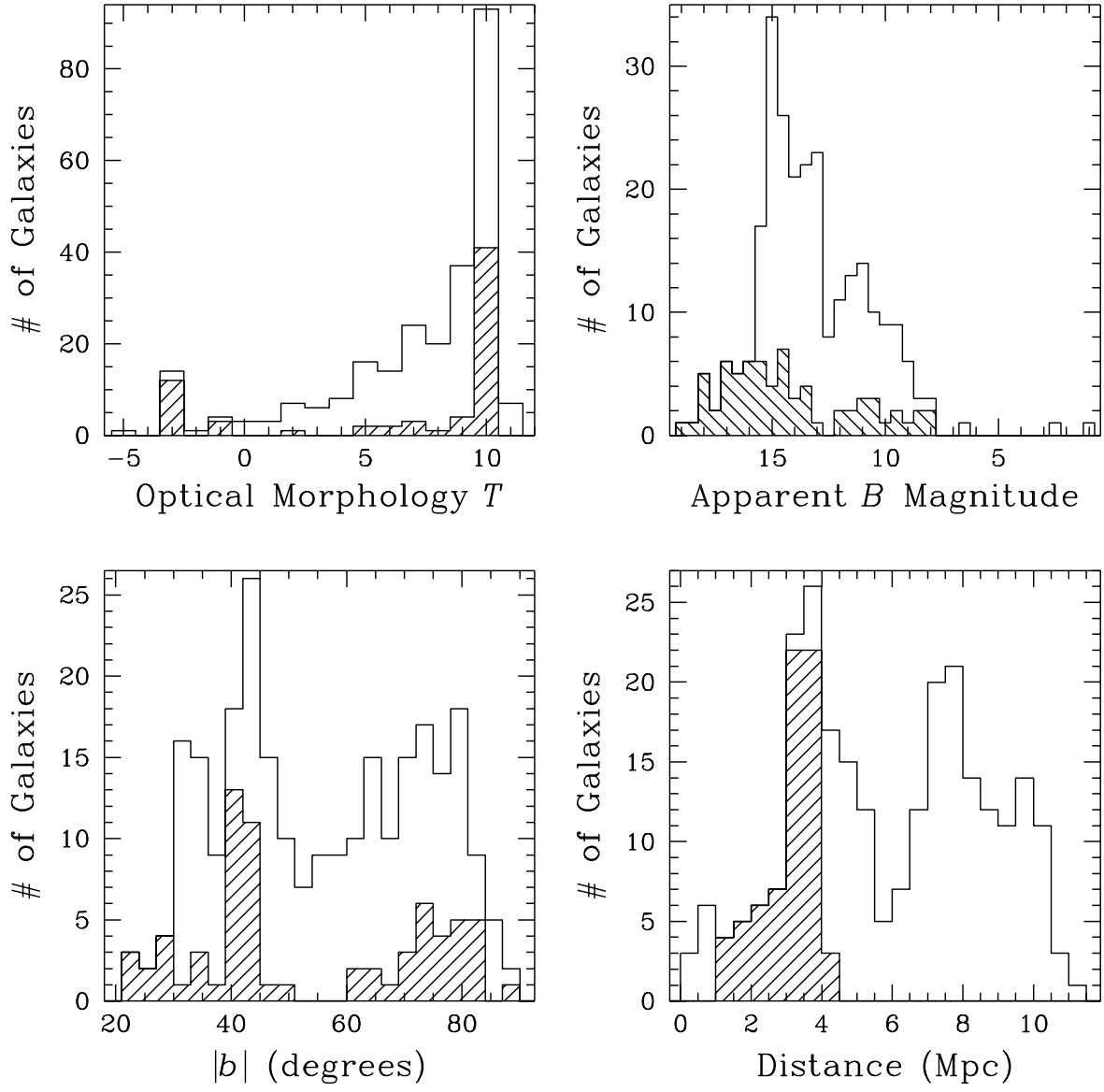


Fig. 2.— The distributions of RC3 morphological type (top left), apparent B magnitude (top right), Galactic latitude (bottom left) and distance (bottom right) for the LVL sample. The histograms outlined by the solid lines show the entire sample of 258 galaxies, whereas the shaded portions indicate the ANGST sub-sample for which *HST* resolved stellar populations observations are available.

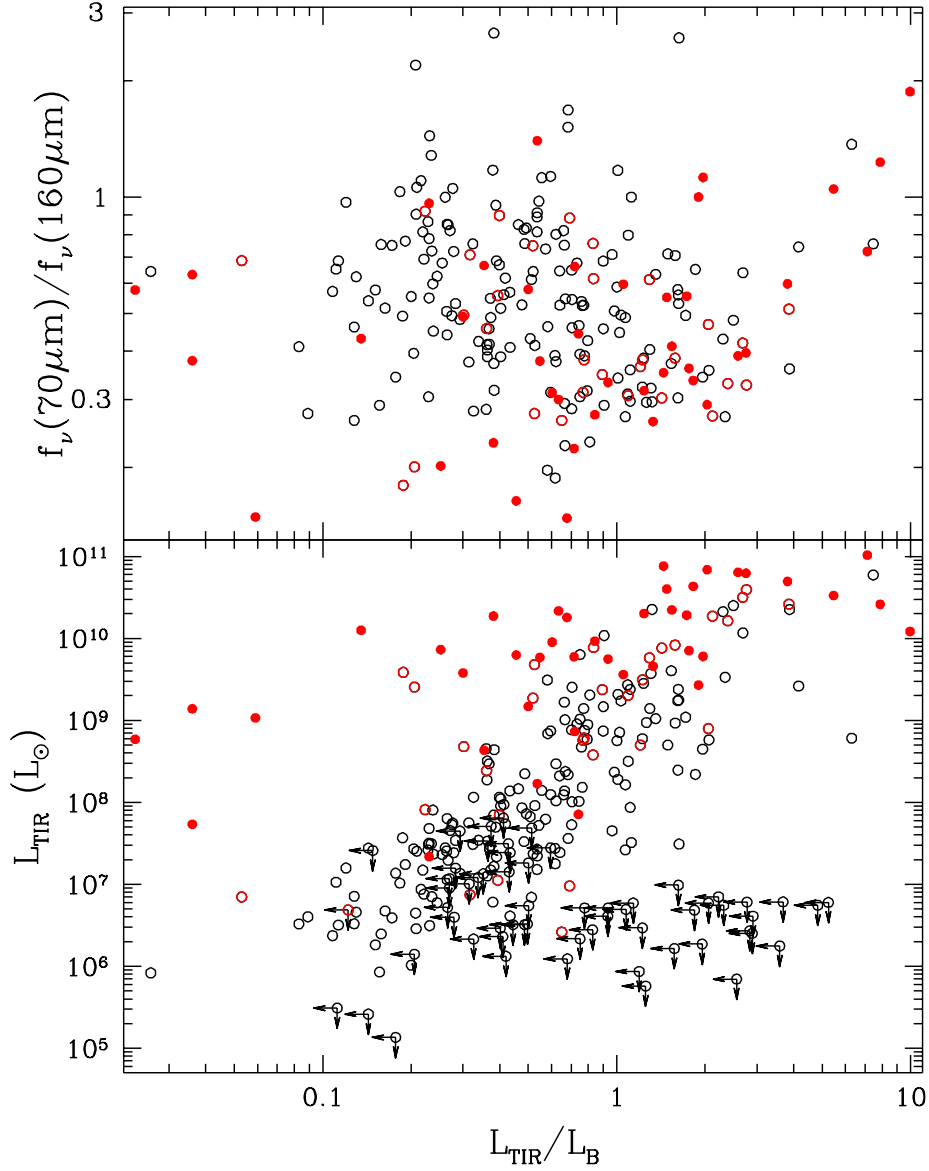


Fig. 3.— The range of 3–1100 μm total infrared and total infrared-to-optical properties in the LVL (open black circles) and SINGS (filled red circles) samples. Open red circles denote galaxies in both samples. SINGS data are taken from Dale et al. (2007). Arrows indicate 3σ upper limits.

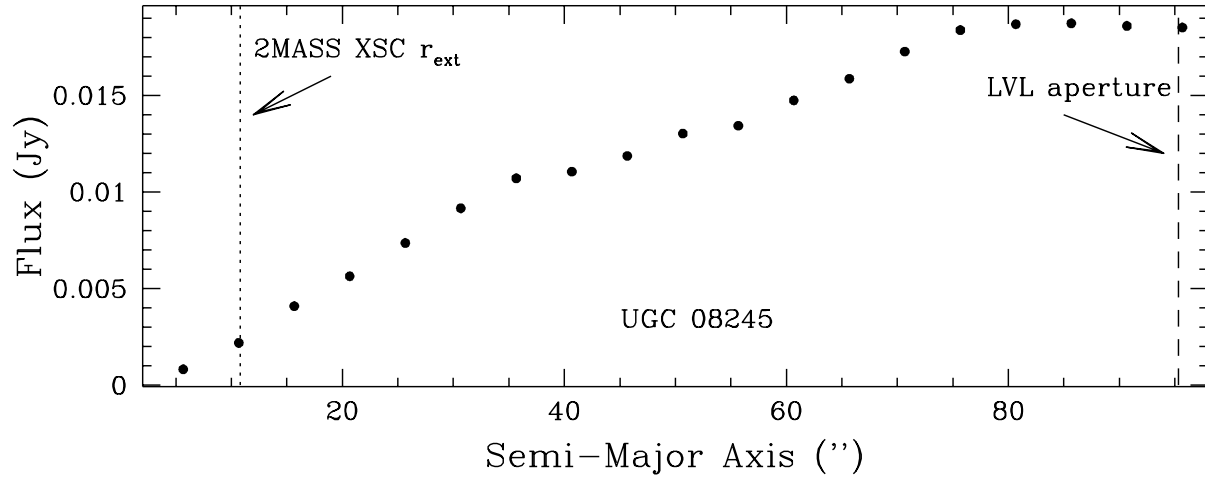


Fig. 4.— A K band curve-of-growth plot that includes a comparison of extraction apertures for UGC 08245 from our work (dashed line) and from the 2MASS ‘XSC’ Extended Source Catalog (dotted line). The larger aperture captures more of the faint diffuse emission from the galaxy’s disk.

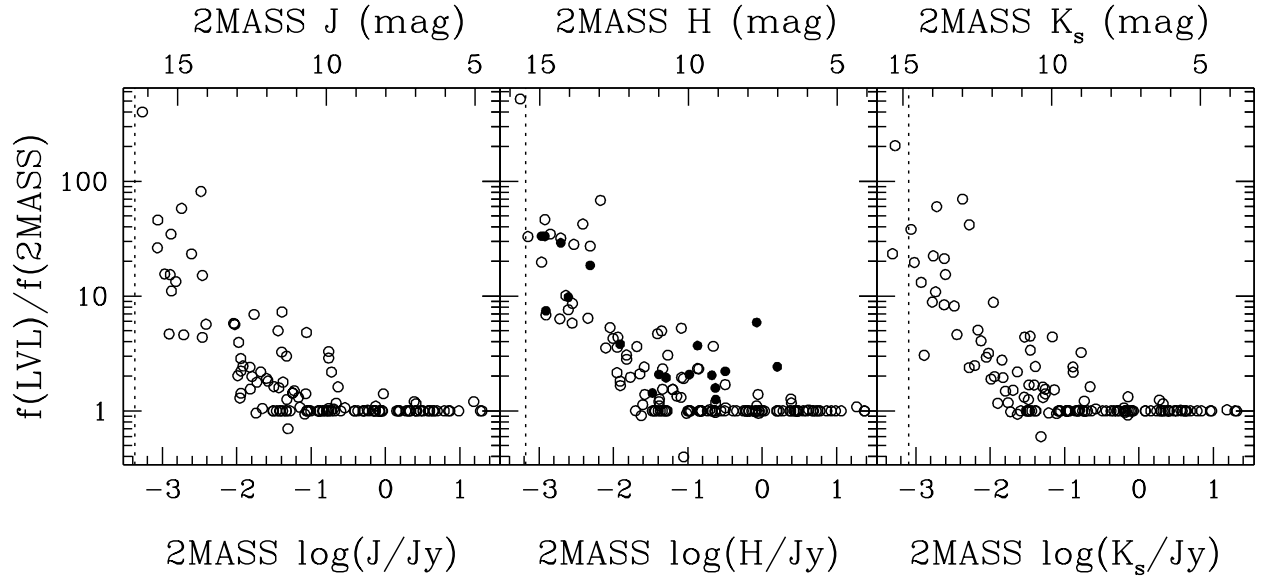


Fig. 5.— A comparison of near-infrared fluxes independently extracted from the 2MASS image archives using the apertures described in § 4.2 with those from the 2MASS Extended Source Catalog. The filled circles are based on deep H band imaging of nearby galaxies with the 3.9 m Anglo-Australian Telescope (Kirby et al. 2008). The vertical dotted lines indicate the 2MASS 10σ point source detection limits.

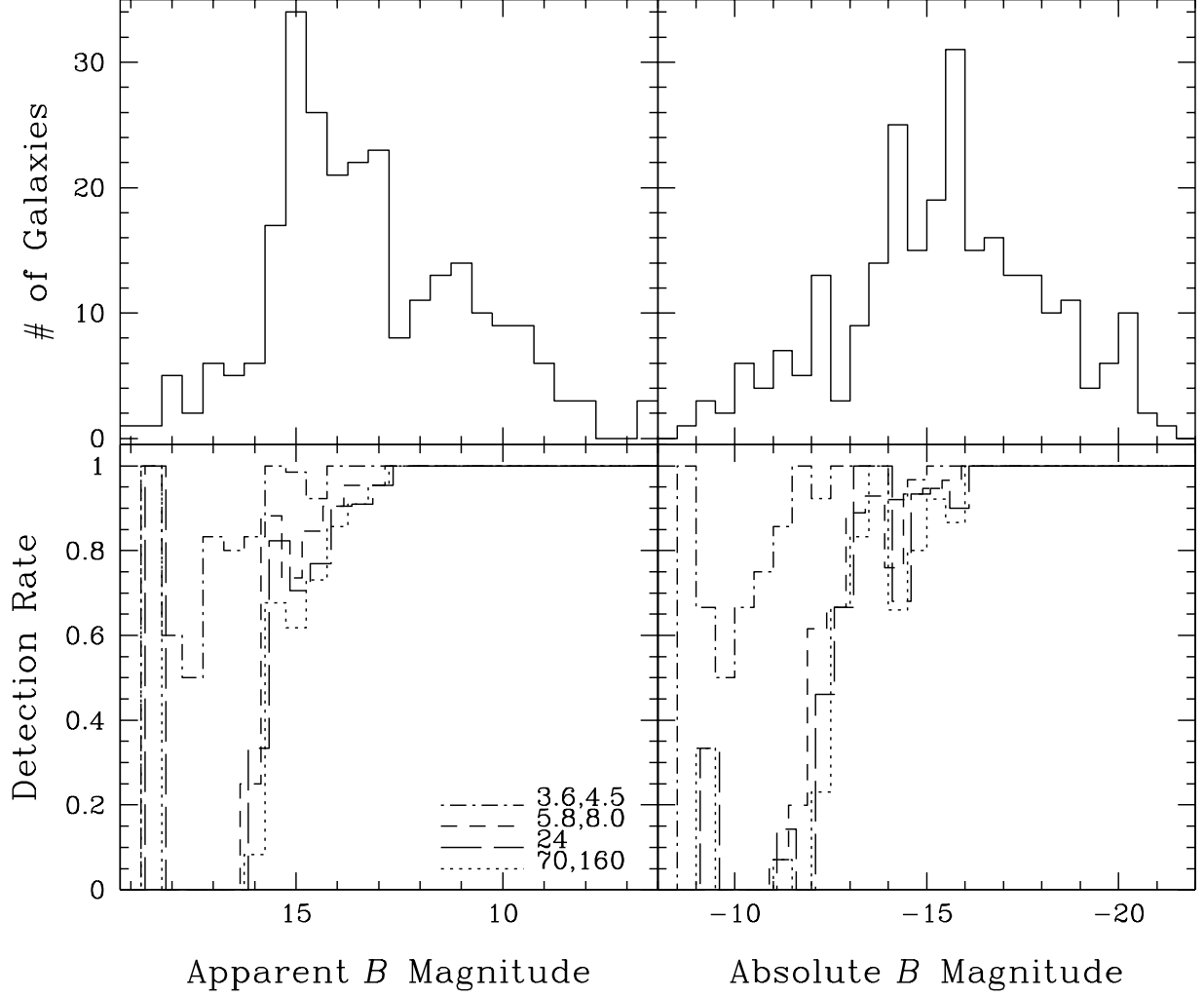


Fig. 6.— Top: The distribution of LVL galaxies as a function of apparent and absolute B -band magnitudes. Bottom: The imaging detection rates for different *Spitzer* wavelengths. Two histograms are slightly offset in magnitude for purposes of clarity. Note that the *average* detection rate is displayed at 3.6 and 4.5 μm (dot dashed line) and at 5.8 and 8.0 μm (short dashed line).

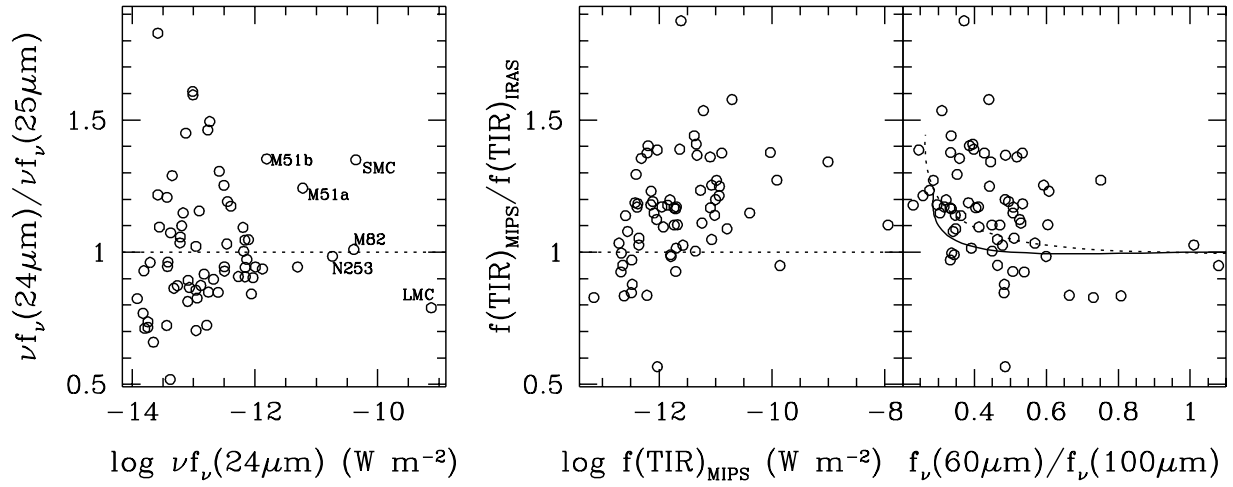


Fig. 7.— A comparison of *Spitzer* and *IRAS* data for the LVL sample. The left-most panel shows the ratio of *Spitzer* 24 μm and *IRAS* 25 μm data, and the right two panels compare the total infrared as measured from *Spitzer* and *IRAS*. The dotted line in the left two panels indicate a ratio of unity, whereas the solid and dotted lines in the right-most panel indicate model predictions from Dale & Helou (2002) and Dale et al. (2001), respectively.

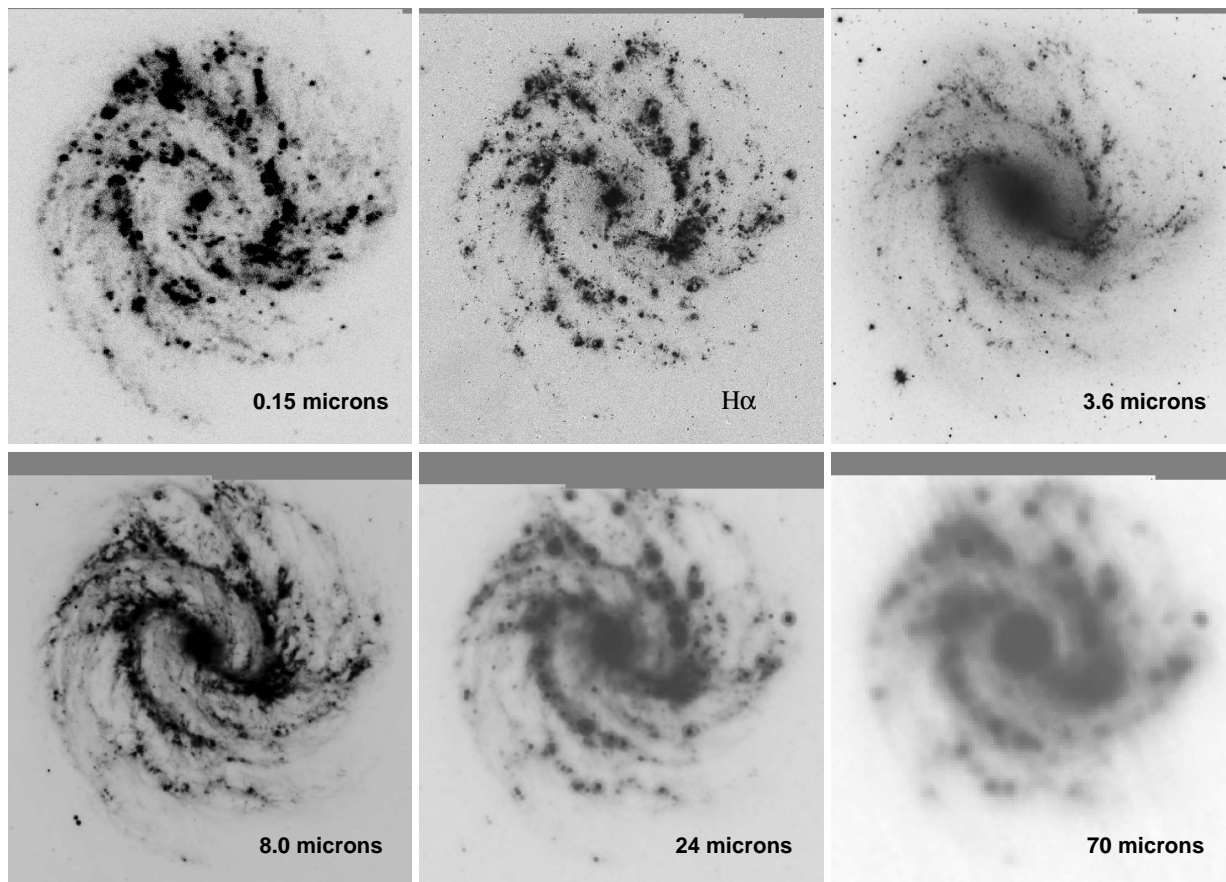


Fig. 8.— A multi-wavelength mosaic of spiral galaxy NGC 5236, displaying the range of imaging available for the LVL survey. The H α image is continuum-subtracted. The images are all $9'.9 \times 10'.7$, or $13 \text{ kpc} \times 14 \text{ kpc}$ at a distance of 4.47 Mpc.

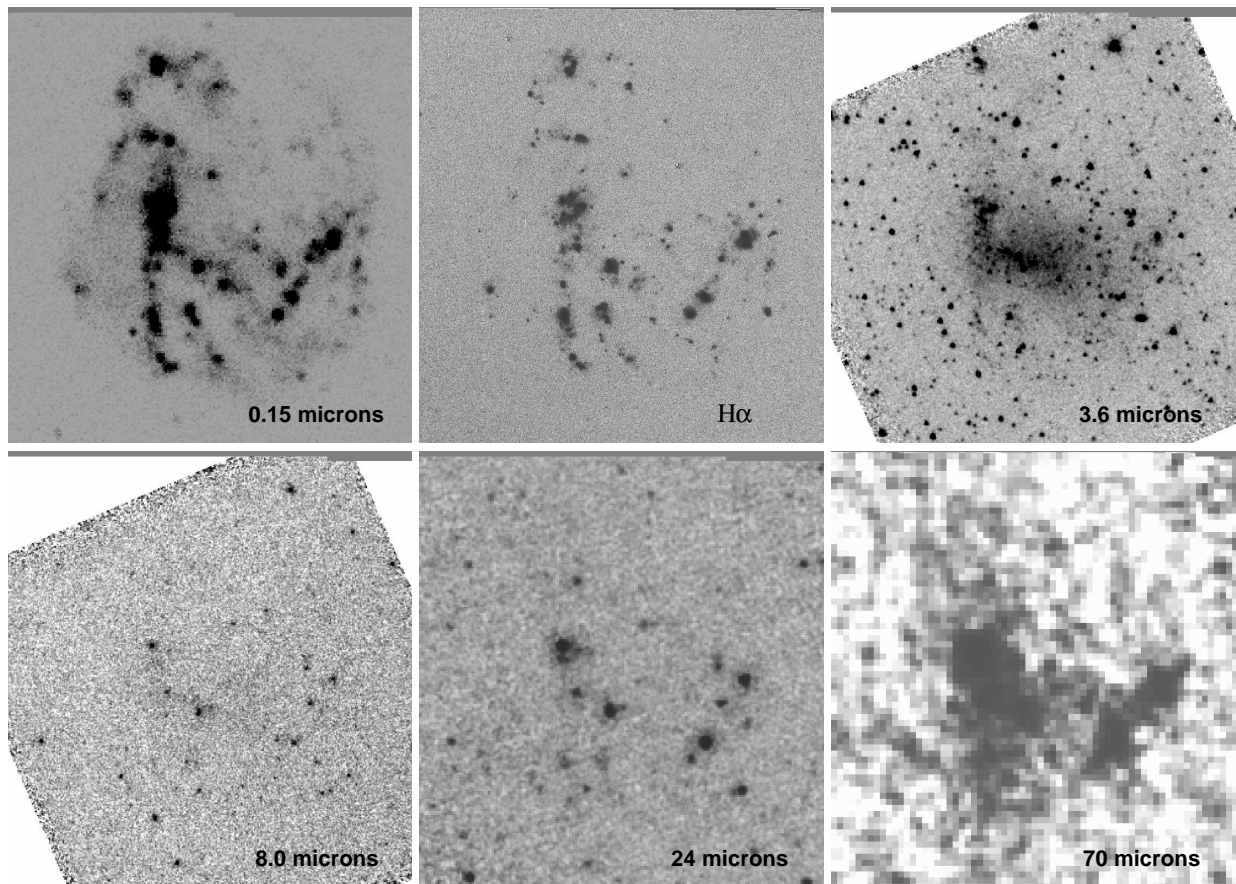


Fig. 9.— The same as Figure 8 but for the irregular galaxy UGC 05829. The images are all $5'.0 \times 5'.4$, or $11 \text{ kpc} \times 12 \text{ kpc}$ at a distance of 7.88 Mpc.

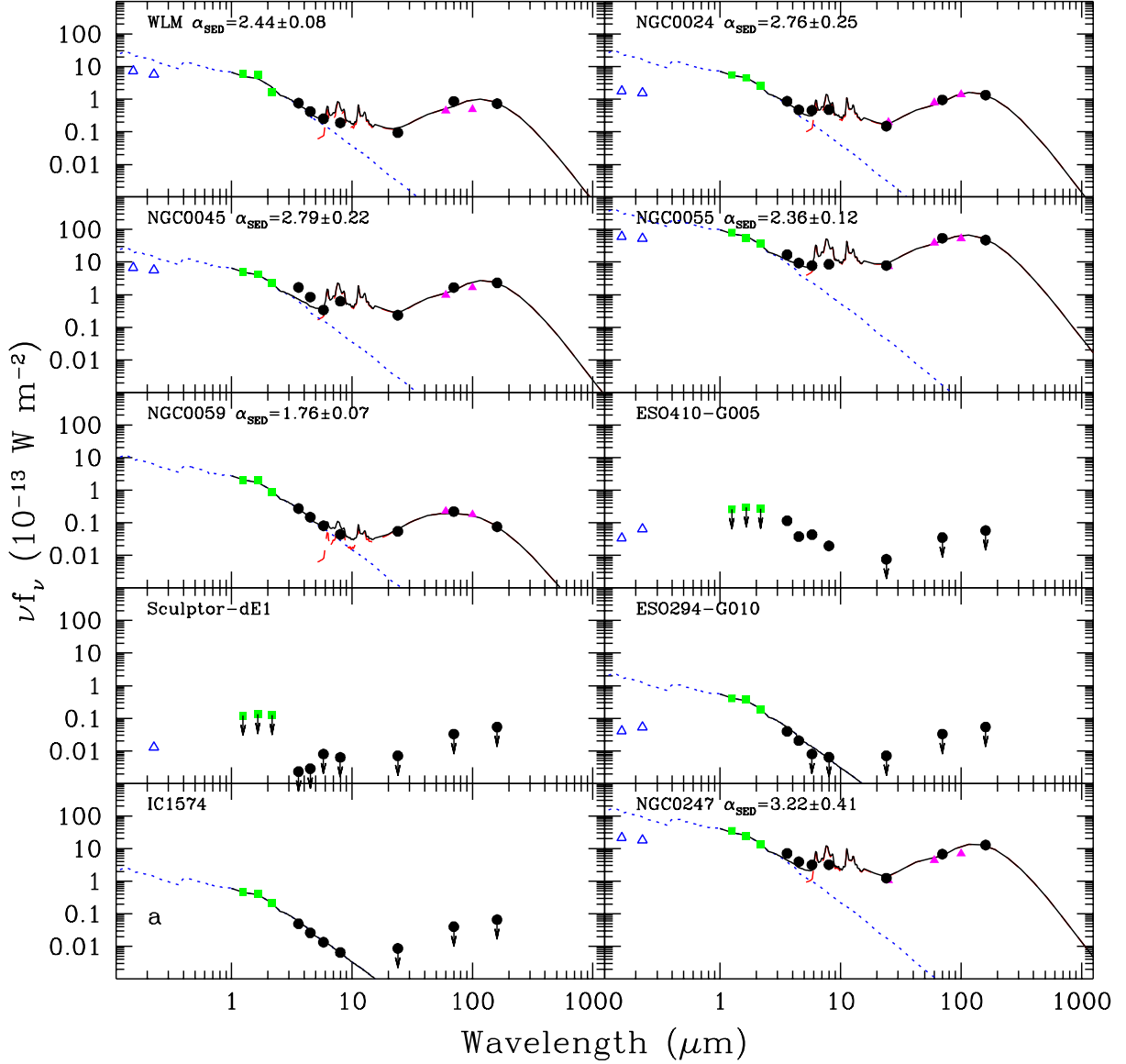


Fig. 10.— Globally-integrated 0.15–160 μm spectral energy distributions for the LVL sample. *GALEX*, 2MASS, *IRAS*, and *Spitzer* data are represented by open triangles, filled squares, filled triangles, and filled circles, respectively. Downward-pointing arrows, if present, indicate 5σ upper limits. The solid curve is the sum of a dust (dashed) and a stellar (dotted) model. The dust curve is a Dale & Helou (2002) model fitted to the amplitude and ratios of the observed 24, 70, and 160 μm fluxes; the α_{SED} listed within each panel parameterizes the distribution of dust mass as a function of heating intensity, as described in Dale & Helou (2002). The stellar curve, serving merely as a fiducial visual aid, is a 1 Gyr continuous star formation, solar metallicity curve from Vazquez & Leitherer (2005) fitted to the 2MASS data (see § 5.3 for details).

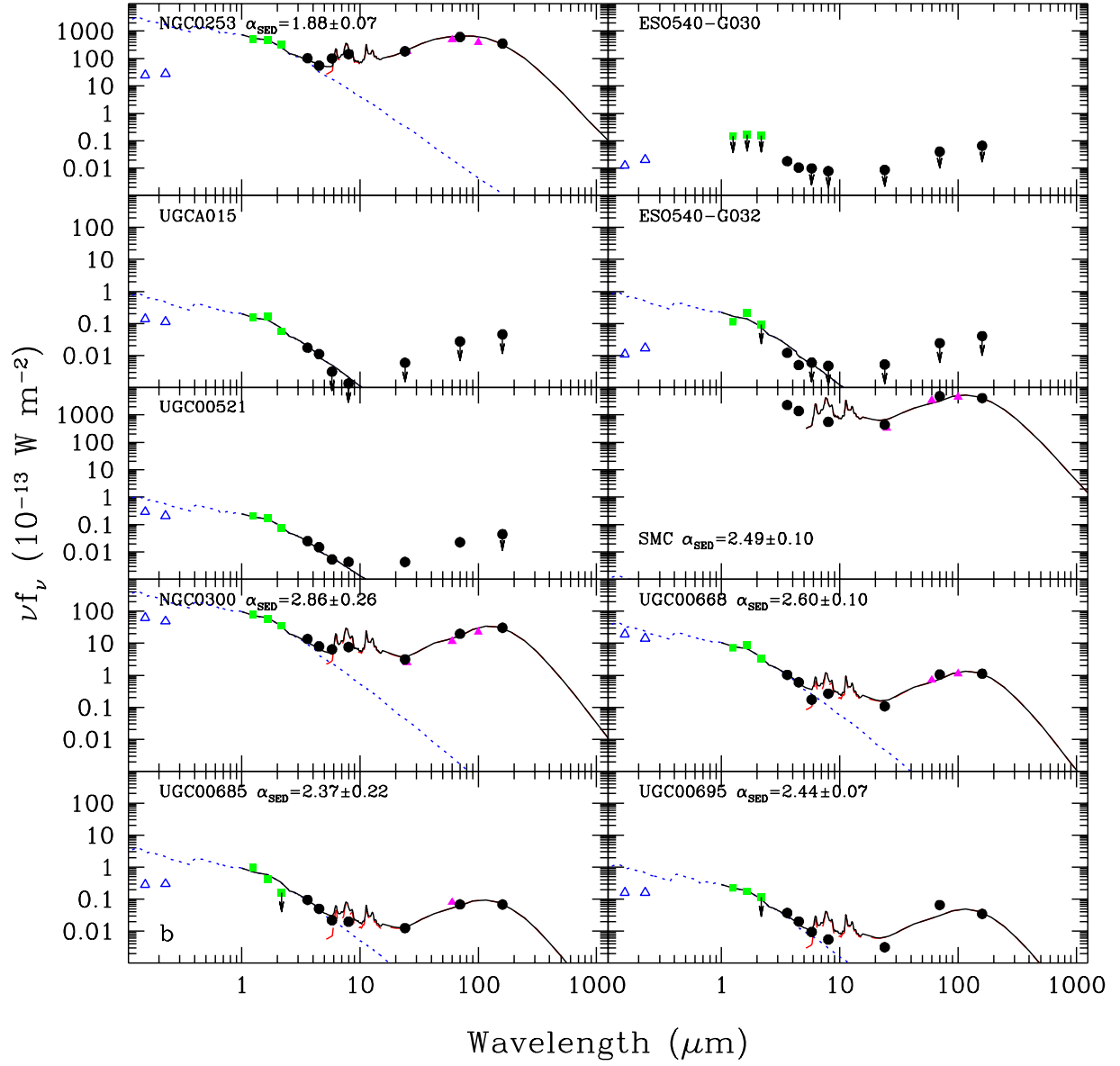


Fig. 10.— Globally-integrated 0.15-160 μm spectral energy distributions for the LVL sample (continued).

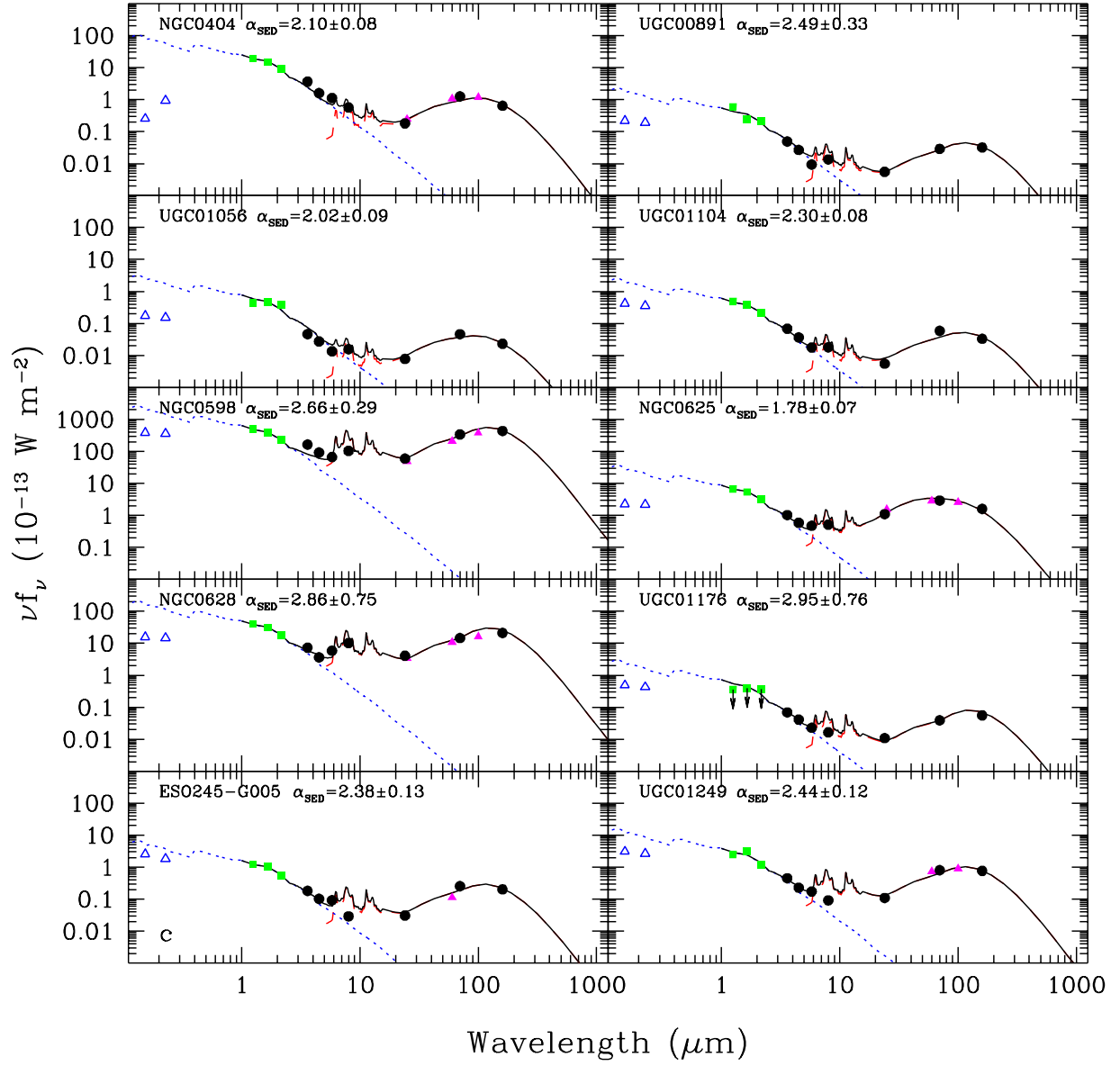


Fig. 10.— Globally-integrated 0.15-160 μm spectral energy distributions for the LVL sample (continued).

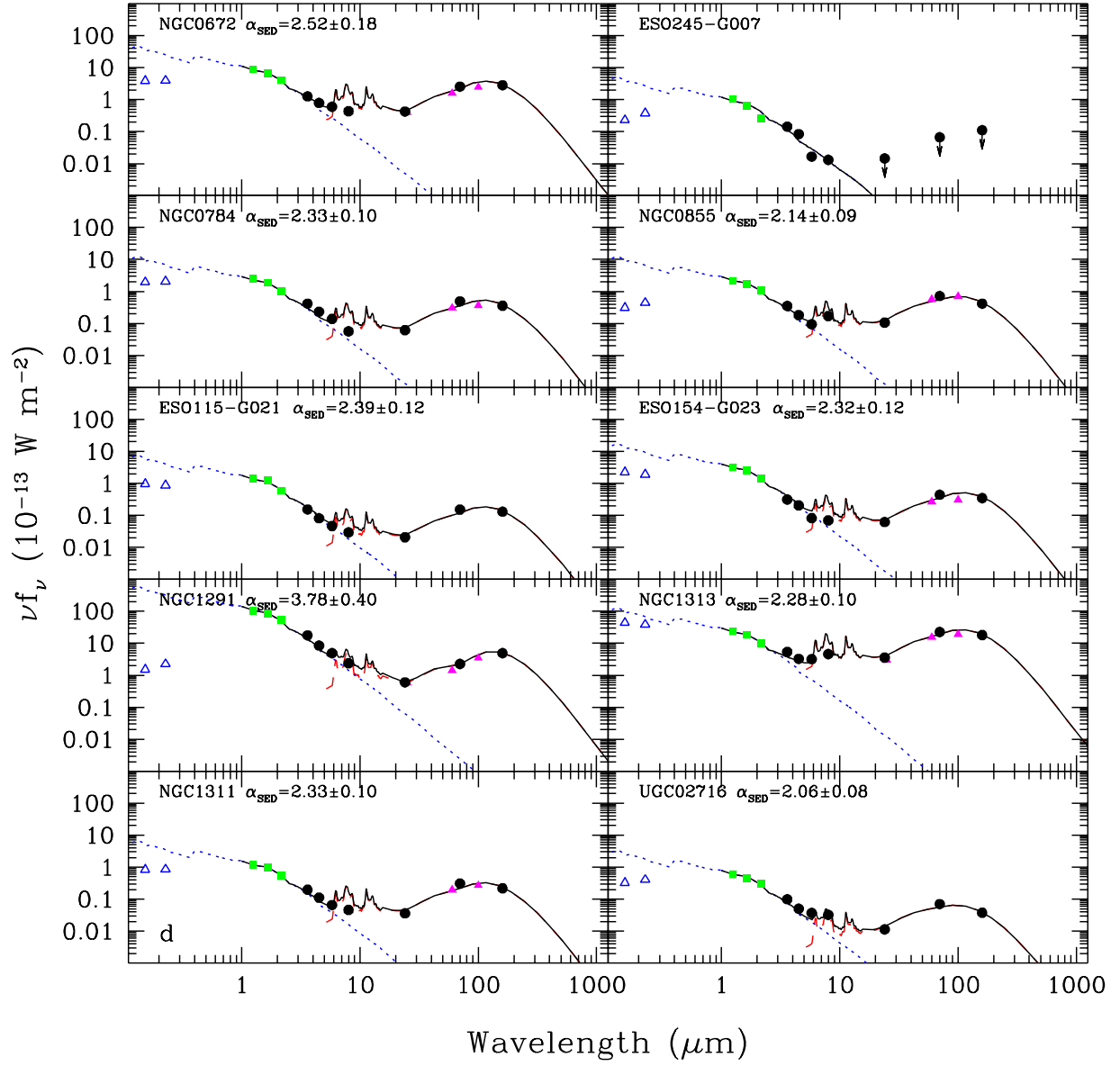


Fig. 10.— Globally-integrated 0.15-160 μm spectral energy distributions for the LVL sample (continued).

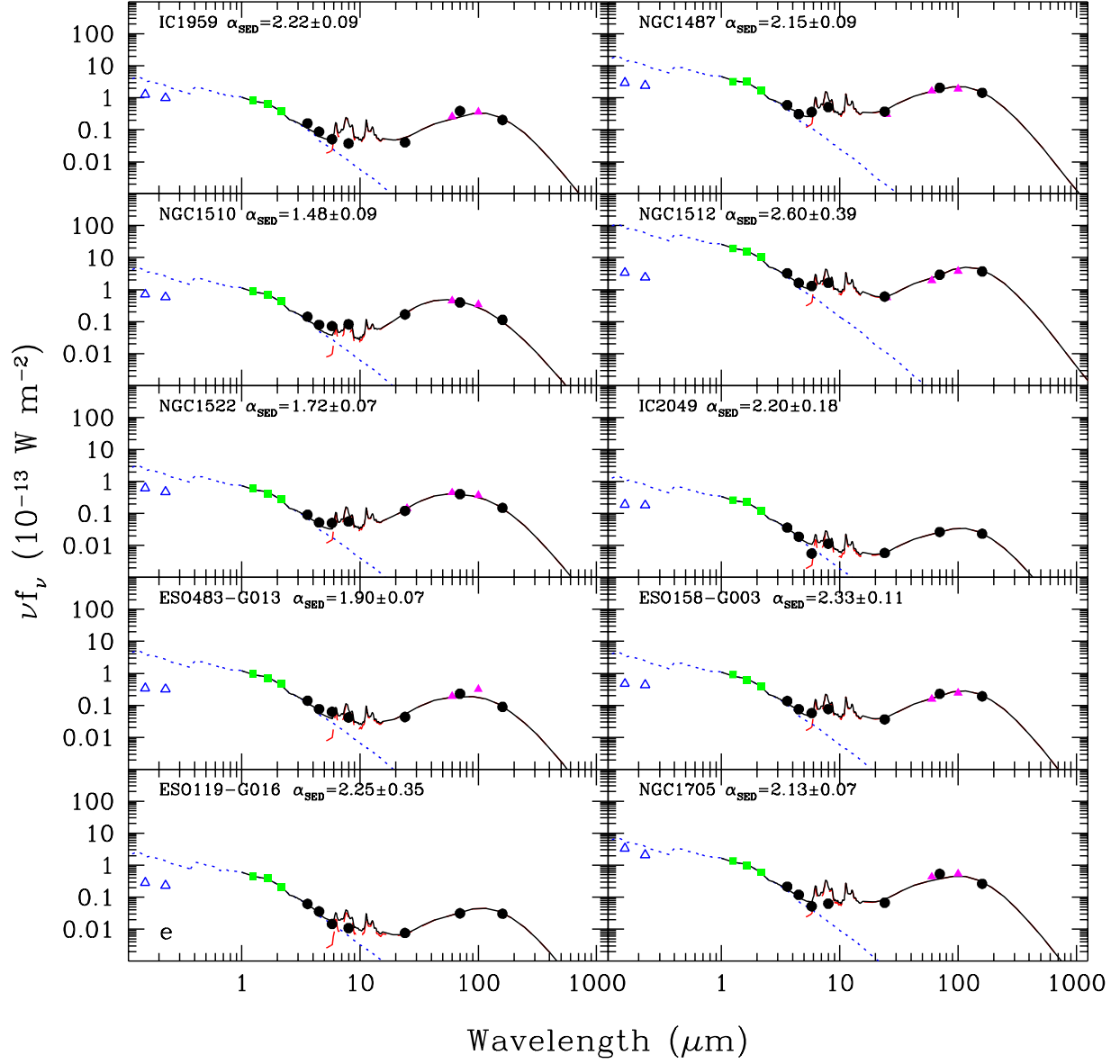


Fig. 10.— Globally-integrated 0.15-160 μm spectral energy distributions for the LVL sample (continued).

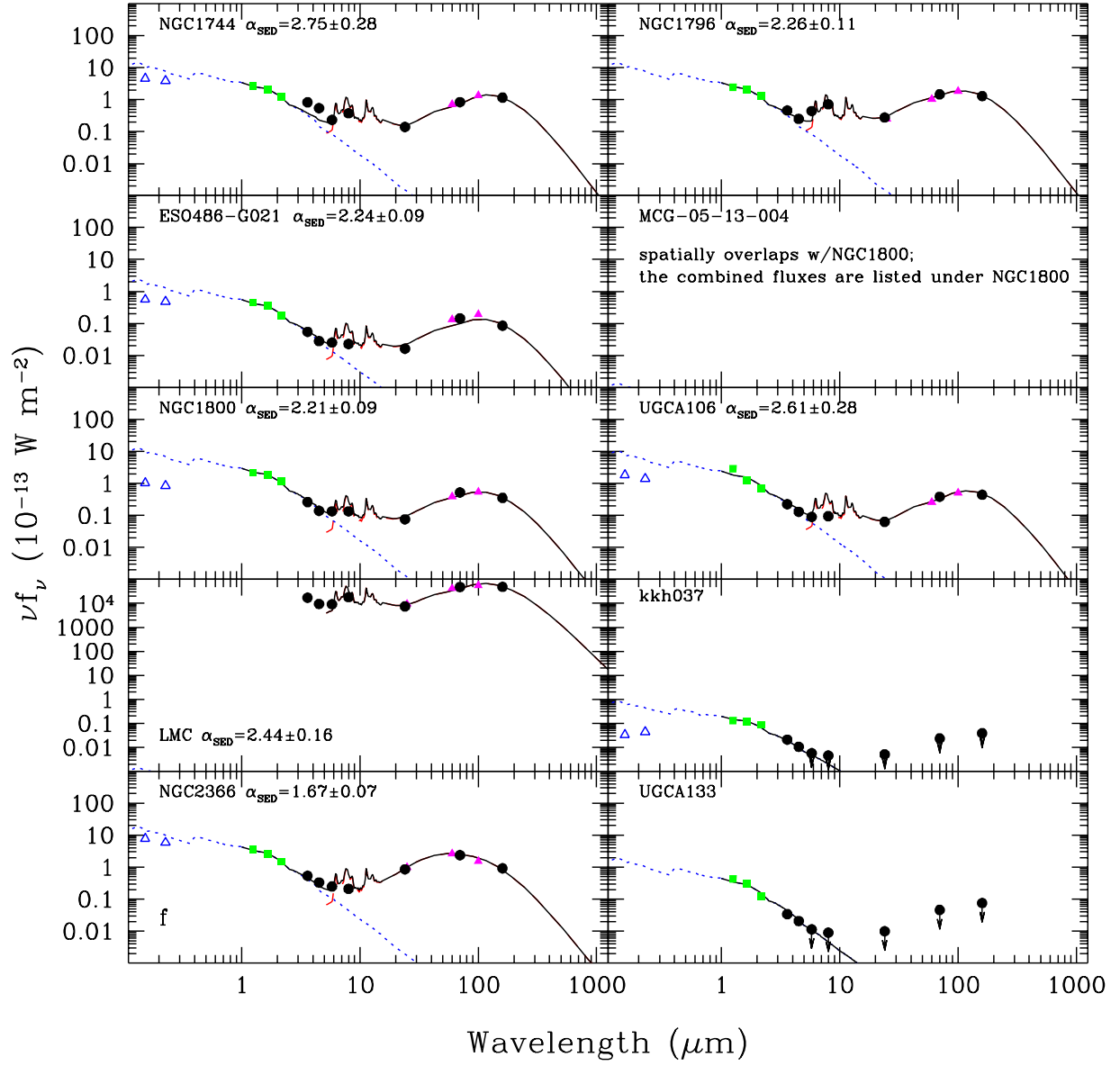


Fig. 10.— Globally-integrated 0.15-160 μm spectral energy distributions for the LVL sample (continued).

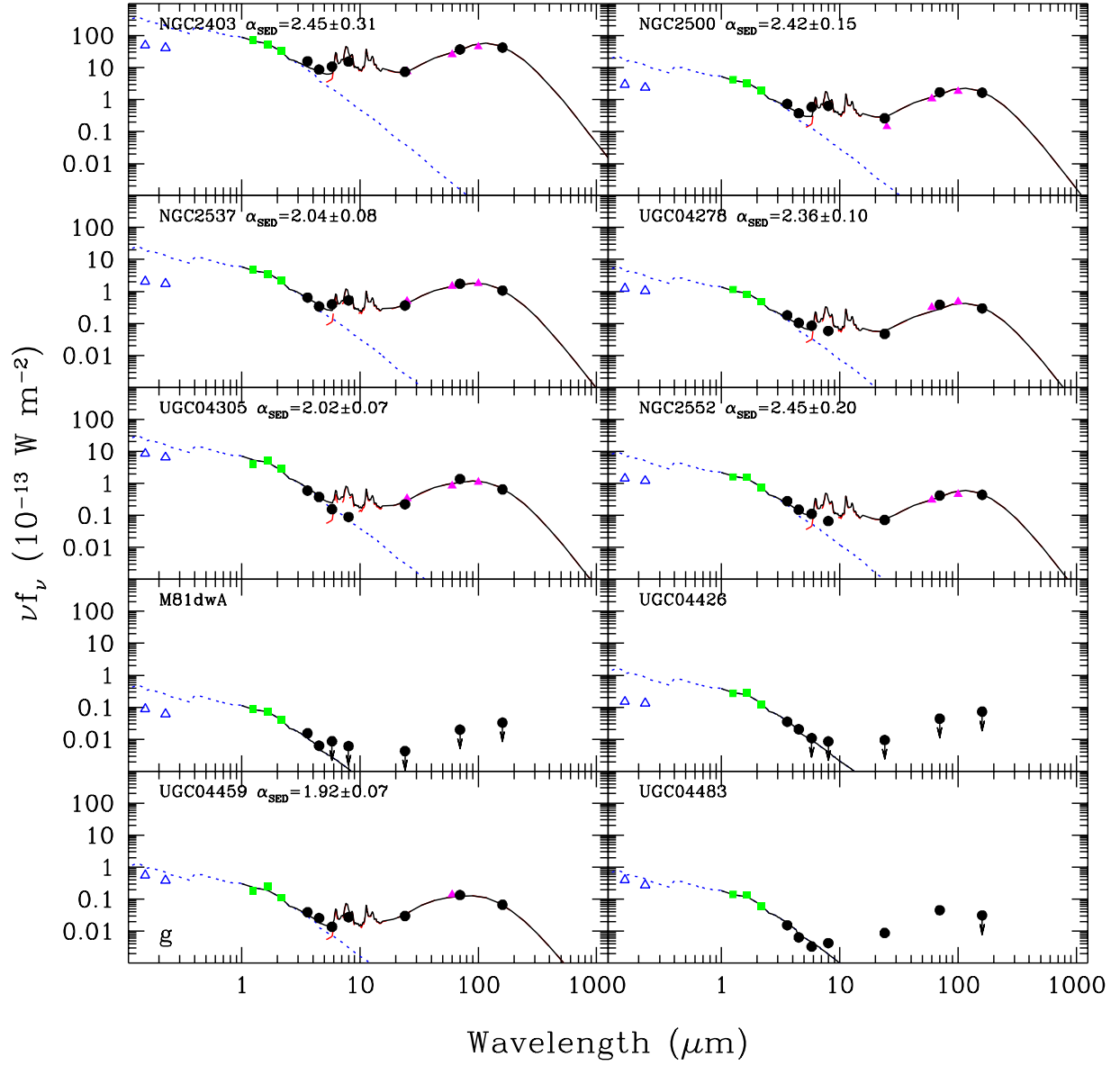


Fig. 10.— Globally-integrated 0.15-160 μm spectral energy distributions for the LVL sample (continued).

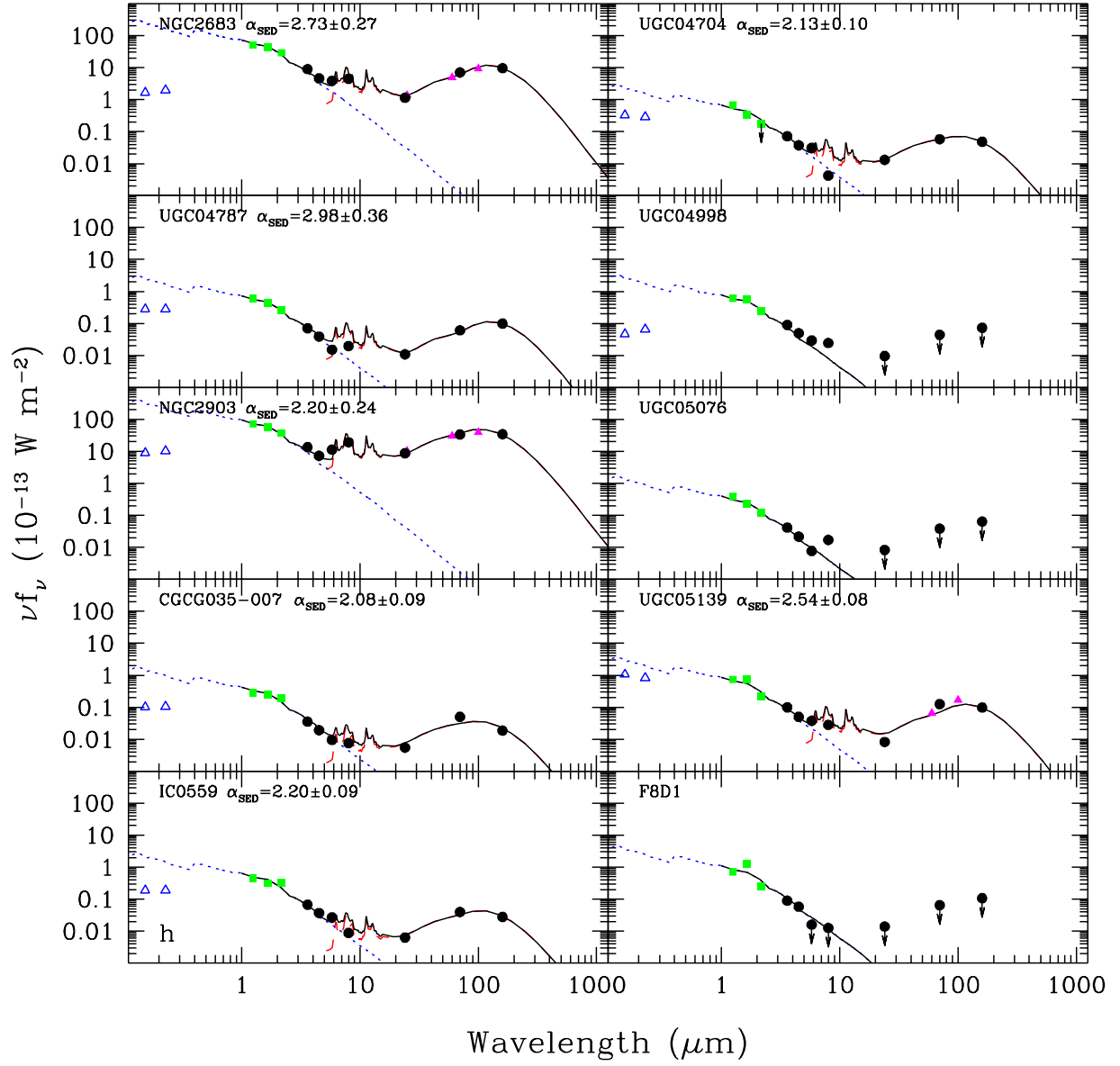


Fig. 10.— Globally-integrated 0.15-160 μm spectral energy distributions for the LVL sample (continued).

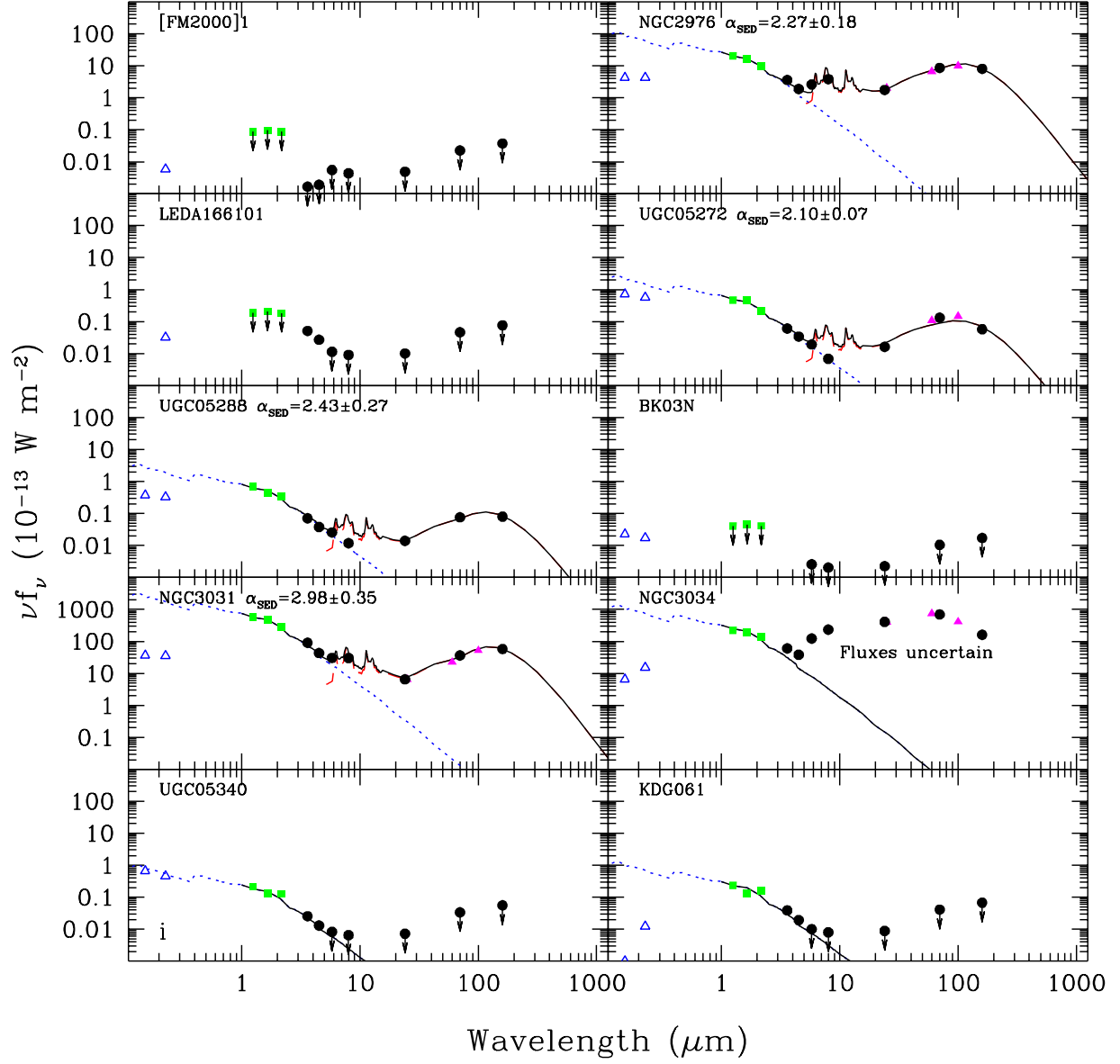


Fig. 10.— Globally-integrated 0.15-160 μm spectral energy distributions for the LVL sample (continued).

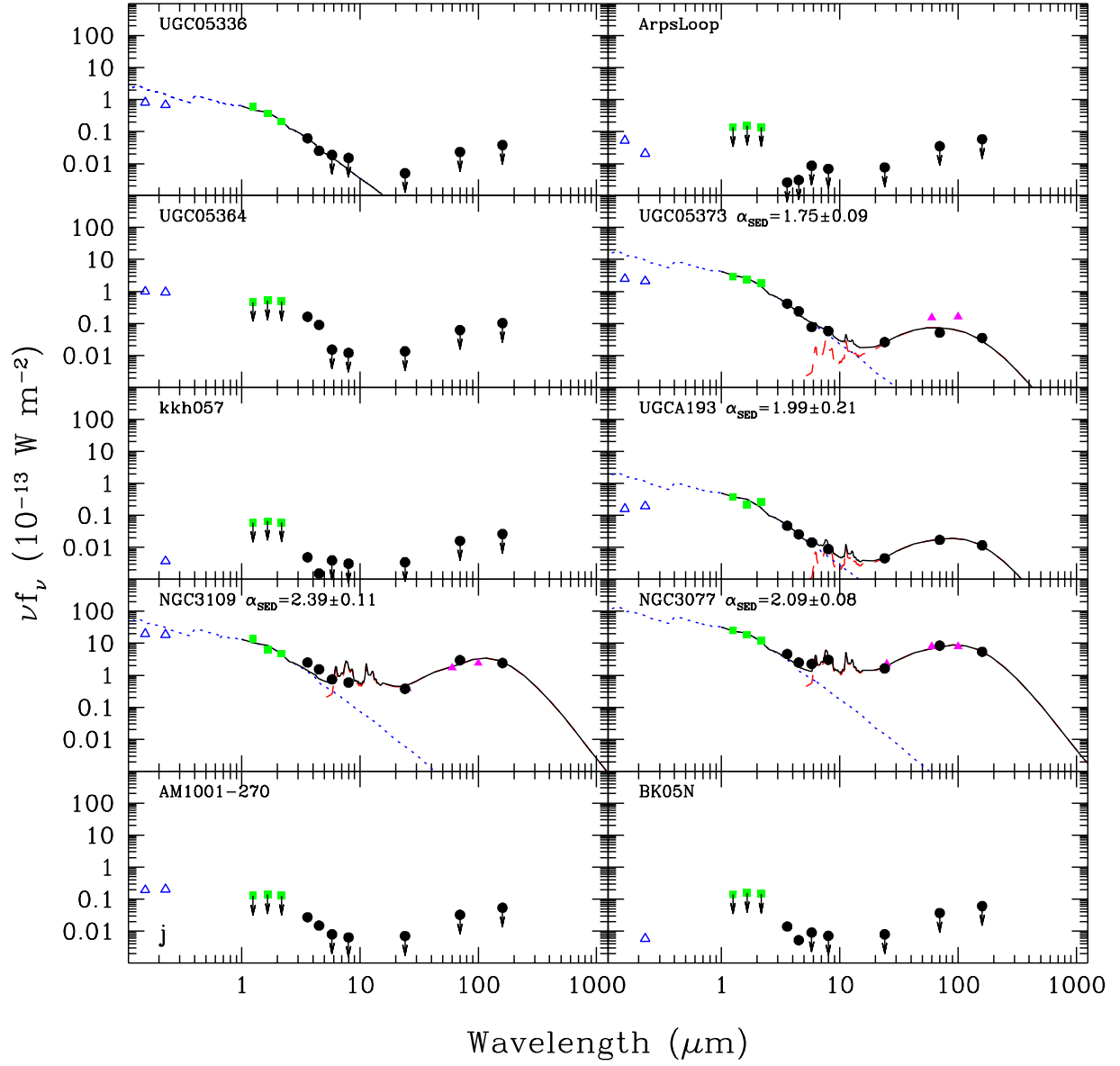


Fig. 10.— Globally-integrated 0.15-160 μm spectral energy distributions for the LVL sample (continued).

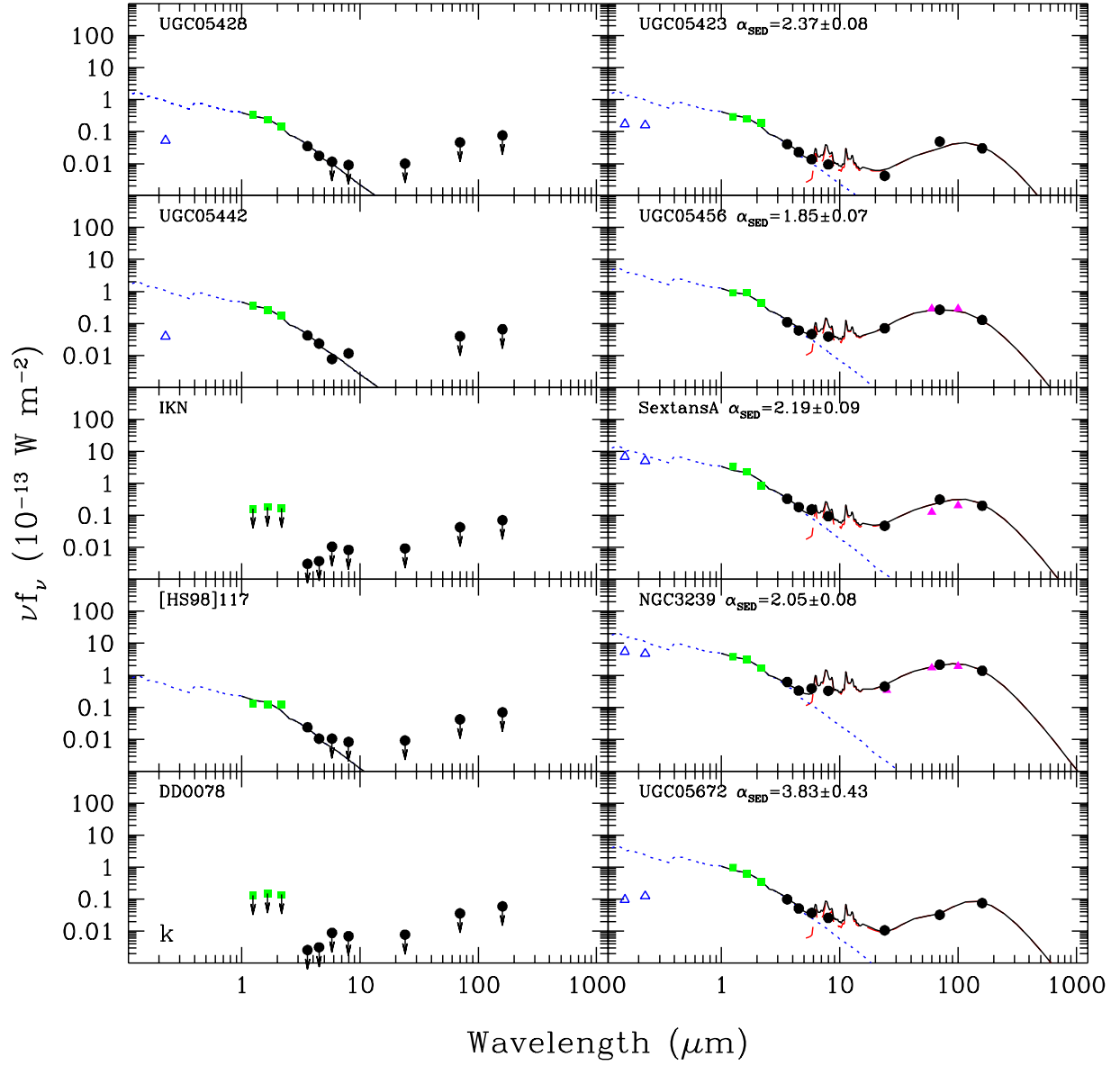


Fig. 10.— Globally-integrated 0.15-160 μm spectral energy distributions for the LVL sample (continued).

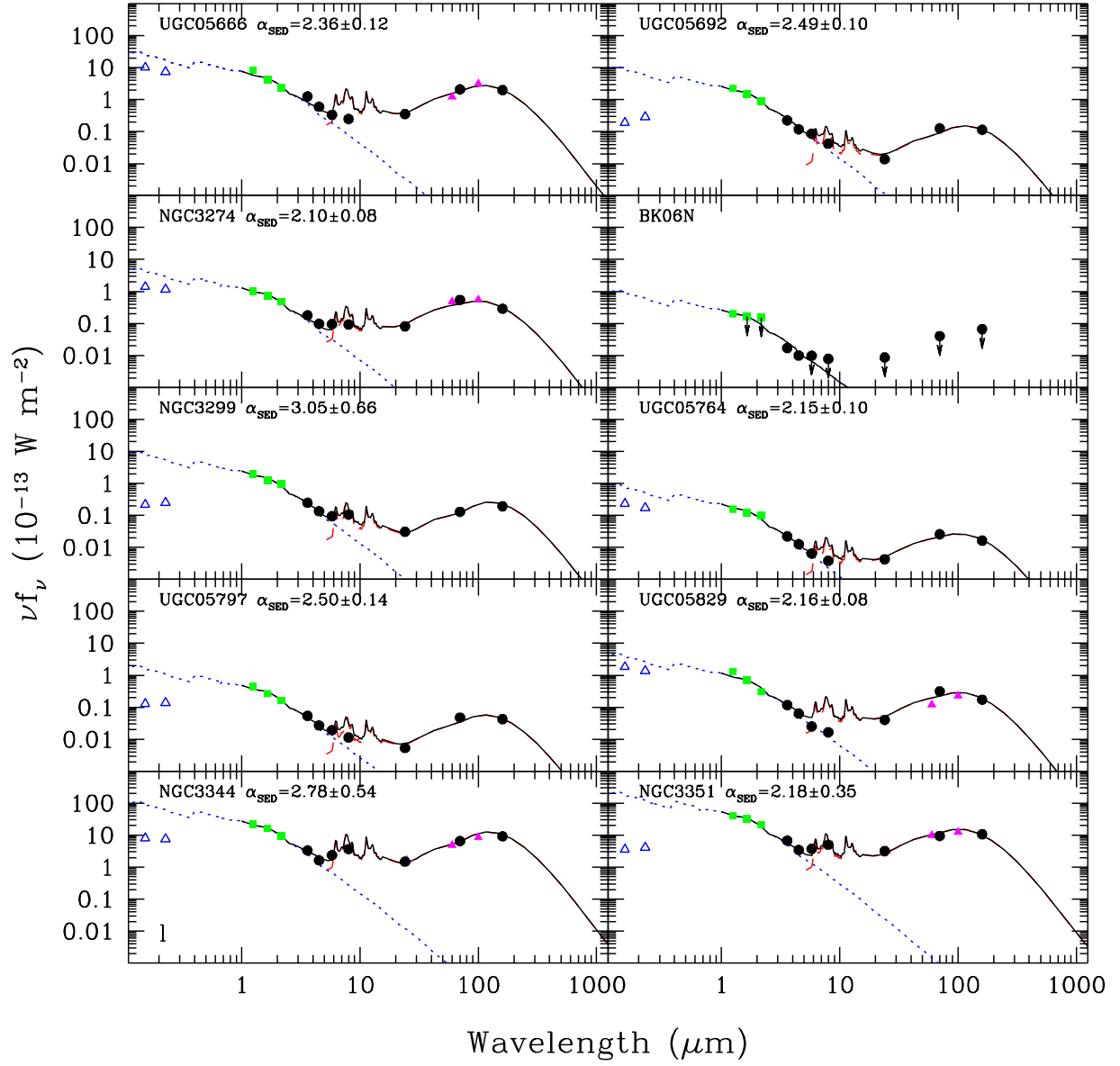


Fig. 10.— Globally-integrated 0.15–160 μm spectral energy distributions for the LVL sample (continued).

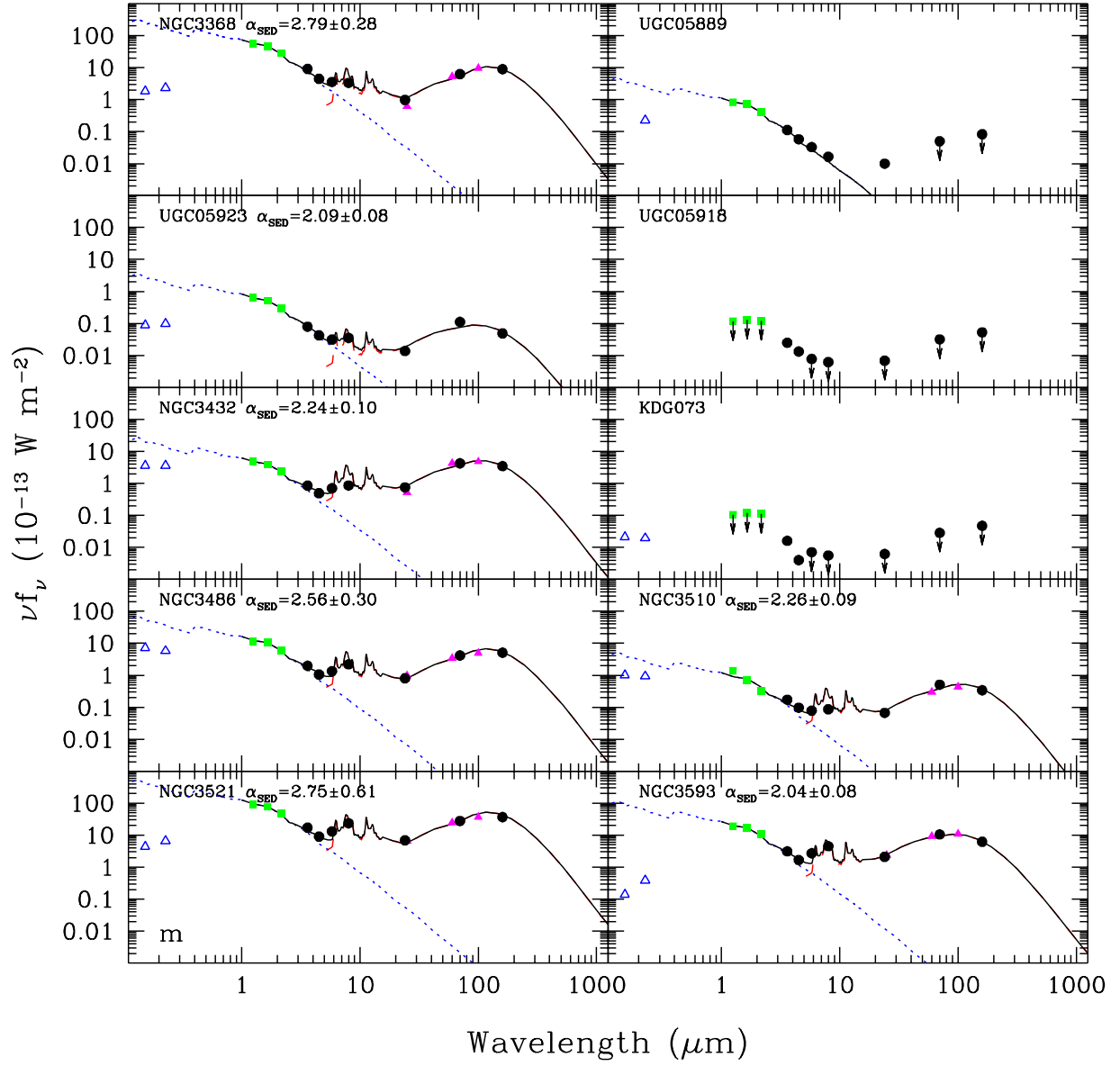


Fig. 10.— Globally-integrated 0.15-160 μm spectral energy distributions for the LVL sample (continued).

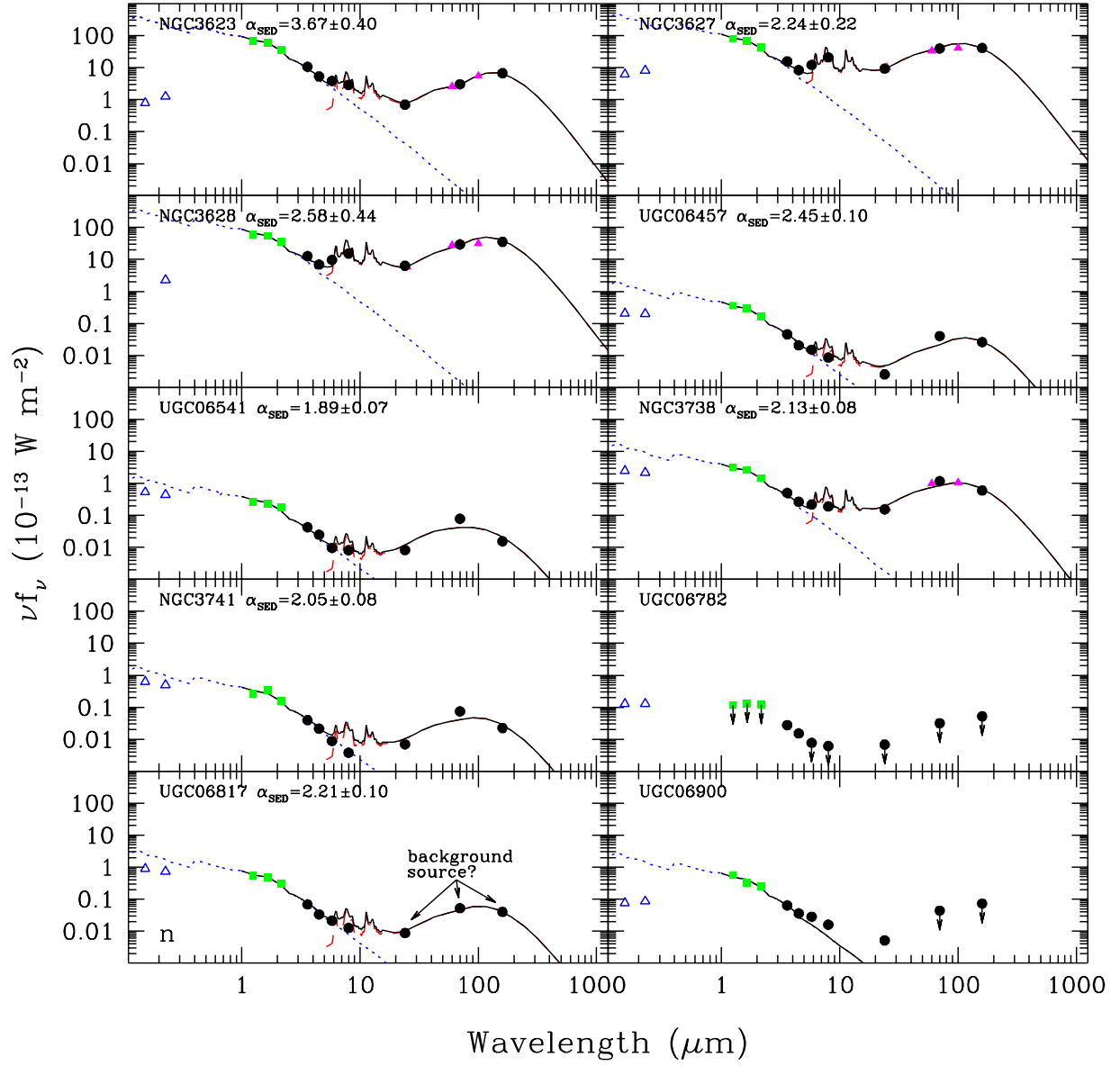


Fig. 10.— Globally-integrated 0.15-160 μm spectral energy distributions for the LVL sample (continued).

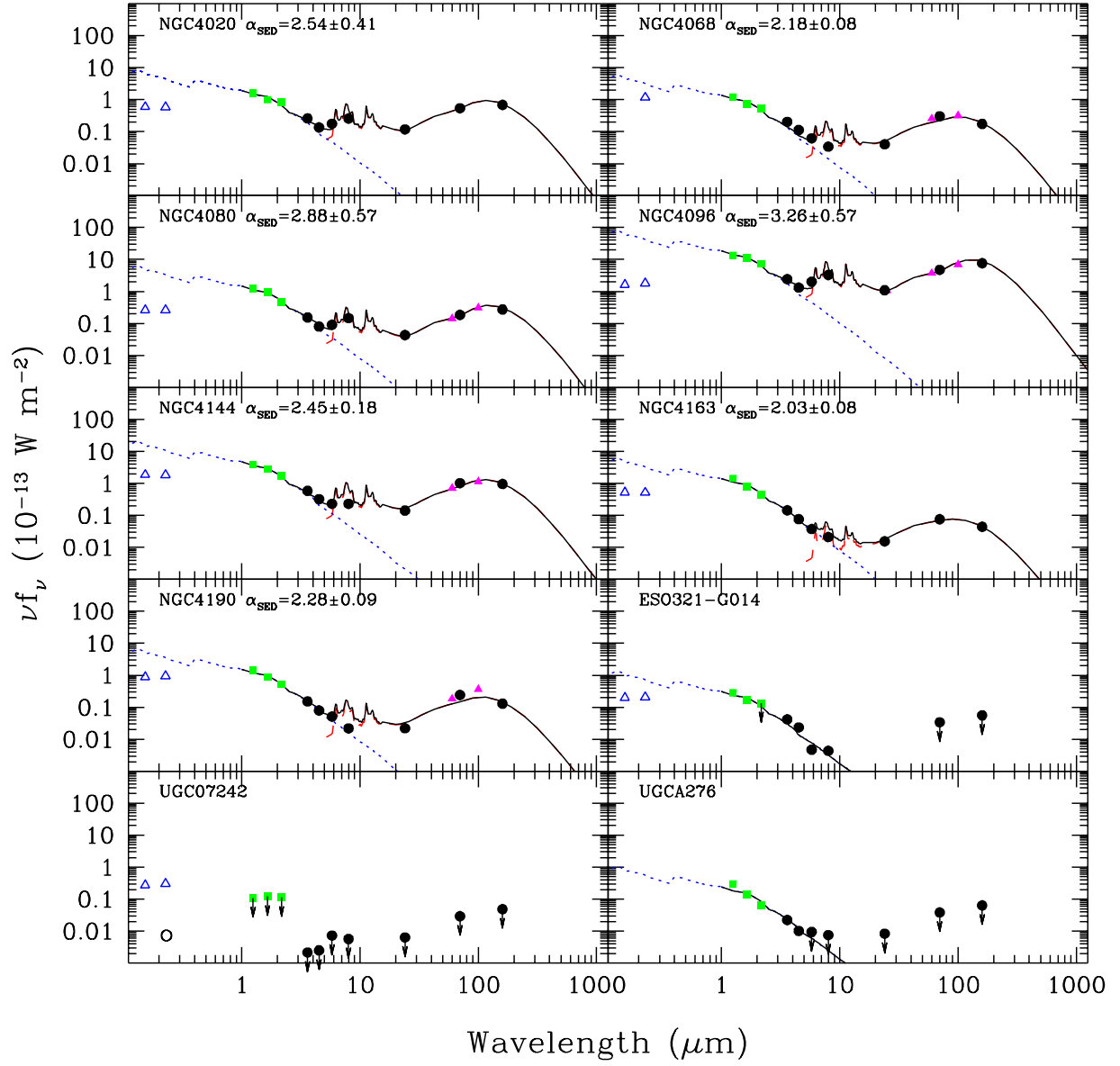


Fig. 10.— Globally-integrated 0.15-160 μm spectral energy distributions for the LVL sample (continued).

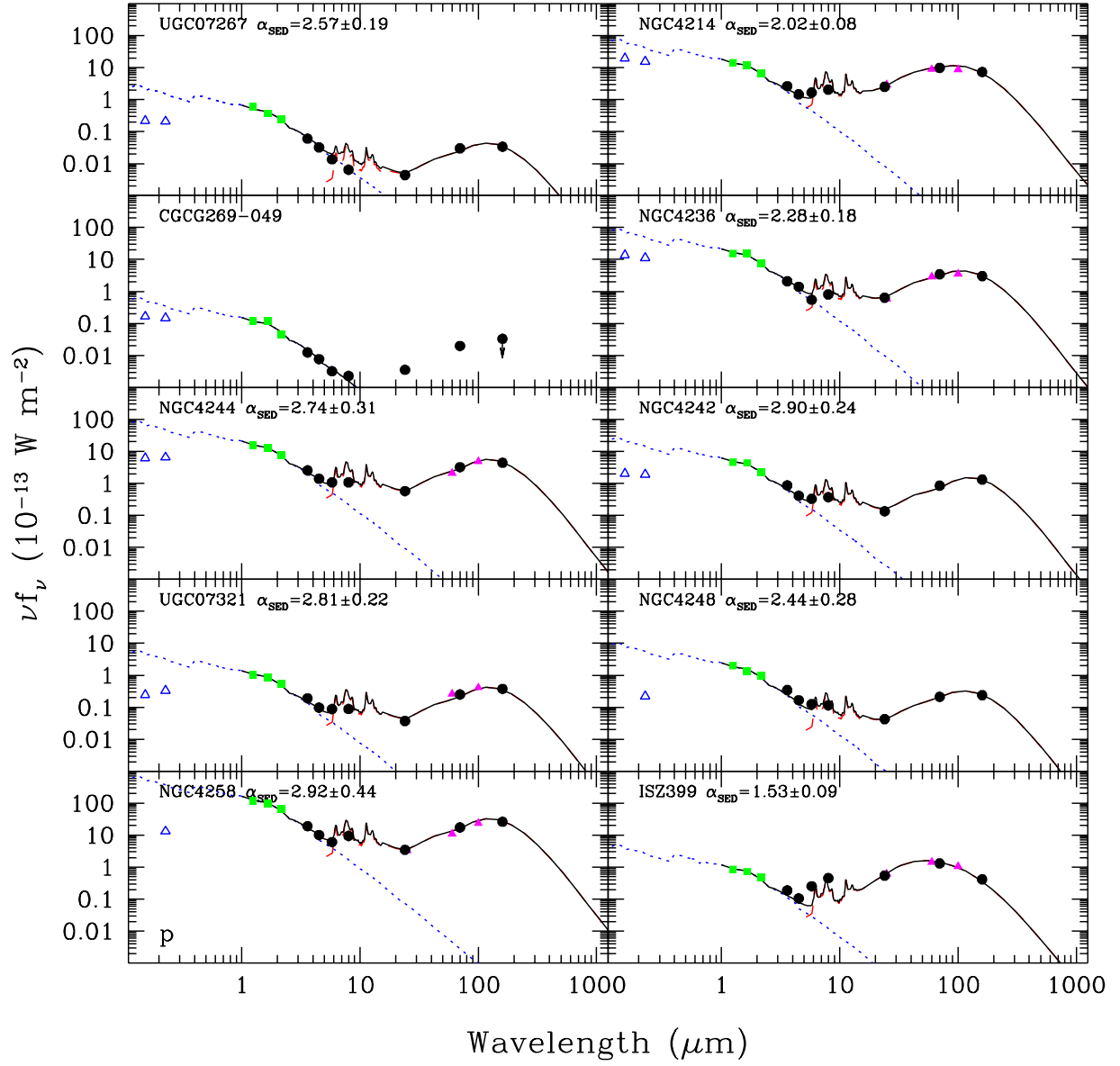


Fig. 10.— Globally-integrated 0.15-160 μm spectral energy distributions for the LVL sample (continued).

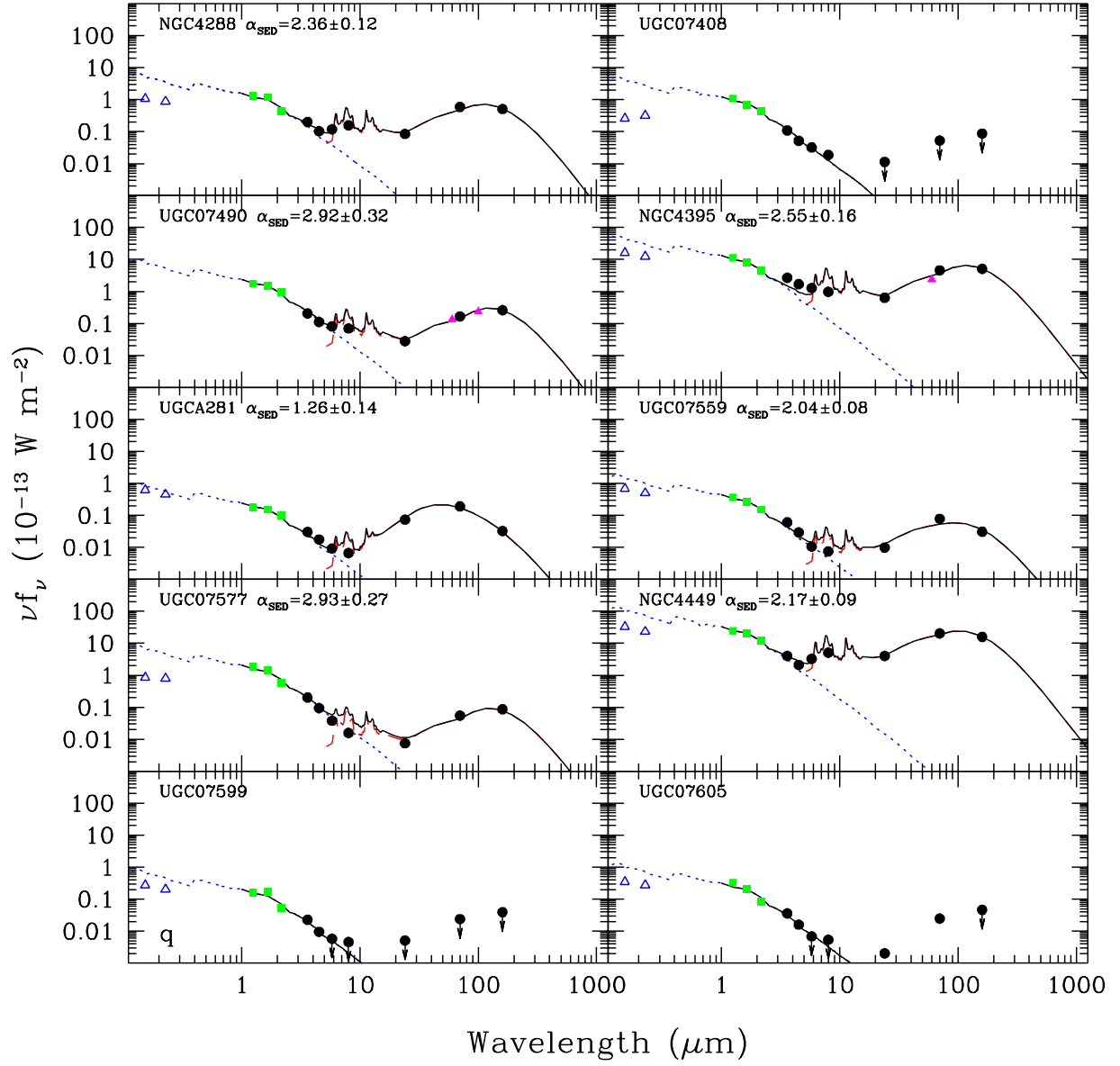


Fig. 10.— Globally-integrated 0.15-160 μm spectral energy distributions for the LVL sample (continued).

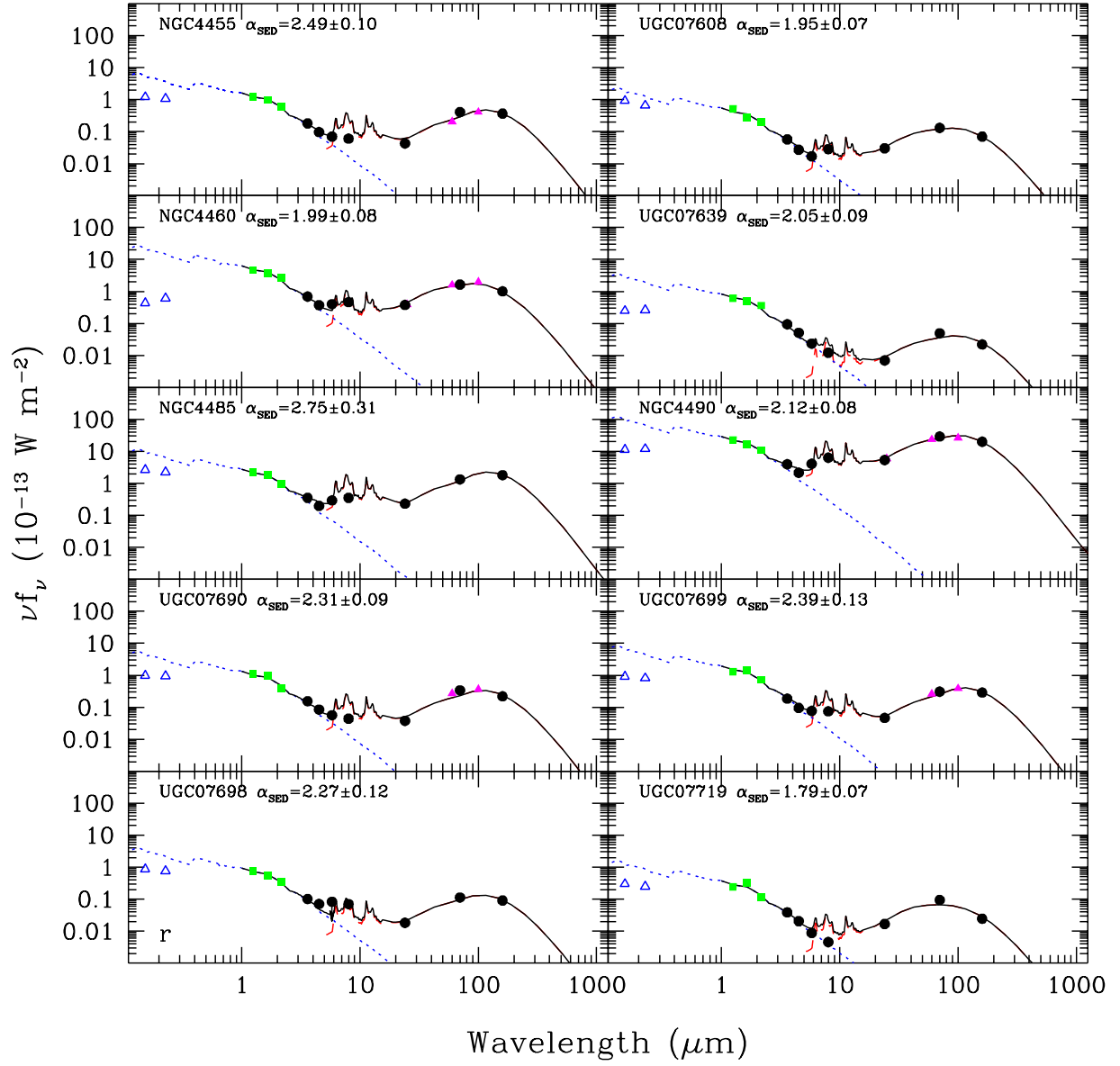


Fig. 10.— Globally-integrated 0.15-160 μm spectral energy distributions for the LVL sample (continued).

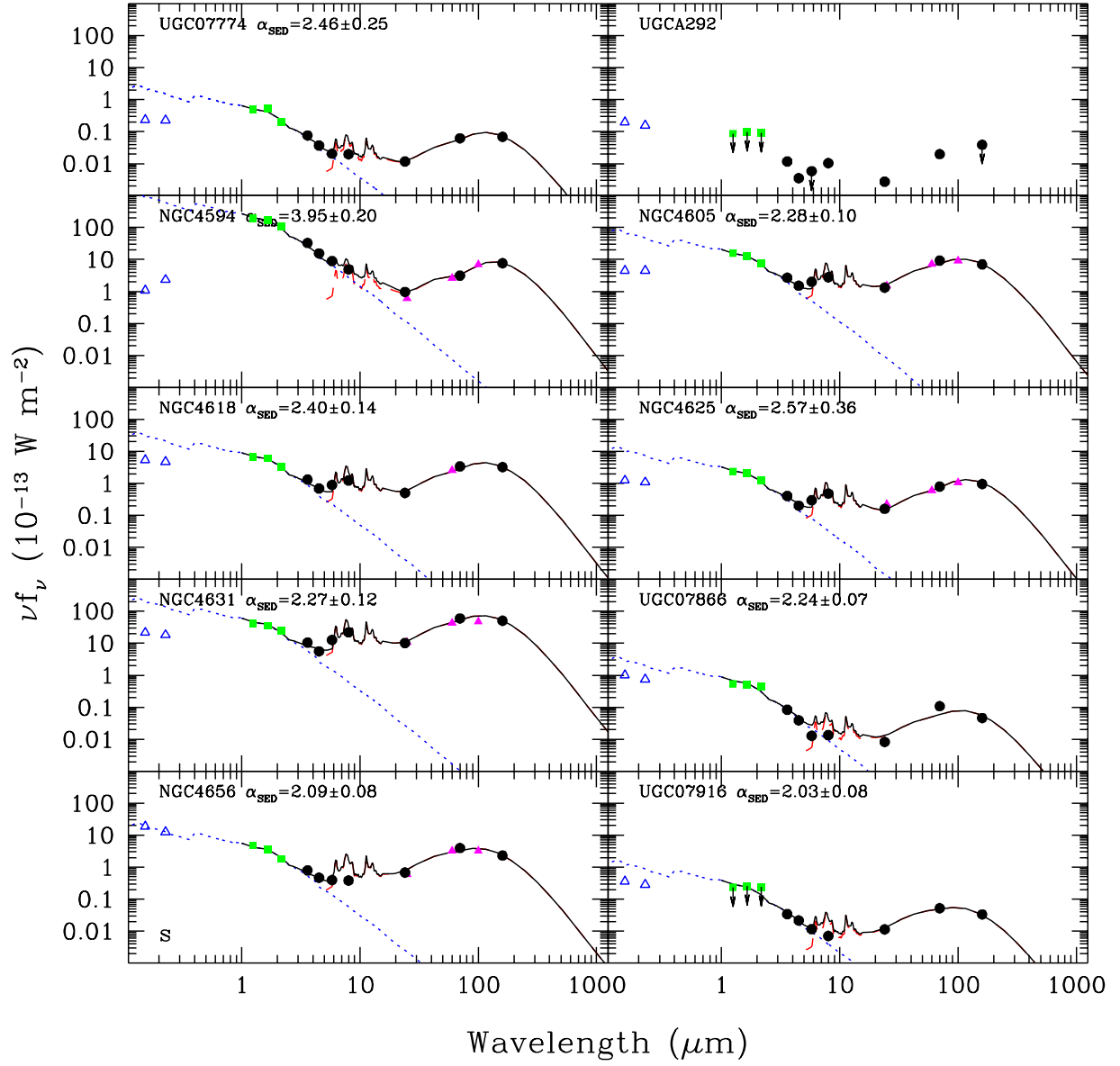


Fig. 10.— Globally-integrated 0.15-160 μm spectral energy distributions for the LVL sample (continued).

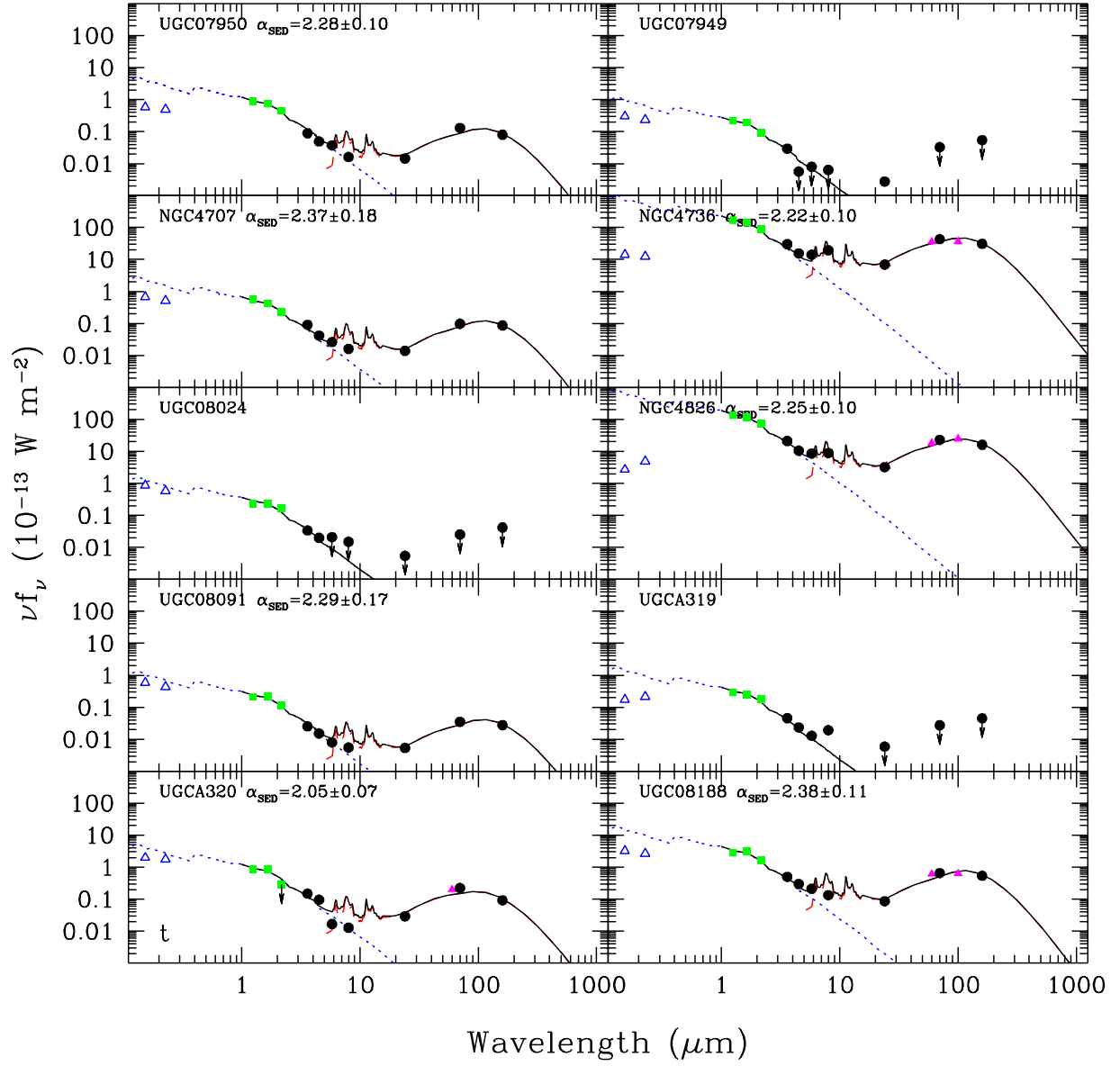


Fig. 10.— Globally-integrated 0.15-160 μm spectral energy distributions for the LVL sample (continued).

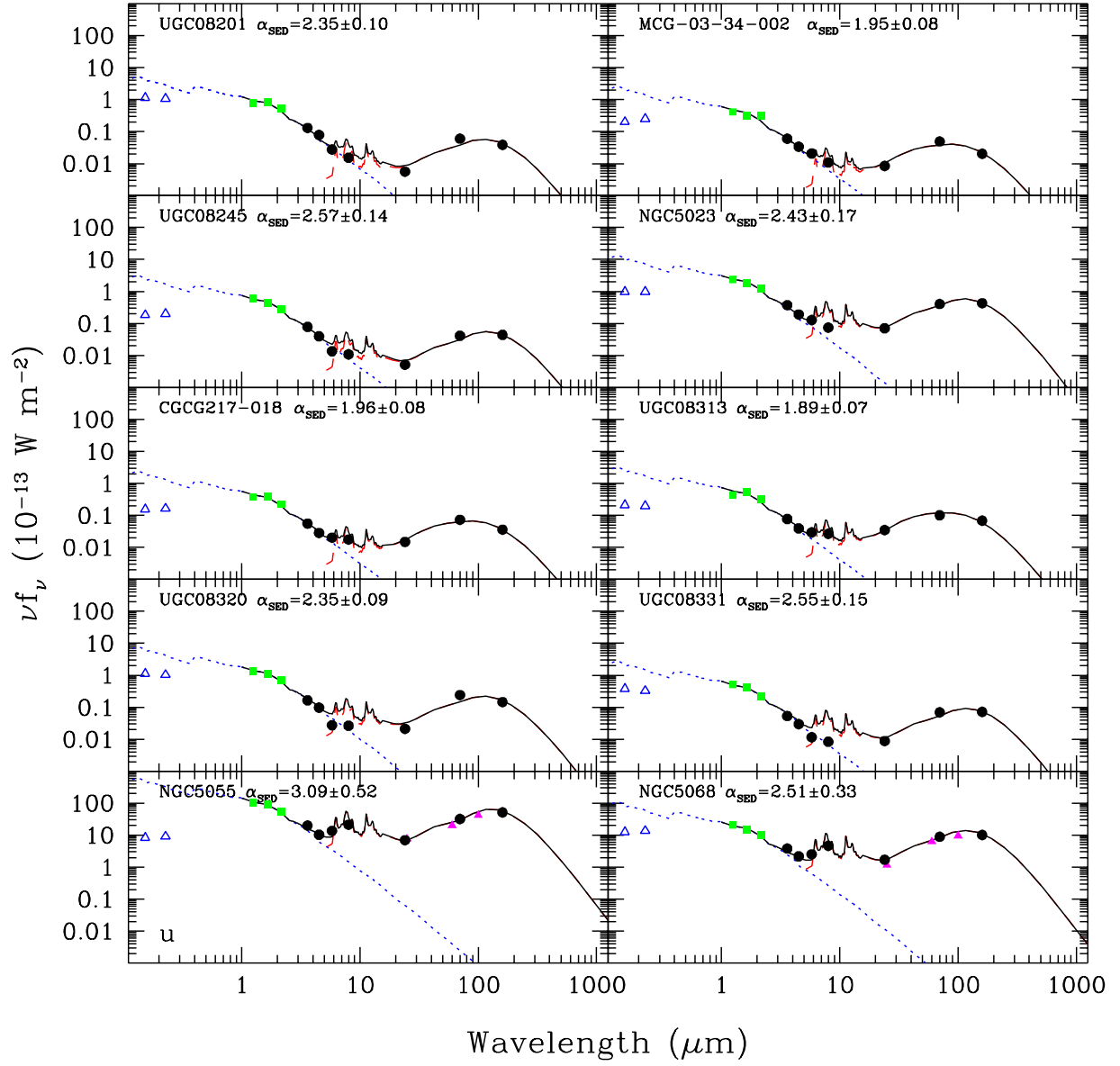


Fig. 10.— Globally-integrated 0.15-160 μm spectral energy distributions for the LVL sample (continued).

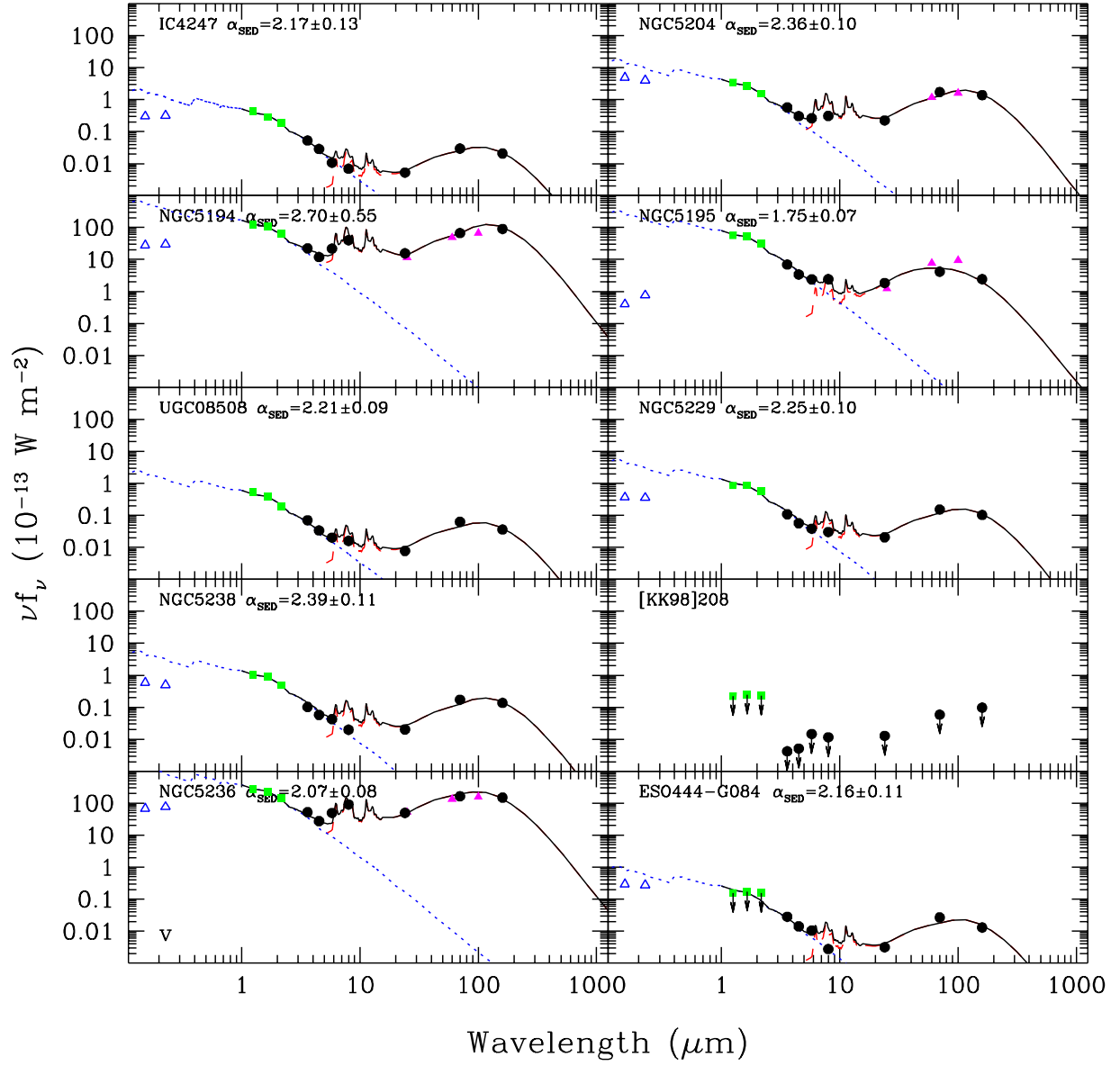


Fig. 10.— Globally-integrated 0.15-160 μm spectral energy distributions for the LVL sample (continued).

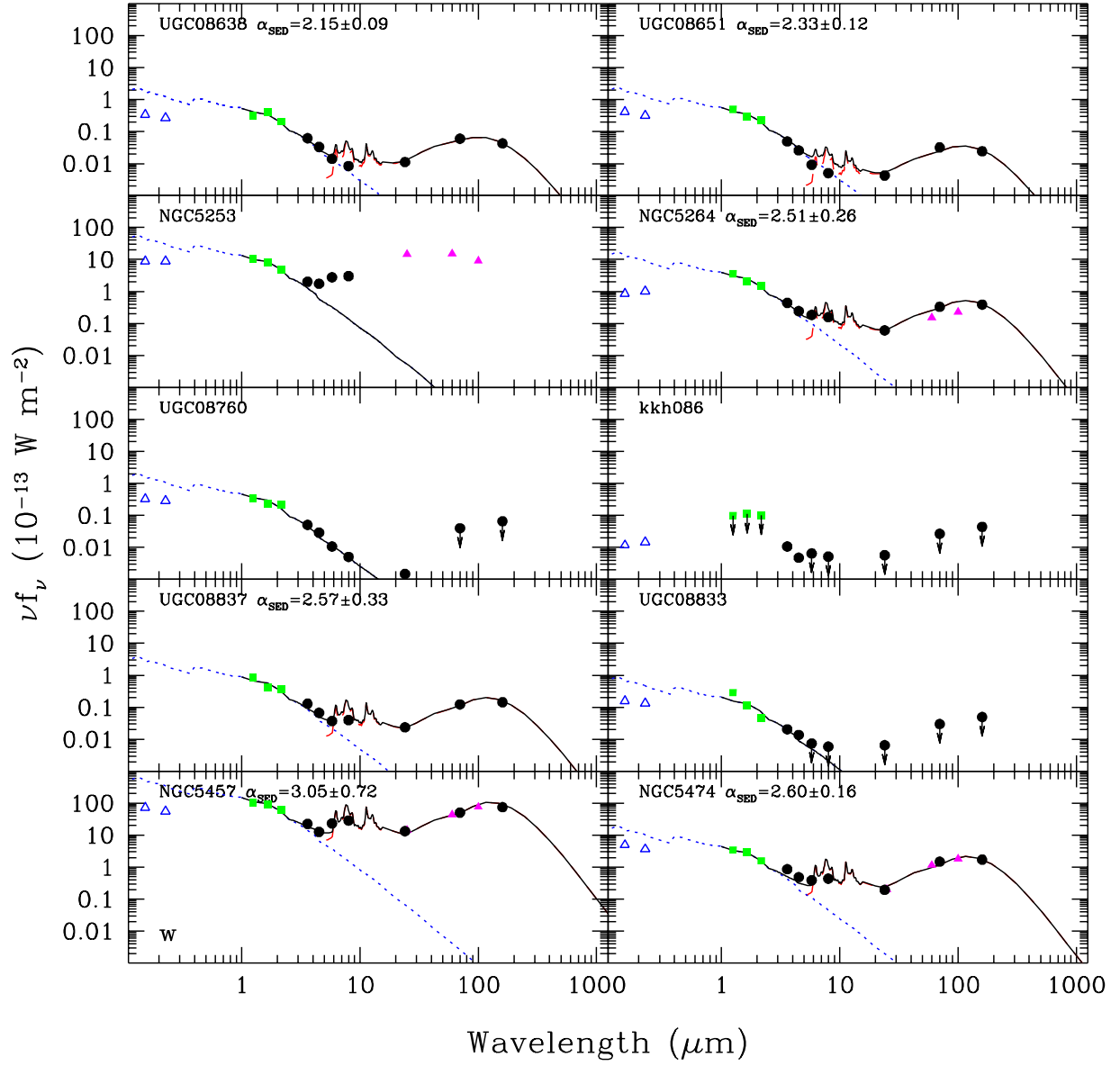


Fig. 10.— Globally-integrated 0.15-160 μm spectral energy distributions for the LVL sample (continued).

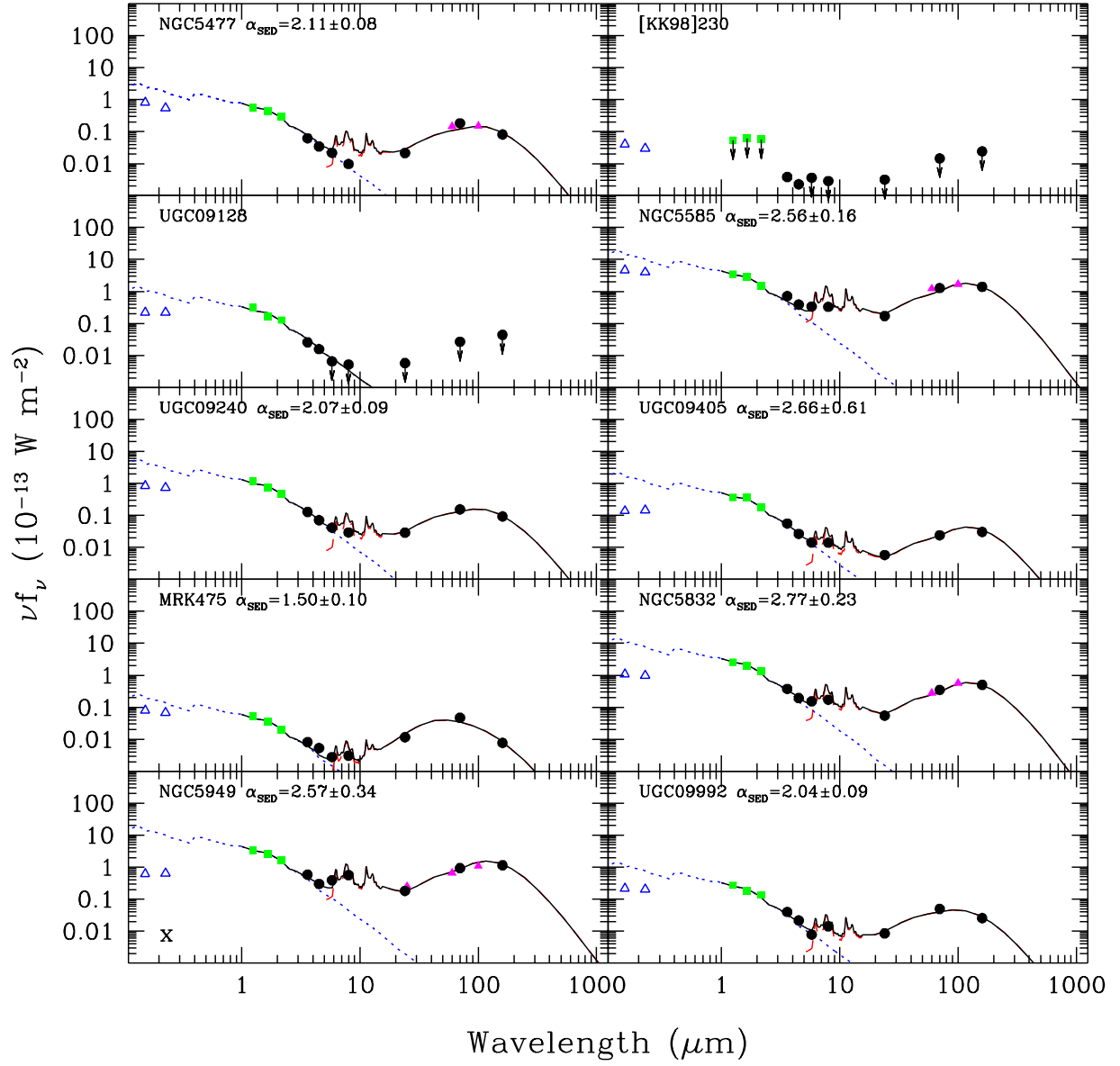


Fig. 10.— Globally-integrated 0.15-160 μm spectral energy distributions for the LVL sample (continued).

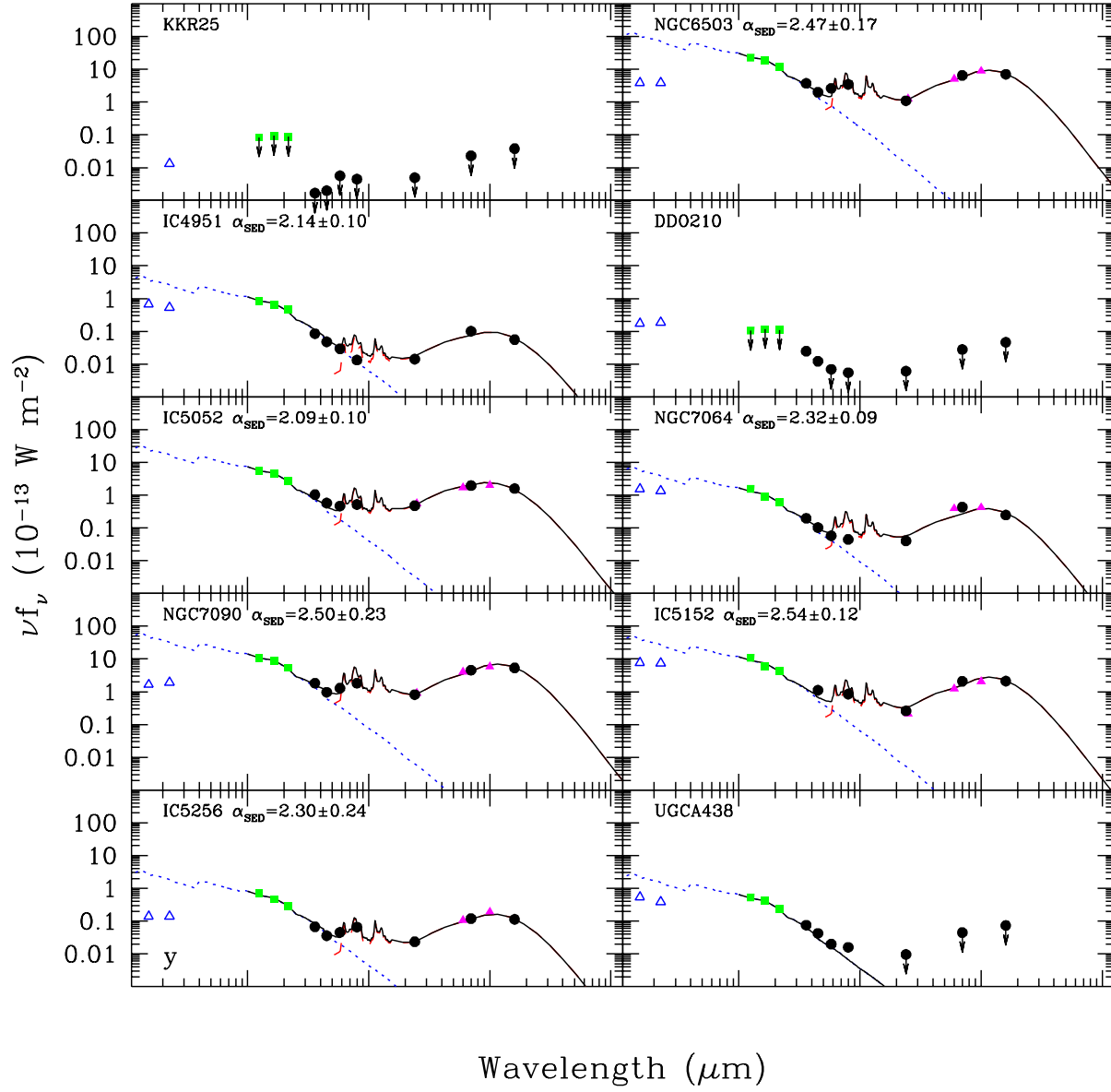


Fig. 10.— Globally-integrated 0.15-160 μm spectral energy distributions for the LVL sample (continued).

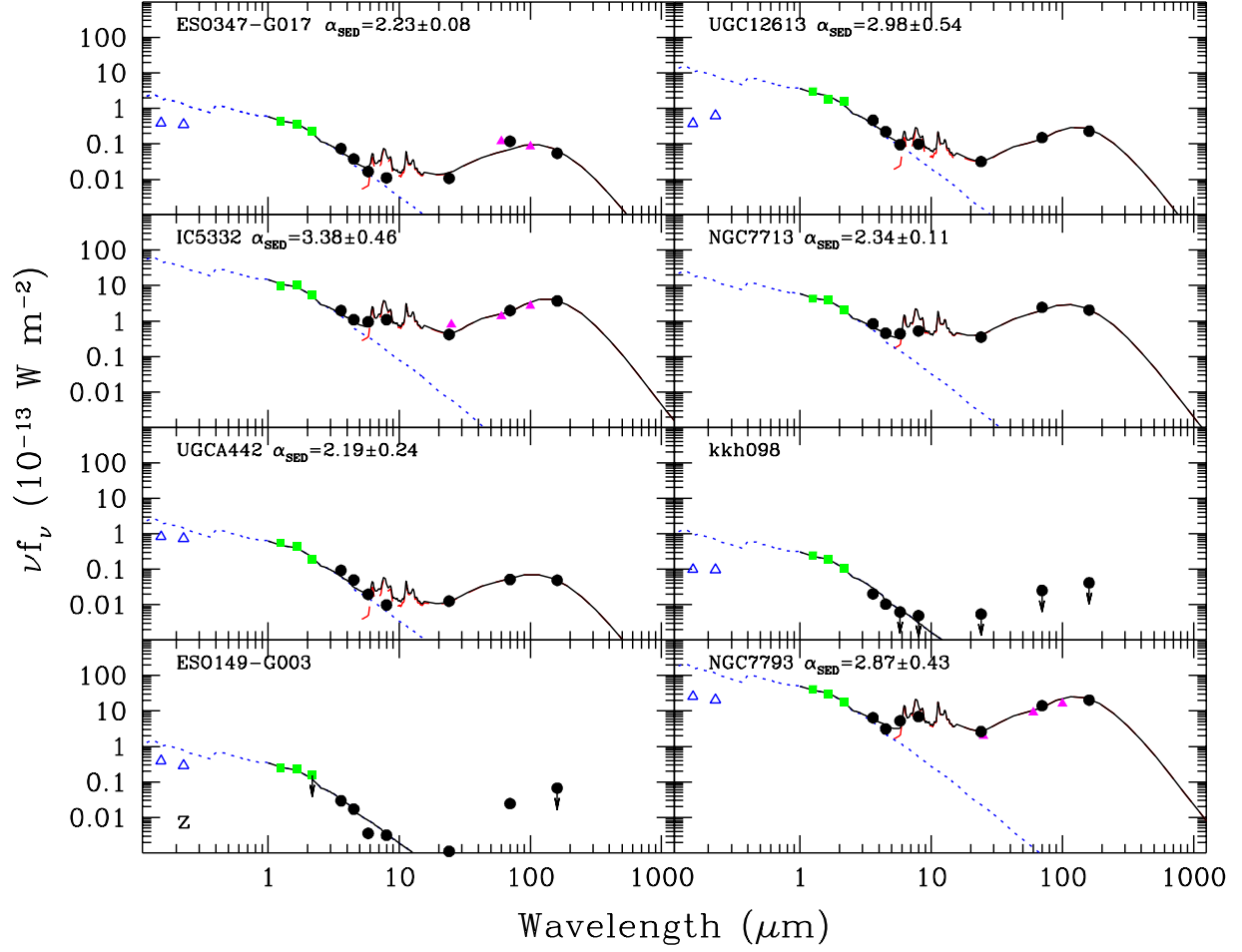


Fig. 10.— Globally-integrated 0.15-160 μm spectral energy distributions for the LVL sample (continued).

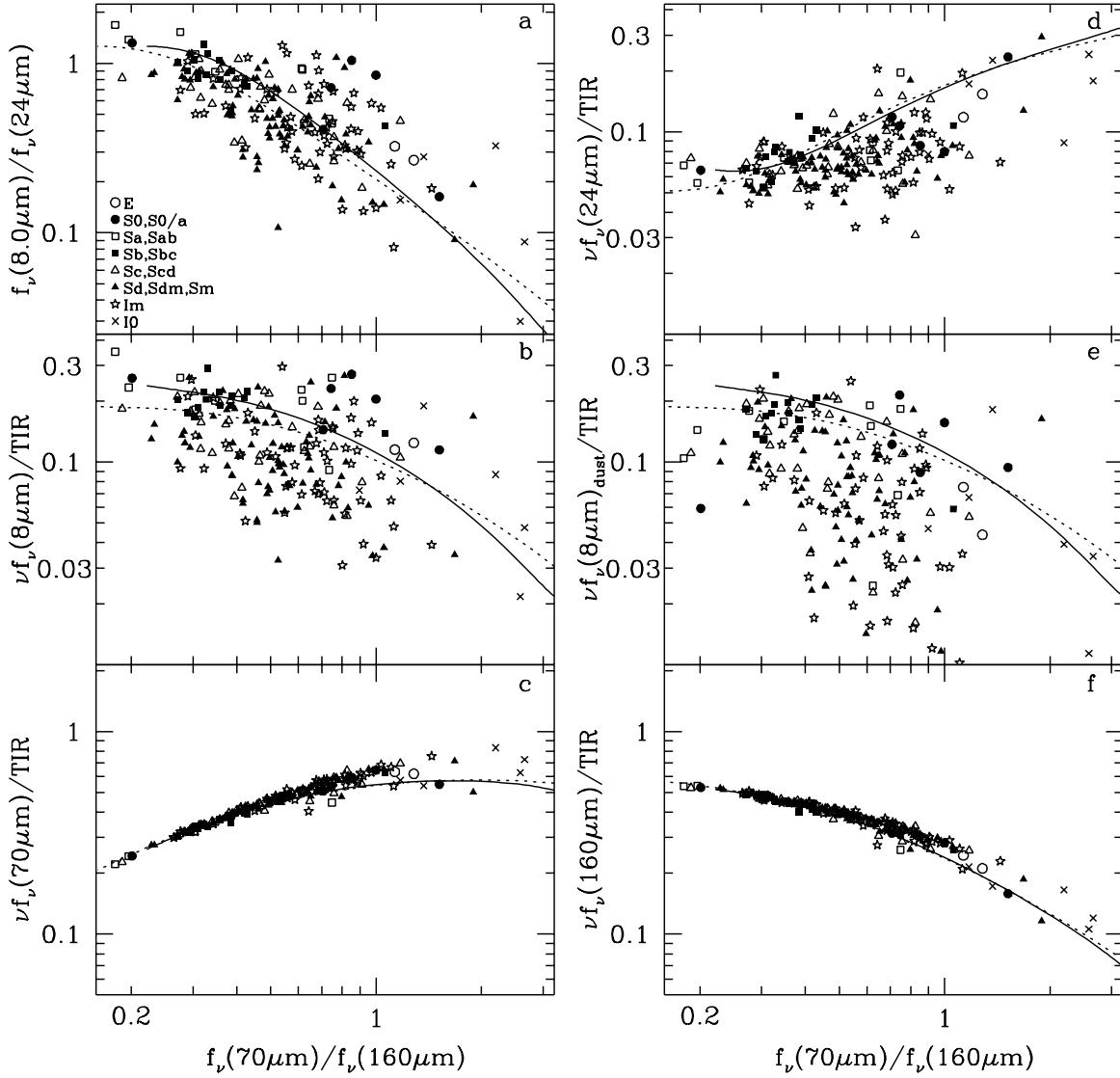


Fig. 11.— The *Spitzer* infrared colors and monochromatic-to-bolometric infrared ratios for globally-integrated LVL data. The solid and dotted lines indicate the dust-only SED models of Dale & Helou (2002) and Dale et al. (2001), respectively, derived from the average global trends for a sample of normal star-forming galaxies observed by *ISO* and *IRAS*. A y -axis logarithmic range of ~ 1.6 dex is the same for panels b–f for ease of comparison.

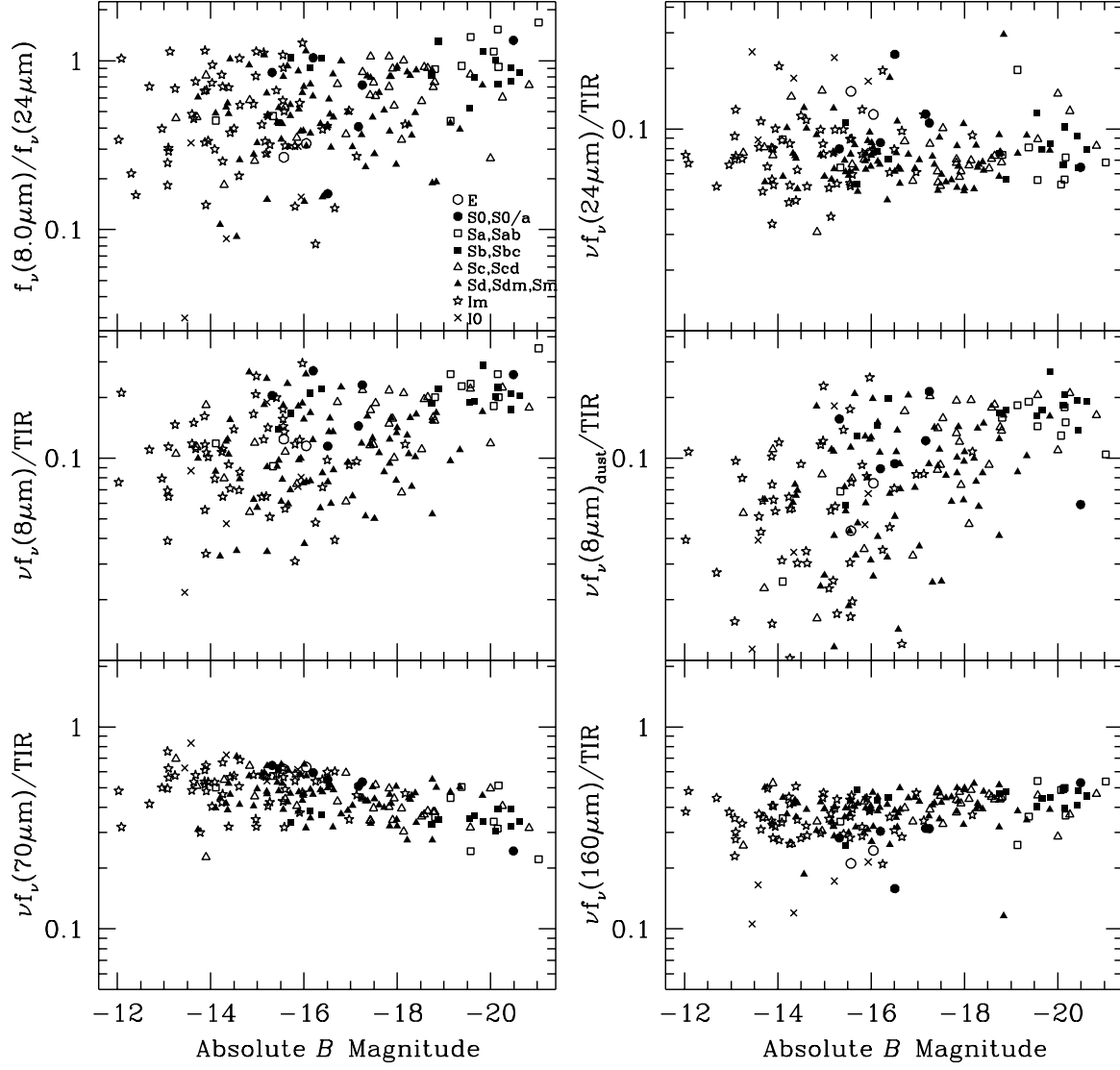


Fig. 12.— Similar to Figure 11 except as a function of absolute B magnitude.

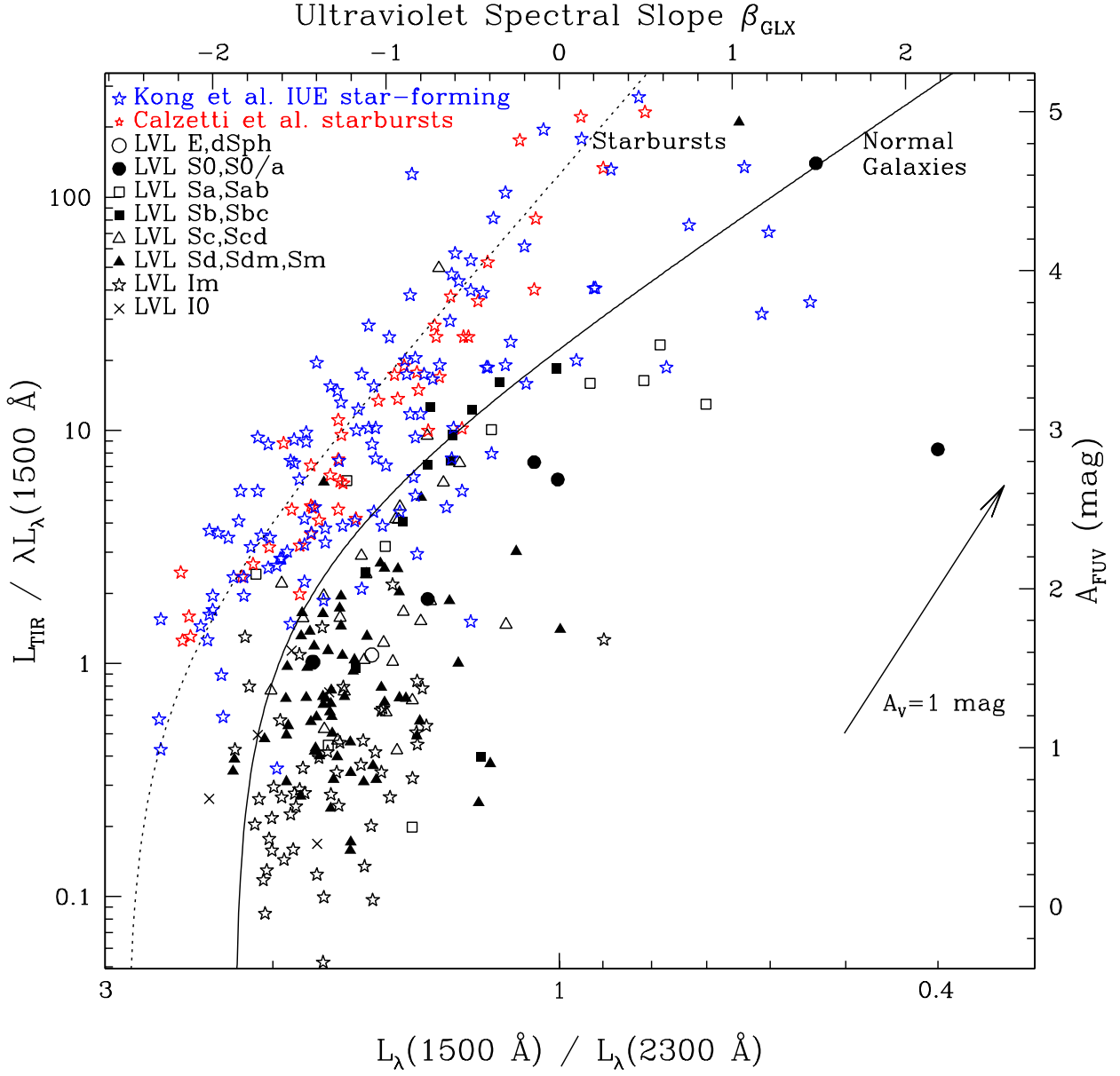


Fig. 13.— The infrared-to-far-ultraviolet ratio as a function of ultraviolet spectral slope. Normal star-forming and starbursting galaxies from Kong et al. (2004) and Calzetti et al. (1995) are plotted in addition to the LVL data points. The dotted curve is that for starbursting galaxies from Kong et al. (2004) and the solid curve is applicable to normal star-forming galaxies (Cortese et al. 2006). The reddening vector assumes the reddening curve of Li & Draine (2001) and the far-ultraviolet extinction prescription used for the righthand axis is from Buat et al. (2005).

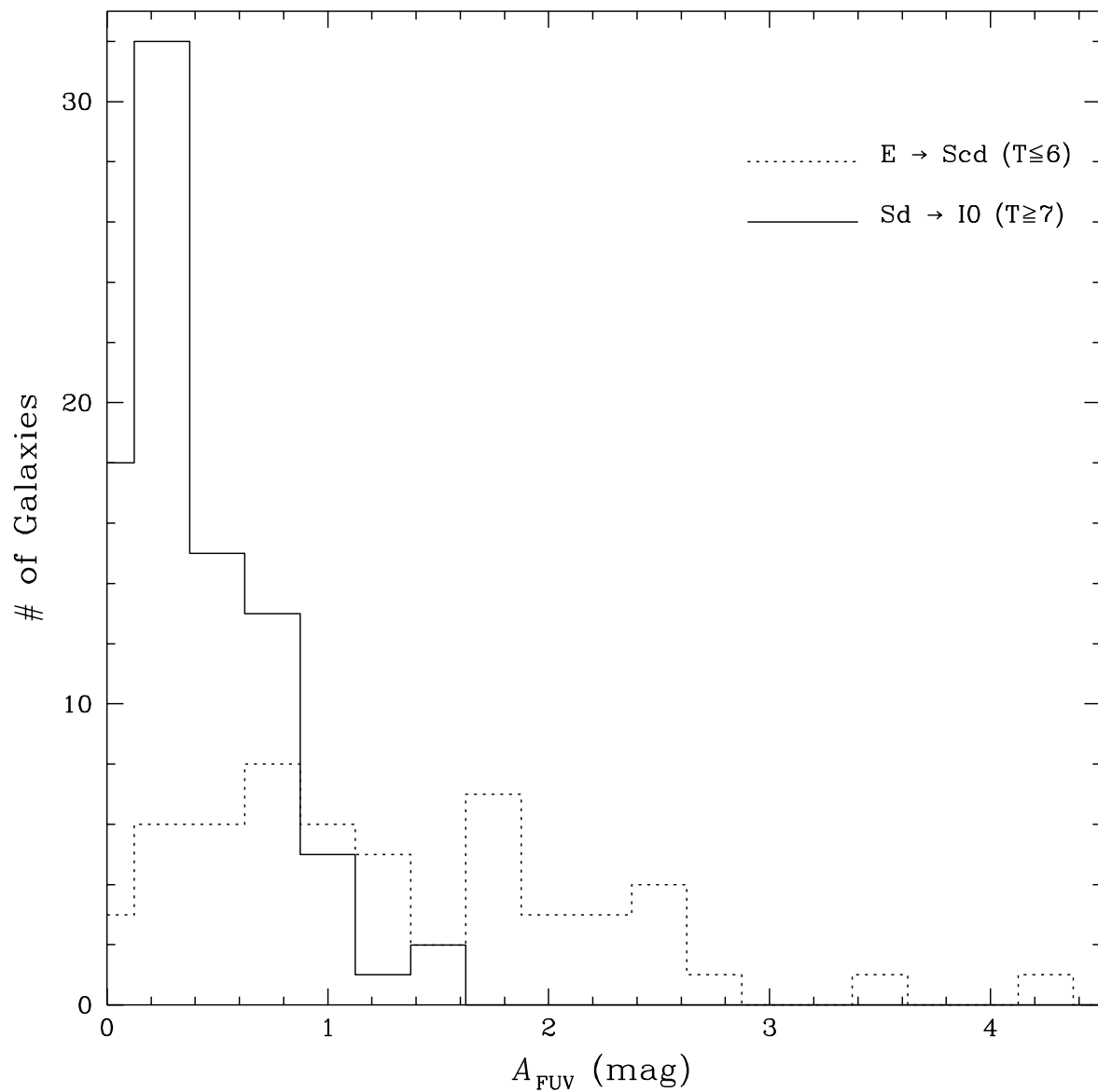


Fig. 14.— The distribution of far-ultraviolet extinctions, computed using the infrared-to-ultraviolet ratio and Equation 2 of Buat et al. (2005).

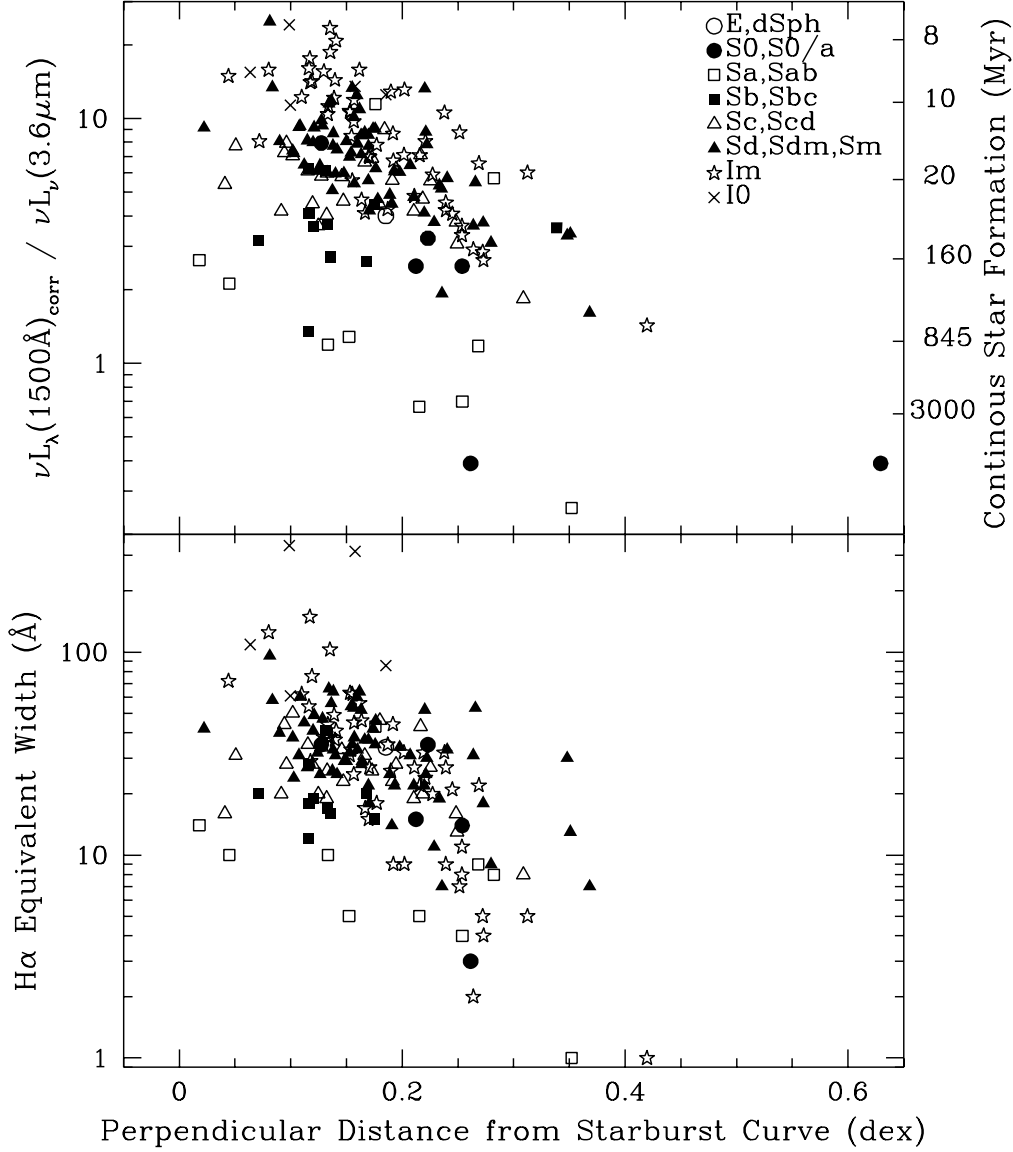


Fig. 15.— The dependence of galaxy star formation history as a function of distance from the starburst relation infrared-to-ultraviolet versus ultraviolet slope, as shown in Figure 13. The left-hand axes are observable diagnostics of the birthrate parameter, the current star formation rate normalized to the average star formation rate. Top: The far-ultraviolet-to-near-infrared ratio, with the righthand axis showing the number of years (continuous) star formation has been occurring, as measured from theoretical spectra. The theoretical spectra utilized are solar metallicity, $1 M_{\odot} \text{ yr}^{-1}$ continuous star formation curves assuming a double power law initial mass function, with $\alpha_{1,\text{IMF}} = 1.3$ for $0.1 < m/M_{\odot} < 0.5$ and $\alpha_{2,\text{IMF}} = 2.3$ for $0.5 < m/M_{\odot} < 100$ (Vazquez & Leitherer 2005). The far-ultraviolet emission is corrected for extinction using the recipe formulated in Buat al. (2005) and described in § 5.5. Bottom: The global H α equivalent width measured from narrowband and R band imaging.